3D Pixel Sensors
for the High Luminosity LHC
ATLAS Detector Upgra

David Vázquez Furelos

3D Pixel Sensors for the High Luminosity LHC ATLAS Detector Upgrade

Ph. D. Thesis
October 7, 2019

David Vázquez Furelos
Institut de Física d'Altes Energies
Universitat Autònoma de Barcelona

Thesis director

Sebastian Grinstein
ICREA / Institut de Física d'Altes Energies
Universitat Autònoma de Barcelona

Institut de Física d'Altes Energies
EXCELENCIA SEVERO OCHOA
BIST Barcelona Institute of Science and Technology
Universitat Autònoma de Barcelona

Abstract

The Large Hadron Collider (LHC) located in Geneva is the largest accelerator ever constructed. It produces proton-proton collisions in the center of the ATLAS detector, which collects the information of the collisions. The LHC started operations in 2008 at a center of mass energy of 7 TeV and an instantaneous luminosity of 10^{34} cm^{-2}s^{-1}. In 2011 the energy was increased to 8 TeV. The starting luminosity was upgraded in 2015 to $2{\times}10^{34}$ cm^{-2}s^{-1} and the center of mass energy to 13 TeV. The extensive program of the LHC includes an accelerator upgrade in 2026 to an energy of 14 TeV and a luminosity of $7{\times}10^{34}$ cm^{-2}s^{-1}. This is known as the High Luminosity LHC (HL-LHC) phase.

Following the LHC upgrades, the ATLAS detector also has an upgrade program. The original ATLAS detector was first upgraded in 2015, when a new layer of pixel detectors (IBL) was mounted directly on the beam pipe to improve its detection capabilities. To cope with the conditions of the HL-LHC, the innermost subsystem of the ATLAS detector (Inner Detector - ID) will be completely replaced by the the new Inner Tracker (ITk). This new fully silicon-based subsystem is formed by layers of pixel detectors and layers of strip detectors. The innermost layer of the new ITk pixel detector is specially important: it plays a critical role in the determination of the track impact parameter and thus it is fundamental for b-tagging. At the same time, it is the layer exposed to the highest particle rates and radiation damage.

The 3D pixel sensors, which are the topic of this thesis, are the strongest candidates to be used in the innermost layer of ITk thanks to the advantage that they offer over the planar pixel sensors. Since in 3D sensors the electrodes are columns that penetrate the silicon bulk, instead of implants on the surface (like in planar sensors), the distance between electrodes is disentangled from the thickness of the device. This allows to reduce the electrode distance (hence increase radiation hardness) while keeping the signal amplitude (which is proportional to the thickness). Furthermore, with the reduced electrode distance, the depletion voltage is lower hence reducing the power dissipation.

The 3D pixel sensors studied in this thesis were coupled to the chip used in IBL, the FE-I4, since the first prototype of chip to be used in ITk (RD53A) was only available in 2018. They were tested in beam tests before and after irradiation up to a fluence of $2.8{\times}10^{16}$ n$_{eq}$/cm^2 comfortably exceeding the ITk requirements of $1.4{\times}10^{16}$ n$_{eq}$/cm^2. An efficiency of 97% was achieved for the highest fluence at 150 V. Also, for the benchmark fluences of 5×10^{15} n_{eq}/cm^2 a voltage of 40 V is needed for 97% efficiency with a power dissipation of 1.5 mW/cm^2 and for 1×10^{16} n_{eq}/cm^2 a voltage of 100 V is needed for 97% efficiency with a power dissipation of 8 mW/cm^2. These results show that 3D sensors largely outperformed the planar technology in terms of radiation hardness and power dissipation. The original work presented in this thesis resulted in the choice of 3D pixel sensors as the baseline technology for the innermost layer of ITk.

Resumen

El Gran Acelerador de Hadrones (LHC) localizado en Ginebra es el acelerador más grande del mundo. Produce colisiones protón-protón en el centro del detector ATLAS, el cual recopila la información de las colisiones. El LHC empezó a funcionar en 2008 con una energía en el centro de masas de 7 TeV y una luminosidad instantánea de 10^{34} $\mathrm{cm}^{-2}\mathrm{s}^{-1}$. En 2011, la energía fue incrementada hasta 8 TeV. La luminosidad incial fue incrementada en 2015 hasta $2{\times}10^{34}$ $\mathrm{cm}^{-2}\mathrm{s}^{-1}$ y la energía en el centro de masas hasta 13 TeV. El extenso programa del LHC incluye mejoras en el acelerador en 2026 hasta una energía de 14 TeV y una luminosidad de $7{\times}10^{34}$ $\mathrm{cm}^{-2}\mathrm{s}^{-1}$. Esta es conocida como la fase de Alta Luminosidad del LHC (HL-LHC).

Siguiendo las mejoras en el LHC, el detector de ATLAS también tiene un programa de mejoras. El detector ATLAS original fue mejorado por primera vez en 2015, una nueva capa de detectores de píxeles (IBL) se montó directamente en la tubería del acelerador para mejorar sus capacidades de detección. Para hacer frente a las condiciones del HL-LHC, el subsistema más interno del detector ATLAS (ID) será completamente reemplazado por el nuevo medidor de trazas interno (ITk). Este nuevo subsistema basado completamente en silicio está formado por capas de detectores de píxeles y capas de detectores de tiras. La capa más interna del nuevo detector de píxeles de ITk es especialmente importante: juega un papel crítico en la determinación del parámetro de impacto de la traza y, por lo tanto, es fundamental para determinar el b-tagging. Al mismo tiempo, es la capa expuesta a la tasa más alta de partículas y daño por radiación.

Los sensores de píxeles 3D, los cuales son el tema de esta tesis, son los candidato más fuertes para usar en la capa más interna de ITk gracias a las ventajas que ofrecen sobre los detectores de píxeles planares. Dado que en los sensores 3D los electrodos son columnas insertadas en el silicio, en lugar de implantes en la superficie (como en los detectores planares), la distancia entre electrodos están separadas del espesor del sensor. Esto permite reducir la distancia entre electrodos (por tanto incrementando la resistencia a la radiación) manteniendo la amplitud de la señal (que es proporcional al espesor). Además, gracias también a una reducida distancia entre electrodos se reduce el voltage de vaciamiento, por tanto reduce el consumo de potencia.

Los sensores de píxeles 3D estudiados en esta tesis fueron acoplados al chip usado en

IBL, el FE-I4, dado que el primer prototipo de chip que será usado en ITk (RD53A) solo estuvo disponible en 2018. Fueron estudiados con haces de partículas antes y después de ser irradiados hasta una fluencia de 2.8×10^{16} n_{eq}/cm^2 excediendo confortablemente los requisitos de ITk de 1.4×10^{16} n_{eq}/cm^2. Una eficiencia del 97% fue alcanzada para la más alta fluencia a 150 V. También, para la fluencia de referencia de 5×10^{15} n_{eq}/cm^2 se necesita un voltaje de 40 V para alcanzar la eficiencia del 97% con un consumo de potencia de 1.5 mW/cm^2 y para una fluencia de 1×10^{16} n_{eq}/cm^2 se necesita un voltaje de 100 V para alcanzar el 97% de eficiencia con un consumo de potencia de 8 mW/cm^2. Estos resultados muestran que los sensores 3D superan en gran medida la tecnología de sensores planares en términos de resistencia a la radiación y consumo de potencia. El trabajo original presentado en esta tesis ha resultado en la elección de los sensores de píxeles 3D como la tecnología base para la capa más interna de ITk.

Contents

Chapter 1

Introduction

Silicon detectors are presently the most precise charged particle detectors in High Energy Physics. Thanks to advanced microelectronics silicon wafer techniques, an excellent position resolution (of a few micrometers) can be achieved in pixel sensors. Furthermore, thanks to the intrinsic radiation hardness of silicon detectors, they are an excellent option to measure particles' trajectories close to the interaction point in high radiation environments. Due to these features, silicon detectors have contributed significantly to the study of heavy quarks like charm, beauty and top, and the recent discovery of Higgs particle in the Large Hadron Collider. In addition to their excellent position resolution, their collection time is short (in the order of 10 ns) and they can be operated in strong magnetic fields. In particular, silicon pixel detectors have been chosen as the central tracking detectors in many LHC experiments, like ATLAS and CMS. In these experiments, the silicon detectors have to operate in an environment that imposes very harsh radiation hard requirements. Radiation damage limits the lifetime and performance of silicon sensors in more than one way. It changes the doping concentration of the silicon sensors, but more critically, increases the leakage current and introduces charge trapping. The increase of leakage current increases power dissipation and noise, while trapping reduces the signal amplitude. Thus, continuous progress has been carried out to improve the radiation hardness of silicon sensors (and their associated read out electronics).

The LHC is the largest particle accelerator ever constructed with its 27 kilometer long ring. It started running in 2008 at a energy of 7 TeV with a luminosity of 10^{34} cm^{-2}s^{-1}; however, it has an extensive program which includes several upgrades. The main upgrades are related to the energy of the collisions, which will be increased to 14 TeV, and the luminosity, which is expected to increase up to 7×10^{34} cm^{-2}s^{-1}. The LHC is planned to work at its highest luminosity after 2026, in the High Luminosity phase (HL-LHC) to improve the discovery potential of the experiments.

The ATLAS detector is one of the two general purpose experiments, which is designed to exploit the complete range of physics opportunities that the LHC offers. The ATLAS detector is formed by several subdetectors specialized on the measurement of energy and momentum of the particles originated from the LHC collisions. There are three main subsystems and the innermost is focused on the measurement of trajectories closest to the interaction point with high precision[1]. In particular, silicon sensors with pixel size of 50×400 μm^2 were installed in the four innermost layers of the first version of ATLAS, but it was updated in 2015 with a new layer (IBL) closer to the interaction point with silicon sensors with pixel size of 50×250 μm^2. For the HL-LHC phase, the Inner Tracker (ITk) subdetector is planned to replace the current innermost subsystem. The silicon pixel detectors planned for the ITk upgrade will have a pixel size of either 50×50 μm^2 or 25×100 μm^2. These ITk silicon sensors will have to sustain an unprecedented radiation dose while providing excellent performance (in terms of reconstruction efficiency and position resolution).

3D sensors are a novel, but well established technology, that was proposed to improve the capabilities of the existing planar sensor technology. In planar sensors, the electrodes that collect the charge carriers are positioned in the surface of the semiconductor, hence the distance between electrodes is fixed by the thickness of the device. On the other hand, for 3D sensors, the electrodes are column-like and go through the semiconductor bulk, disentangling the distance between electrodes from the thickness of the device. To reduce the electrode distance (collection distance) in a planar device, it is necessary to reduce the thickness of the device, hence reducing also the signal amplitude. For 3D sensors, the collection distance is determined by the column separation and can be made very short without affecting the signal amplitude. This property also reduces the trapping probability after irradiation (improving radiation hardness), improves the charge collection time and reduces the depletion voltage (also reducing the leakage current and thus the power dissipation). Thanks to these properties, 3D sensors were used already in IBL (which is composed of 25% of 3D sensors and 75% of planar sensors).

In this thesis, the performance of 3D sensors with pixel size of 50×50 μm^2 and 25×100 μm^2 is studied, to determine if the 3D sensor technology is suitable for the innermost layers of the ITk Pixel detector. The devices are studied before and after high levels of irradiation, up to the fluence that the ITk subdetector will face after several years working at HL-LHC luminosity. For ITk, a new chip has been developed but was not available for the studies performed in this thesis. However, the previous chip, used in IBL (with pixel size of 50×250 μm^2), was used to provide a testing framework of the 3D sensors with reduced pixel size using the strategy described in this thesis.

The text is divided in 7 chapters. In the following chapter, a description of the Large Hadron Collider and the different phases that has and will go through is given. In chapter 3, the ATLAS experiment and its different phases and upgrades are explained, focusing

---

[1] The other subsystems are the calorimeters and the muon system.

more on the current innermost subsystem (ID) and its upgrade (ITk). Chapter 4 describes the basic characteristics of semiconductor (silicon) detectors, how the signal is produced and the effects of the radiation damage on the signal and ends with a short description of the 3D sensors and their fabrication process. Chapter 5 shows the instrumentation (readout systems and chips), the methods used to study the 3D sensors performance (chip calibration and beam tests) and the facilities used for irradiation and beam testing. The fabrication of the first 3D pixel prototypes with small pixel size, how are they coupled to the existing FE-I4 chip and the experimental measurements carried out on these devices are presented in chapter 6. Finally a summary and conclusions are given in chapter 7.

Chapter 2

The Large Hadron Collider, present and future

The Large Hadron Collider (LHC) [1] is located at the Conseil Européen pour la Recherche Nucléaire (CERN) in Geneva and is presently the largest particle accelerator and the most powerful since it first started operations in 10 September 2008. The LHC was constructed in the tunnel previously used by the Large Electron Positron accelerator (LEP). The LHC consists of a 27 kilometer ring which uses a number of accelerating structures with superconducting magnets to boost the energy of the circulating particles. Two particle beams (protons or heavy ions (Pb)) accelerated in two separated beam pipes (tubes at ultrahigh vacuum) travel in opposite directions and collide in certain positions of the accelerator where the main experiments are placed (see chapter 3). The trajectory of these beams is guided around the accelerator ring by a strong magnetic field generated by superconducting magnets. To keep the magnets working in a superconducting state they need an efficient cooling system, which operates with liquid helium at 1.85 K. The magnets are a critical part of a accelerator system, and different types of them are used mainly: dipoles and quadrupoles. The dipole magnets bend the trajectories of the charged particles, while the quadrupoles act like a lens, focusing the beam and avoiding that the particles spread out. Also, a kicker magnet is used to merge the two beams to produce the collisions (injection) or to empty an accelerator (beam dump). The radiofrecuency (RF) cavity is a chamber where an electric field is applied to speed up the particles going through it. The chambers are shaped to resonate at specific frequencies, allowing radio waves to interact with passing particle bunches. Each time a beam passes the electric field in an RF cavity, some of the energy from the radio waves is transferred to the particles, speeding them forward. To avoid the collision of the beam particles with gas molecules of the air (hence losing energy in the process) the mentioned ultrahigh vacuum is needed inside the beam pipe.

A set of smaller accelerators is used to pre-accelerate the particles that are injected

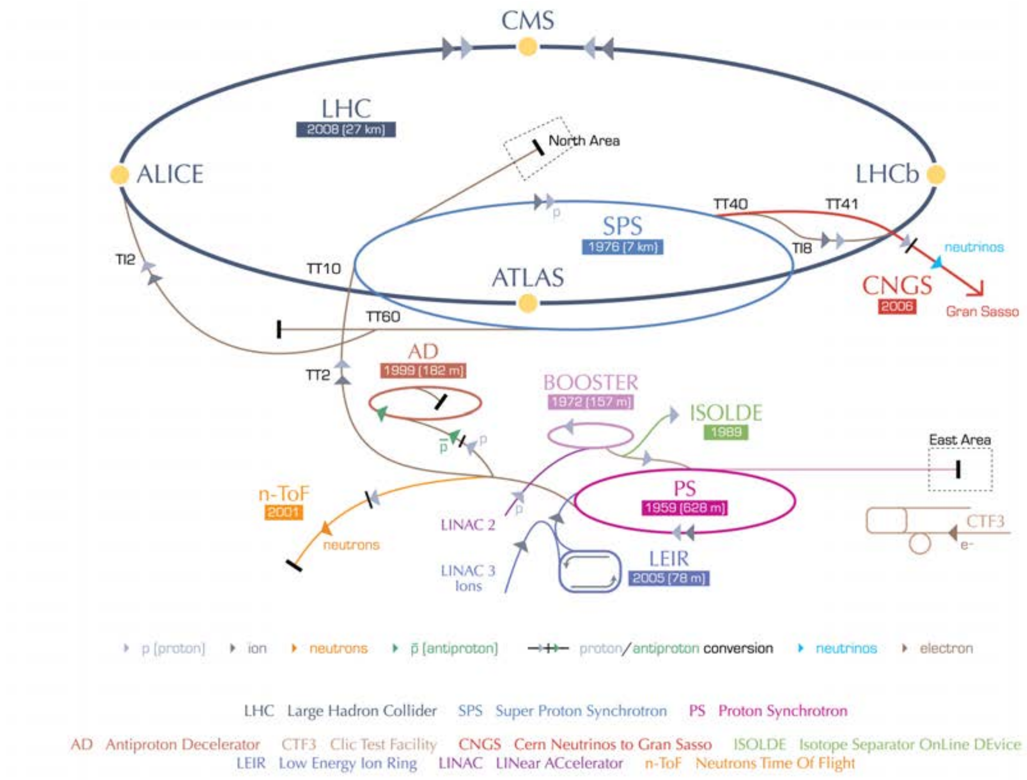

Figure 2.1: The LHC accelerator complex at CERN. Taken from [2].

into the LHC to the minimum energy that the particles need to travel inside the LHC ring. The full CERN accelerator complex is shown in figure 2.1. The protons come from a bottle of hydrogen gas and are first accelerated in the Linear Accelerator (LINAC 2) to 50 MeV and then injected to the proton synchrotron booster (PSB), in which they are accelerated to 1.4 GeV. Then they are transferred to the Proton Synchrotron (PS) and accelerated up to an energy of 25 GeV and finally in the Super Proton Synchrotron (SPS) to 450 GeV before entering in the LHC. For the heavy ion operations, the lead ions are obtained from a source of vaporised lead and accelerated first in the LINAC 3 and then in the Low Energy Ion Ring (LEIR) before being injected into the PS. From there, they follow the same accelerating path as the protons to enter the LHC. The pre-accelerators are also used for a different purposes such as other particle physics experiments, beam tests or irradiation of detector material for radiation hardness studies (see sections 5.4 and 5.5).

The main characteristics that define the performance of an accelerator are its energy and luminosity. In the case of LHC, the energy is measured in terms of the center of mass reference frame (noted as $\sqrt{s}$). The first collisions produced by LHC were at $\sqrt{s} = 7$ TeV by accelerating each circulating beam to 3.5 TeV. A shutdown was performed in 2011 and the energy was increased to $\sqrt{s} = 8$ TeV. The Run 1 period lasted until 2012 and took data at the energy of 8 TeV.

The luminosity ($\mathcal{L}$) of the accelerator determines the rate of particle interactions, R, occurring for a given process with cross section σ_p (total cross section of pp → X):

$$R = \mathcal{L}\sigma_p \tag{2.1}$$

The machine luminosity depends only on the beam parameters and is defined as the beam intensity I per collision area A. For a circular machine, assuming Gaussian beam profiles:

$$\mathcal{L} = \frac{I}{A} = \frac{N_b^2 n_b f_{rev} \gamma}{4\pi\epsilon_N \beta^*} R_\phi \tag{2.2}$$

where N_b is the number of particles per bunch, n_b the number of bunches per beam, f_{rev} the revolution frequency, γ the relativistic Lorentz factor, ϵ_N the normalized transverse beam emittance[1], β^* is the beta function at the interaction point[2] and R_ϕ is a geometrical correction which takes into account the crossing angle of the bunches. Equation 2.2 is integrated to obtain the integrated luminosity, L=$\int \mathcal{L}$dt. The average number of interactions, $\langle\mu\rangle$, which quantifies the number of interactions per event (referred as pile-up), is given by the ratio between the rate of generated events and the bunch crossing rate

$$\langle\mu\rangle = \frac{\mathcal{L}\sigma_{tot}}{n_b f_{rev}}. \tag{2.3}$$

The LHC was designed to run at $\mathcal{L} = 10^{34}$ cm^{-2}s^{-1} and an energy of 14 TeV, with 1.15×10^{11} protons per bunch and 2808 bunches per beam that are separated by 25 ns (40 MHz bunch crossing rate) and a f_{rev} = 11.245 kHz. The nominal ϵ_N is 3.75 μm and β^* is 0.55 m. However, during Run 1, the LHC worked at instantaneous luminosity of $\mathcal{L}$ = 0.7×10^{34} cm^{-2}s^{-1}, and an energy of 7 (2011) - 8 (2012) TeV, with 1.6×10^{11} protons per bunch (higher than design but lower than the limit usable value of 1.7×10^{11}) and 1374 bunches per beam, separated by 50 ns. The value of the pile-up was $\langle\mu\rangle \sim 20$ events for this Run. A total integrated luminosity of 28.26 fb^{-1} was delivered by LHC during Run 1 of which 26.38 fb^{-1} was recorded by ATLAS and 24.87 fb^{-1} was certified as good quality data [3].

During the first Long Shutdown (LS1 - 2013-2015), an upgrade to the LHC was performed, increasing the energy to 13 TeV and the instantaneous luminosity to $\mathcal{L}$ = 1.7×10^{34} cm^{-2}s^{-1}. The number of protons per bunch was 1.2×10^{11} with 2556 bunches per beam separated 25 by ns reaching a pile-up $\langle\mu\rangle \sim$ of 50 events. The ϵ_N was 3.5 μm and the β^* was 0.4 m. During the Run 2 (2015-2018) a maximum instantaneous luminosity of 2.1×10^{34} cm^{-2}s^{-1} was reached and the beam was squeezed down to a β^* of 0.25

---

[1] The beam emittance is a measurement of the spread of the beam particles in position and momentum. A small emittance is preferred for small distance confinement and uniform transverse momentum.

[2] The beta function is related to the transverse size of the particle beam at the location along the nominal beam trajectory. A small values at the interaction point is preferred for larger luminosity.

Figure 2.2: The schedule of LHC. Adapted from [6].

m. As shown in equation 2.2 this increases the total number of collisions (the integrated luminosity), which helps to build statistics. The pile-up during this run was $\langle\mu\rangle \sim 50$ events. A total integrated luminosity of 156 fb^{-1} was delivered by LHC during Run 2 of which 147 fb^{-1} was recorded by ATLAS and 139 fb^{-1} was certified as good quality data [4].

During the on-going second Long Shutdown (LS2 - 2019-2020) a new upgrade to the LHC is under development, to increase the energy to the designed 14 TeV and the instantaneous luminosity to $\mathcal{L} = 2{\times}10^{34}$ $\mathrm{cm}^{-2}\mathrm{s}^{-1}$. A beam spacing of 25 ns is also expected. This shutdown is also aiming to the upgrade of the injection accelerators (LHC Injectors Upgrade - LIU) to deliver high brightness beams in preparation for the HL-LHC. In particular the LINAC 2 was replaced by the new LINAC 4 which can accelerate the initial protons to 160 MeV. The PSB will be prepared to take 160 MeV protons (instead of the previous 50 MeV) and accelerate them to 2 GeV. The PS will accelerate the beam from 2 to 26 GeV and the SPS will increase the energy from 26 to 450 GeV. In the PS some magnets will be renewed while at SPS some components of the acceleration system will be refurbished. The ion chain will also be upgraded. The Run 3 is expected to run from 2021 to 2023 and reach an integrated luminosity of 150 fb^{-1} to reach a total integrated luminosity of 300 fb^{-1} since the LHC started.

The third Long Shutdown (LS3 - 2024-2026) is a major change to the LHC, which will increase the instantaneous luminosity to $5{\times}10^{34}$ $\mathrm{cm}^{-2}\mathrm{s}^{-1}$ (possibly to $7.5{\times}10^{34}$ $\mathrm{cm}^{-2}\mathrm{s}^{-1}$). This upgrade is also known as upgrade Phase-2 or High Luminosity LHC (HL-LHC). The aim of the upgrade is to extend the discovery potential of the LHC by increasing its statistical power with the increase in the instantaneous luminosity. The aim is to collect ten times more statistics than the total of the previous runs, reaching an integrated luminosity of 250 fb^{-1} per year to a total of 3000 fb^{-1} (4000 fb^{-1}) in twelve years. The main components of the current LHC that need to be changed or improved due to the fast aging induced from the radiation damage or because they can become a bottleneck for operation in a higher radiation environment are the magnets, the cryogenics and the collimation system. The powering system of the magnets and other electronic systems are very sensitive to radiation damage, since they are located in a highly irradiated environment, and they will be either protected with new shielding materials or moved away from the irradiation source [5]. To increase the luminosity and keep the beam focused, the HL-LHC upgrade relies on the improvement of the LHC magnets, which will be done by using magnets with a new superconducting material (Nb_3Sn) which can reach a higher magnetic field. The HL-LHC is expected to start working in 2026 with Run 4 and take data at least to 2038. The pile-up during the HL-LHC phase is expected to be $\langle \mu \rangle \sim 200$ events.

Chapter 3

The ATLAS experiment

Together with CMS, ALICE and LHCb, ATLAS is one of the main four experiments located at the LHC. ALICE [7] is designed for the study of heavy-ion physics and focuses on QCD, the strong-interaction sector of the Standard Model. The LHCb [8] aims to measure with precision CP violation and rare decays of hadrons with b quarks. ATLAS [9] is a general purpose physics experiment run by an international collaboration and, together with CMS [10], is designed to exploit the full discovery potential and the complete range of physics opportunities that the LHC provides. The ATLAS detector tests the predictions of the Standard Model (SM), studying the building blocks of the matter and how they interact. The experiment achieved a milestone with the discovery of the Higgs boson, the last piece to complete the SM. In the future, ATLAS is going to continue the study of the properties of the Higgs boson and in general, the Standard Model, while also exploring the energy frontiers in search of extra dimensions or new particles.

ATLAS is the largest detector in volume ever constructed for a particle collider. It is a 44 m long cylinder, with a diameter of 25 m and a total weight of 7000 tonnes; placed 100 m underground. The detector is formed by layers designed to measure the momentum, energy and trajectory of the particles produced in the collisions. Many heavy particles are produced during these collisions, which are unstable and decay immediately to lighter particles. By measuring the characteristics of these light particles it is possible to reconstruct the collision event. Some of the particles created during the collisions cannot be detected (neutrinos or other weakly interacting particles with low cross section that can pass through all the ATLAS layers undetected) but thanks to the conservation of energy and momentum their presence can be inferred (these type of events are characterized by "missing transverse energy/momentum").

The ATLAS detector has changed during its lifetime due to the different phases that the LHC has gone through. The next main upgrade will be done to cope with the conditions required in the HL-LHC phase around 2026. The detector during Run 1 is described in section 3.1. Prior to Run 2 (during LS1) a new layer of pixel detectors

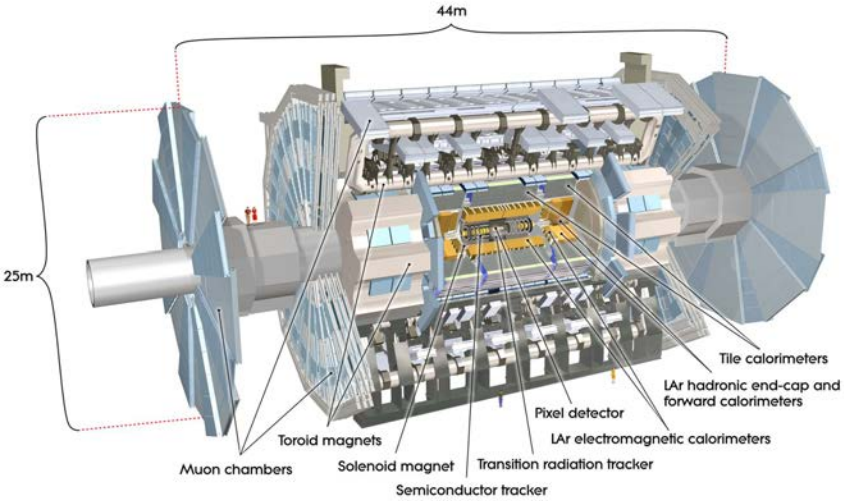

Figure 3.1: The ATLAS detector. Taken from [12].

was inserted closer to the beam pipe to allow a better resolution on the track impact parameter (needed due to the increase of the LHC luminosity (and hence higher pile-up)) and to identify jets coming from bottom and charm quarks from the decay of B-mesons (b-tagging). During LS2, the ATLAS tracking detector will not be upgraded since for Run 3 the LHC instantaneous luminosity is similar to Run 2 ($\sim 2\times10^{34}$ cm^{-2}s^{-1}) while the center of mass energy will be increased from 13 TeV to the maximum designed energy of 14 TeV. The LS3 is the time when the LHC upgrade to the HL-LHC takes place and at the same time, the ATLAS inner tracking detector will be upgraded to cope with a increased instantaneous luminosity of 5×10^{34} cm^{-2}s^{-1} (possible to be pushed to 7.5×10^{34} cm^{-2}s^{-1} in the ultimate scenario) and higher pile-up (∼200 events). The new innermost subsystem of the ATLAS detector for the HL-LHC upgrade (called ITk) will be described in section 3.2.

3.1 Current ATLAS detector

The current ATLAS detector is represented in figure 3.1. As mentioned before, it consists of different layers that measure the energy and momentum of the particles originated from the LHC collisions. In particular, there are three main subsystems, focused on the different particles that appear in the final state of the proton-proton collisions. These subsystems are from the inside to the outside: Inner detector, Calorimeter and Muon Spectrometer. Also, a Magnet system [11] is present to bend the trajectories of the charged particles allowing to measure their momenta with high precision.

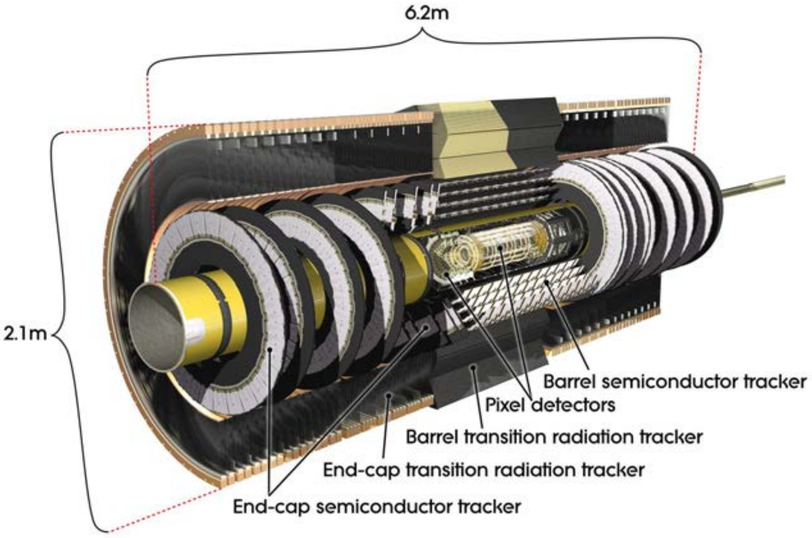

Figure 3.2: The ATLAS inner detector subsystem. Taken from [19].

3.1.1 Inner detector

The inner detector (ID) [13][14] is the innermost system of the ATLAS detector. Its purpose is to determine the trajectories of the charged particles generated in the LHC collisions. It is embedded in a solenoid magnet (see section 3.1.4) which allows to determine the electric charge and measure the momenta of the traversing particles. With this information the primary vertex (point of the original collision) or the secondary vertex (appearing due to the decay of long lived particles like b-hadrons) can be determined. The ID is formed by three subdetectors (see figure 3.2 and 3.5), from the innermost to the outermost are: the Pixel Detector, the SemiConductor Tracker (SCT) and the Transient Radiation Tracker (TRT). The pixel detector is the innermost part of the inner detector and provides the first measurement of the track momentum, impact parameter[1] and vertex position. Since the Pixel Detector is the focus of this thesis, it will be described with more details in section 3.2.

The SCT [15][16] is made of micro-strip p-in-n silicon sensors. They are placed in four cylindrical barrel layers (at 30.0, 37.3, 44.7 and 52.0 cm) with a length of $|z| \leq 74.5$ cm and nine planar end-cap discs per side. The pitch of the barrel micro-strips is 80 μm, while in the end-cap discs the pitch ranges from 56.9 to 90.4 μm. The strip length is 62.0 mm. Each layer of the barrel contains modules with two strip sensors with small angle between them, which provides better 2D resolution. A total of 4088 modules form the SCT, 2112 in the barrels and 1976 in the end-caps, covering an area of 60 m^2. The main objective of the SCT is to provide precision measurements of the tracks in the intermediate radial range,

---

[1] Perpendicular distance between primary and secondary vertex.

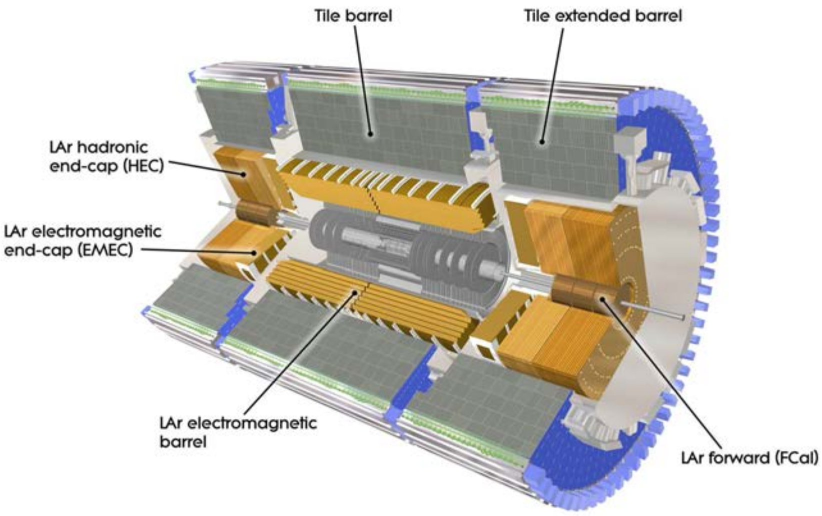

Figure 3.3: The ATLAS calorimeter subsystem. Taken from [22].

contributing to the measurement of the track momentum, impact parameter and vertex position together with the pixel detector. It also provides good pattern recognition thanks to the high granularity used. Both the pixel detector and the SCT require cold detector operation, and the removal of heat generated by the electronics and the detector leakage current. For this reason, the search of low power dissipation technologies is critical. The decision to use micro-strip in the SCT instead of pixel modules is to cover the large area required at a reduced cost. This is possible thanks to the more flexible requirements on the spacial resolution in these outer layers than in the pixel detector. The innermost part of the SCT is designed to withstand doses of $\sim 2\times 10^{14}$ n_{eq}/cm^2.

The TRT [17][18] is the outermost subdetector of the ID. It is composed by 4 mm diameter straw-tubes filled with an ionizing gas. The small pitch of the straw-tubes allows to obtain tracking information. In the center of the straw-tube, a 30 μm wire made of gold-plated Wolfram-Rhenium provides a drift time measurement, giving a spacial resolution per straw of 170 μm. The barrel section covers the radial range from 56 to 107 cm and the end-caps consist of 18 wheels (14 innermost covering radial range from 64 to 103 cm and 4 outermost from 48 to 103 cm). Polymer fibers (barrel) and radiation foils (end-caps) are inserted between the tubes to enable the generation of transition radiation by charged particles which also provides information to distinguish electrons and pions.

3.1.2 Calorimeters

The purpose of the calorimeter is to measure the energy of the incoming particles. Calorimeters are segmented and consist of interleaved active and passive (absorbing) layers. The ATLAS calorimeter is designed to stop or absorb most of the particles coming from the collision, forcing them to deposit all the energy within the detector. However, there are two known particles that are not stopped in the calorimeter system, the muons (see next section) and the neutrinos (their presence is inferred due to the missing transverse energy/momentum).

There are two types of calorimeters depending on the nature of the incoming particle and how it interacts with matter, electromagnetic and hadronic. The former is focused on the energy measurement of electrons and photons while the latter measures the energy of the particles that escape the electromagnetic calorimeter, usually from jets originated from quark and gluon hadronization. The ATLAS calorimeters consist of layers of passive high density material, interleaved with layers of an active medium responsible of the signal generation. The electromagnetic calorimeter (ECAL) consists of accordion shape layers with lead as absorber and liquid Argon (LAr) [20] as active medium (the gas is ionized by the particles passing through). The ECAL has a barrel part (referred to it as ECAL barrel) and end-cap layers (electromagnetic end-cap or EMEC). On the other hand, the hadronic calorimeter is divided into the tile calorimeter (TileCal) [21] in the central region (and the extended TileCal barrel in the forward region surrounding the calorimeter end-caps) and the hadronic end-cap calorimeter (HEC). The TileCal absorber medium is made of steel and the active region is formed by scintillating tiles of polystyrene. The HEC is made of copper as absorption material and LAr as active medium. In the forward region, close to the beam pipe, one more calorimeter subsystem was installed (forward calorimeter - FCal). It consists on one electromagnetic and two hadronic calorimeters per side, with LAr as detection medium. The inner (electromagnetic) layer uses copper as absorber while the outer (hadronic) layers use tungsten. The full layout of the calorimeters on the ATLAS detector is shown in figure 3.3.

3.1.3 Muon Spectrometer

The Muon Spectrometer [23] is designed to measure the momentum of the muons. It is the outermost detector of ATLAS due to the fact that the muons can penetrate several meters of material before being stopped, hence they pass through the calorimeters and are measured in the spectrometer. It consists of a magnet system and four subdetectors: the Monitored Drift Tubes (MDT), the Cathode Strip Chambers (CSC), the Resistive Plate Chambers (RPC) and the Thin Gas Chambers (TGC). Similar to the other ATLAS subdetectors, the muon spectrometer is divided in the barrel part and the end-caps (see figure 3.4). The barrel part is composed of three layers of MDTs and two of RPCs while the end-caps are formed by the CSCs together with MDTs and the TGCs. The MDTs are composed of arrays of tubes that provide information of the trajectory of the muons. Thanks to the magnet system, the curvature of the trajectory is used to precisely deter-

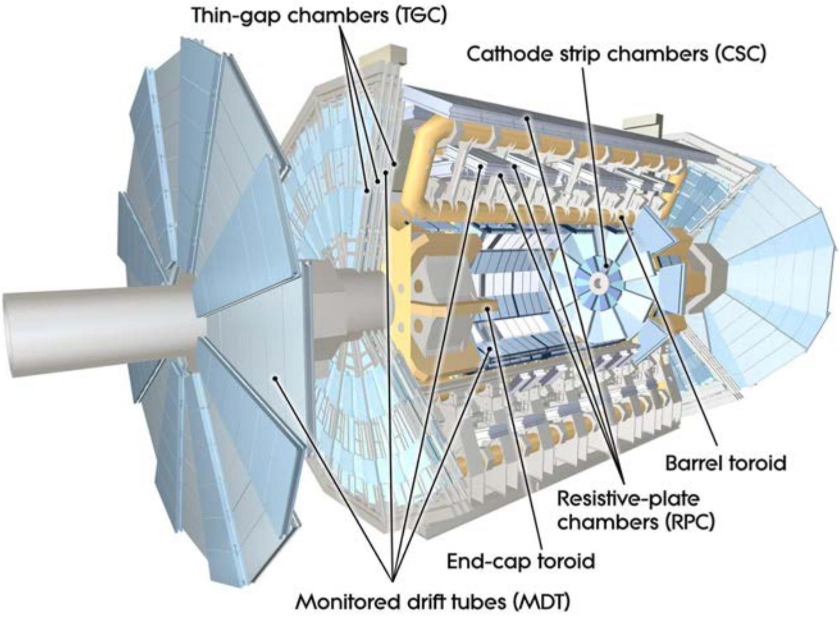

Figure 3.4: The ATLAS muon subsystem. Taken from [24].

mine the momentum of the muon. Each tube has a position resolution of 80 μm. The RPCs are used for muon triggering while also providing position measurements along the MDTs in the non bending direction by the magnet system. The CSCs assist the measurement of the muon momentum in the forward region thanks to a precise determination of the trajectory. They reach a resolution of 60 μm. The TGCs provide the triggering in the end-caps and also help with the determination of the trajectory. All these subsystems are filled with different gases (subjected to high electric fields), which are ionized by the traversing muons.

3.1.4 Magnet system

As mentioned before, the Magnet system is used to bend the trajectories of the charged particles, allowing to identify them and measure their momenta. The system consists of a solenoid magnet which surrounds the inner detector and three toroid magnets in the muon system, one barrel and two end-caps (see figures 3.1 and 3.4). The inner solenoid provides a magnetic field up to 2 T while the toroids can provide up to 4 T.

3.2 The current pixel detector and its upgrade for HL-LHC

The pixel detector [26][27] is the innermost part of the ATLAS detector closest to the interaction point. Due to this, the pixel detector plays a critical role in the reconstruction of the primary and secondary vertexes and in the determination of the impact parameter of the particle trajectories (which, in turn are fundamental for heavy flavor jet identification). The pixel detector is formed by three barrel layers (at 5.1 cm (layer 0 or B-layer), 8.9 cm (layer 1) and 12.3 cm (layer 2)) and six end-cap disks, three at each end of the barrel section. The sensors in the barrel layers and the end-caps consist of n-in-n planar silicon sensors with a pixel size of 50×400 μm^2 readout by the FE-I3 chip (see section 3.2.1 and 5.1). This was the pixel detector configuration at the start of LHC operation in 2009.

During the LS1 (2013-2015), a new layer of pixel detectors was inserted closer to the beam pipe at 3.2 cm, called the Insertable B-layer or IBL [28]. The objective of the new layer was to improve the impact parameter resolution (as already mentioned, critical for b-tagging). This layer also increases the redundancy of the pixel detector, ensuring high detection efficiency even after considerable aging. The sensors in the IBL are n-in-n planar silicon sensors (on the center of the barrel, corresponding to a 75% of the total IBL sensors) and p-type 3D silicon sensors (on the ends of the barrel), both with a pixel size of 50×250 μm^2 and readout by the improved FE-I4 chip (see section 3.2.1 and 5.1).

During the LS3 (2024-2026), the LHC is going to be upgraded for the high luminosity era (the HL-LHC) and most of the ATLAS detector systems will be upgraded. Concerning the pixel detector, the full ID will be completely removed and replaced by the new Inner Tracker Detector (ITk [29]). The objective of ITk is to improve the capabilities of the old pixel detector in terms of radiation hardness and position resolution. Due to the higher instantaneous luminosity of the HL-LHC a higher pile-up will appear around the impact point (∼200 inelastic proton-proton collisions per beam crossing versus the ∼50 during Run 1 and 2). An increased position resolution is mandatory to resolve the trajectories of all the particles involved in the collisions. Due to this higher number of collisions the radiation that the ITk has to sustain is also greatly increased. In order to cope with the new requirements and to maintain the same tracking performance as the present Inner Detector, the layout of the ITk requires an optimization.

The current design for ITk consists of five barrel layers, one end-cap barrel and five end-cap layers with pixel detectors as the innermost layers and four barrel and six end-cap discs with strip detectors (see figure 3.6). The pixel sensors on the central barrel layers are parallel to the beam pipe and placed at a distance of 39, 99, 160, 228 and 291 mm. The three outermost layers of the barrel have in addition an inclined section placed at a distance of 150, 218 and 281 mm with different angles (67°, 58° and 55° respectively). On

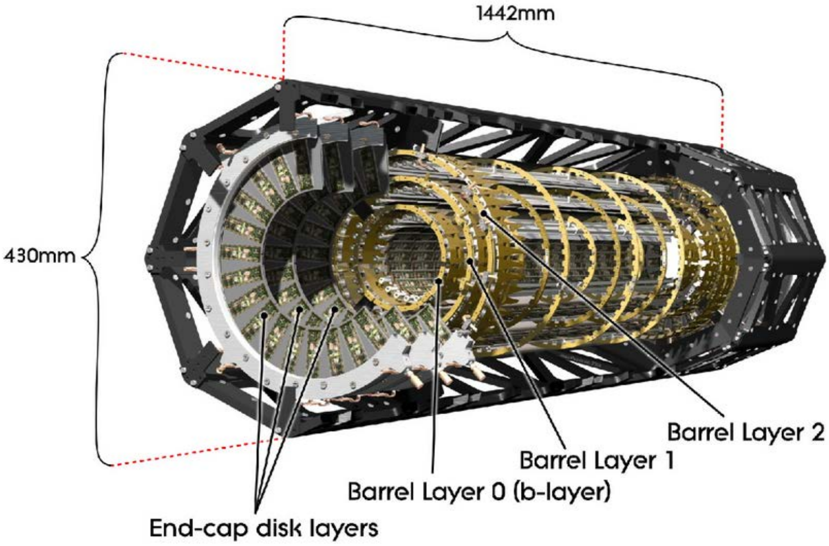

Figure 3.5: The ATLAS pixel detector subsystem. IBL is not represented in this figure. Taken from [25].

the end-cap barrel and layers the sensors are located in rings perpendicular to the beam pipe. The barrel is placed at 36.0 mm and consists of 17 rings. The layers are placed at 58.7, 80.0, 154.5, 214.5 and 274.6 cm and consist of 6, 24, 11, 8 and 9 rings respectively.

Thanks to the good performance of 3D sensors beyond a fluence of 5×10^{15} $\mathrm{n}_{eq}/\mathrm{cm}^2$ demonstrated in this thesis (in terms of radiation hardness and low power dissipation) this technology has been chosen as the baseline option for the innermost layer of the ITk detector. For the outer layers, the planar technology is the baseline option thanks to the higher fabrication yield and lower costs than 3D at the expense of higher operation voltage and power dissipation [67].

To work with 3D sensors in the innermost layer of ITk, the existing technology needs to be upgraded to cope with the increased radiation and occupancy. As mentioned before, IBL used 3D silicon sensors with a pixel size of 50×250 μm^2 with a distance between electrodes of 67 μm and a sensor thickness of 230 μm. For ITk it is required a smaller pixel size, thinner active areas and higher radiation tolerance. The thinner active area is needed to reduce the occupancy in the innermost layer and also helps to reduce the material budget (helpful to reduce the scattering on the detector). On the other hand, the thickness must also be large enough to ensure a detectable signal on the sensors (the collected charge is proportional to the thickness). The baseline active thickness foreseen is 150 μm, with an extra 100 μm passive substrate to ensure the robustness while handling and bump-bonding. The proposed pixel sizes are 50×50 μm^2 with 1 electrode per pixel and 25×100 μm^2 with 1 or 2 electrodes per pixel which means a distance between electrodes of 35 μm and 52 or 28 μm respectively (see section 6.2). The smaller pixel sizes with

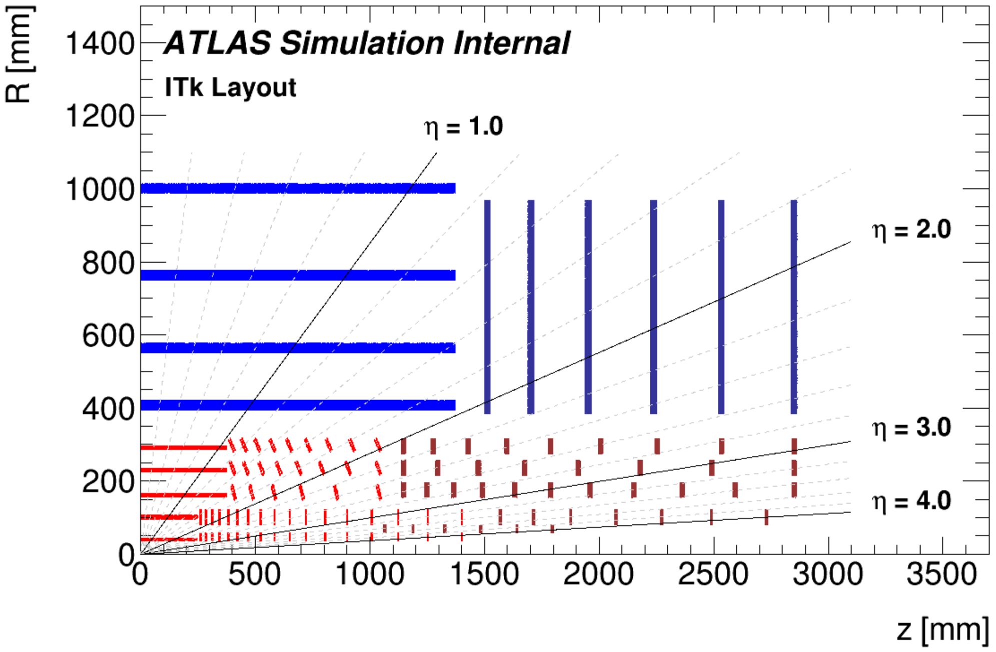

Figure 3.6: A schematic layout of the active detector elements on one quadrant of the ATLAS ITk. The (0,0) is the interaction point. The red elements are formed by pixel detectors while the blue are strip detectors. Image taken from [30].

respect to IBL are expected to deliver a higher tolerance to radiation damage.

3.2.1 The ATLAS pixel detector upgrade program

The ATLAS pixel detector during Run 1 is described in section 3.2. The pixel sensors used in the Inner Detector are readout by the FE-I3 chip. They have a pixel size of 50×400 with 3 electrodes per pixel, resulting on a distance between electrodes of 71 μm. The thickness of the pixel sensors is 255 μm. The maximum instantaneous luminosity on this phase of LHC is 10^{34} cm^{-2}s^{-1} which is translated to an expected dose on the innermost layer (at 5.1 cm of the interaction point) of 10^{15} n$_{eq}$/cm^2 or 100 Mrad[2] after the expected 5 years of operation.

During the LS2 the beam pipe inside the ATLAS detector was reduced in diameter to accomodate a new layer of silicon detectors at 3.2 cm (IBL). The sensors used in IBL are readout by the FE-I4 chip [42] and have a pixel size of 50×250 μm^2 with 2 electrodes per pixel, which means an electrode distance of 67 μm and have a thickness of 230 μm. Both the FE-I3 and the FE-I4 ASICs are discussed in section 5.1. A combination of planar (75%) and 3D detectors (25%) was used in IBL. The new pixel size keeps the same resolution in the r-φ direction while increasing the resolution in the z direction and

---

[2] See section 5.5 for the definition of the n$_{eq}$ unit and its converstion to rad.

improving the radiation hardness (required due to the increased proximity to the beam pipe) thanks to the reduction of the electrode distance. This configuration of the ATLAS pixel detector is used during Runs 2 and 3 where the maximum instantaneous luminosity is 2×10^{34} cm^{-2}s^{-1}. The expected fluence in IBL is 5×10^{15} n$_{eq}$/cm^2 or a dose of 250 Mrad. The FE-I4 chip also improves the FE-I3 in terms of readout speed, which reduces the inefficiency coming from dead time (saturation of the readout electronics), see section 5.1 and [28].

During the LS3 the upgrade of the LHC into the HL-LHC will be performed. The details of this upgrade were explained in chapter 2. Most of the systems of the ATLAS detector will be also upgraded (also known as upgrade Phase-2) and in particular the Inner Detector upgrade (to ITk) was described in section 3.2. Three pixel geometries for the pixel detectors are under discussion: 50×50 μm^2 with 1 electrode per pixel and 25×100 μm^2 with 1 readout electrode per pixel or 25×100 μm^2 with 2 electrodes per pixels. The advantages and inconvenients of each pixel size are described in section 6.2. These sensors will be coupled to the RD53 chip (the first prototype was named RD53A [43][44]). The chip has a pixel size of 50×50 μm^2 which is compatible with both pixel sensor geometries.

A peak instantaneous luminosity of 5×10^{34} cm^{-2}s^{-1} is expected during the HL-LHC era, meaning a fluence of 1.4×10^{16} n$_{eq}$/cm^2 (considering one replacement of the innermost layer and a safety factor of 1.5 [29]) and a maximum dose of 750 Mrad. Thus it is critical to demonstrate that the proposed 3D sensors with smaller pixel sizes provide the desired radiation hardness. However, the first prototype of RD53A ASIC was not fabricted until much later than the radiation hardness studies were needed. The main contribution of this thesis is to present the performance of small pitch 3D sensors using the FE-I4 ASIC and thus answer the critical question of radiation hardness and thermal performance.

Chapter 4

Silicon pixels in High Energy Physics

The semiconductor silicon detectors have been widely used in High Energy Physics (HEP) for tracking purposes. Thanks to the high granularity achievable with these detectors, the pixelated silicon sensors allow a high precision measurements of the particles' tracks. They also offer good radiation hardness, compactness and rate capability. For these reasons, they are an excellent option to measure the trajectories of particles in environments with a high number of collisions. They are capable of providing track and vertex reconstruction in the major LHC experiments, allowing to determine the momentum and direction of particles, distinguish the different particles in medium with high pile-up or identify jets coming from b quark hadron disintegration.

Since the role of the silicon tracking sensors on the experiments is critical, their reliability and performance has to be maintained over the lifetime of the experiments. One main challenge to face is radiation damage, which is highly present in an experiment like LHC and even more important in the HL-LHC phase. The silicon detectors are placed close to the interaction point of the experiments, where the radiation is dominated by charged hadrons from the primary interactions. This kind of radiation induces defects in the silicon bulk, which leads to a change of the effective doping concentration, an increase of leakage current and trapping of the signal charge carriers. Trapping is expected to be the limiting factor at the HL-LHC fluences leading to a large degradation of the signal. Due to the increase of the leakage current, the signal noise also increases. The combination of these two effects worsens the signal to noise ratio and may render the detector inoperable.

In this chapter, the operation of silicon detectors as particle detector will be explained. A generic explanation of a silicon detector is presented in section 4.1. The pn junction, the baseline technology to create a silicon detector is explained in section 4.2. The description of a segmented (pixelated) sensor is shown in section 4.3. The radiation damage induced in the detectors in HEP is covered in section 4.4. The effect of temperature cycles on the leakage current is described in section 4.5. Finally, in section 4.6, the 3D sensors are described.

4.1 Semiconductor detectors

A semiconductor is a material that behaves like a conductor under some conditions but acts like an insulator under different conditions. The periodic crystalline structure of a solid material defines discrete energy levels in which the electrons are confined. The last energy level with lowest energy which is filled with the outer shell electrons constituting the covalent bond between atoms is called covalence band. The levels with higher energy belong to the conduction band, where the electrons can move freely through the detector. In conductors, the energy bands overlap, allowing the free movement of the electrons in any conditions. For the insulators, the energy gap between the band is large, not allowing the movement of the electrons in the material. The semiconductors have a energy gap in the range of few eV (0 to 5 eV) hence a considerable amount of electrons can reach the conduction band at room temperature (the amount of electrons that can reach the conduction band changes with temperature). In semiconductors like silicon, if an electron has enough energy, it will move from the valence band to the conduction band leaving a hole behind. The other electrons in the valence band will move to cover this empty space. The hole can then be defined as a particle with positive charge moving freely in the valence band. For this reason, both the holes and the electrons contribute to the total charge carrier concentration. In intrinsic silicon at room temperature there are many electrons populating the conduction band. The large benefit of semiconductors is the possibility of introducing impurities into the silicon crystal structure (doping), and, as described below, by operating the device in a reverse bias, one can deplete the sensor of free carriers and be sensitive to small amounts of charge introduced by the traversing particles. Two types of doping are possible: if the silicon atom is replaced by an atom from group V in the periodic table it will be forming the bonding with neighboring silicon while giving a free electron to the crystal which is easily excited to the conduction band at room temperature (the atom that replaces the silicon is called donor because it has five valence electrons compared to the silicon which has four). In this case, the silicon doping is called n-type. The silicon can also be replaced by an atom from group III which gives to the material free positive carriers (holes). The atom that replaces the silicon is called acceptor because it has three valence electrons. This silicon doping is called p-type. Examples of donor atoms are phosphorous or antimony (P or Sb) while for acceptors is the Boron (B).

The principle of the semiconductor detectors is that a particle traversing the material ionizes de material creating electron-hole pairs inside the semiconductor bulk. These carriers move under the influence of an applied electric field to the electrodes implanted on the material. The energy deposited in the detector can be described with the formula

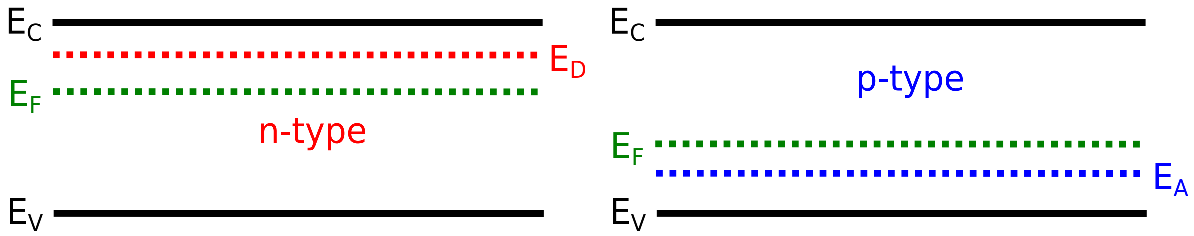

Figure 4.1: Energy levels in the n-type and p-type silicon. E_V and E_C represent the valence and conduction energy levels respectively. E_A and E_D is the energy levels introducing by donor and acceptor respectively. E_F is the level of Fermi, which is close to the middle of the band gap and close to the energy level introduced by the doping.

of Bethe-Bloch (see section 4.3). For silicon, the mean energy loss per flight path of a minimum ionizing particle (MIP) is of 3.87 MeV/cm (1.66 MeV $\text{cm}^2\ \text{g}^{-1} \times 2.3290\ \text{g cm}^{-3}$). The mean ionizing energy for silicon is 3.62 eV which is three times higher than the energy band gap ($E_g = 1.12$ eV). The difference is due to the generation of phonons which are dissipated as thermal energy. Considering a detector of 230 μm the signal produced by a MIP is obtained by multiplying the energy loss by the thickness and dividing by the ionizing energy. This gives a value of 2.46×10^4 e^-h^+ pairs. The intrinsic charge carriers in the silicon at room temperature is

$$n_i^2 = N_C N_V e^{-E_g/k_B T} \tag{4.1}$$

which leads to a concentration of 1.45×10^{10} cm^{-3}, which in a detector of 230 μm (and an area of 1 cm^2) give a number of 4.35×10^8 e^-h^+ pairs. Hence, the signal is masked by the thermal created pairs (the thermal noise is four orders of magnitude higher than the signal). To remove the thermal created pairs and hence increase the signal to noise ratio, a reversed biased pn junction is used.

4.2 The pn junction

A pn junction is a piece of silicon doped with donors (n-type) and acceptors (p-type) on two different sides. At the junction of the two regions, due to the different concentrations of carriers, the electrons and holes diffuse from the zones with high concentration to those of low concentration where they recombine with the opposite carriers thus creating a region almost free of charge carriers (depleted region). In addition, as the depletion zone is electrically charged by the donors and acceptors, an electric field that counteracts the diffusion appears near the junction, which is characterized by a built-in voltage V_{bi} (see figure 4.2). Once the pn junction is created, the size of the depletion zone depends on the levels of doping and the built-in voltage. The size of the depletion zone is given by the

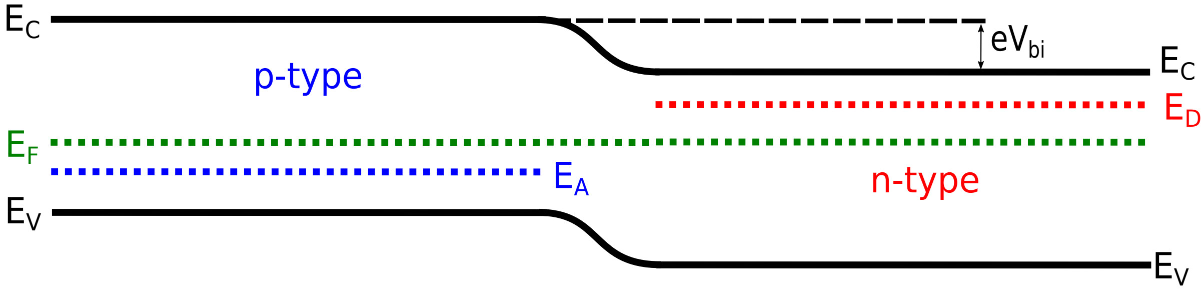

Figure 4.2: Energy levels in a pn junction. The Fermi energy E_F level of the p-type is at the same energy than for the n-type creating a zone where the conduction and valence bands are bent. Due to this bending, the built-in voltage V_{bi} appears in the center area (depletion zone).

equation

$$d = \sqrt{\frac{2\epsilon}{e}\frac{N_A + N_D}{N_A N_D}V_{bi}} \approx \sqrt{\frac{2\epsilon}{eN_{D/A}}V_{bi}} \quad \text{if } N_A >> N_D \text{ or } N_A << N_D, \tag{4.2}$$

with $N_{D/A}$ being is the smallest doping concentration. Equation 4.2 only depends on the smallest doping concentration and the built-in voltage (the simplification is done by assuming that one doping concentration is much higher than the other, which is the usual case). The depleted region free of charge carriers is where the detection of traversing particles takes place. To optimize the functioning of a detector, the depletion region has to be as big as possible. This region can be increased by applying an external reverse bias voltage (V_{bias}) to the junction which adds to the built-in voltage as on equation 4.3, hence increasing the size of the depletion zone. The voltage at which the full volume of the detector is depleted is named depletion voltage (V_{depl}), and it is the minimum desirable voltage to operate a silicon detector.

$$d = \sqrt{\frac{2\epsilon}{eN_{D/A}}(V_{bi} + V_{bias})}. \tag{4.3}$$

The depleted region will generate a current when the external voltage is applied. This current (in unirradiated sensors) is mostly due to thermal excitations in the depleted volume. The leakage current is then proportional to the depleted volume. In the ideal case, the leakage current increases with the $\sqrt{V_{bias}}$ until the depletion voltage is reached and stays in a plateau until it reaches the electrical breakdown. If the voltage is higher than the breakdown value, the charge carriers reach enough energy to create further electron-hole pairs and the leakage current increases very fast (see figure 4.3). The leakage current is a critical factor during sensor operation which can complicate the measurement of signal due to the introduction of noise. The temperature dependence of the leakage

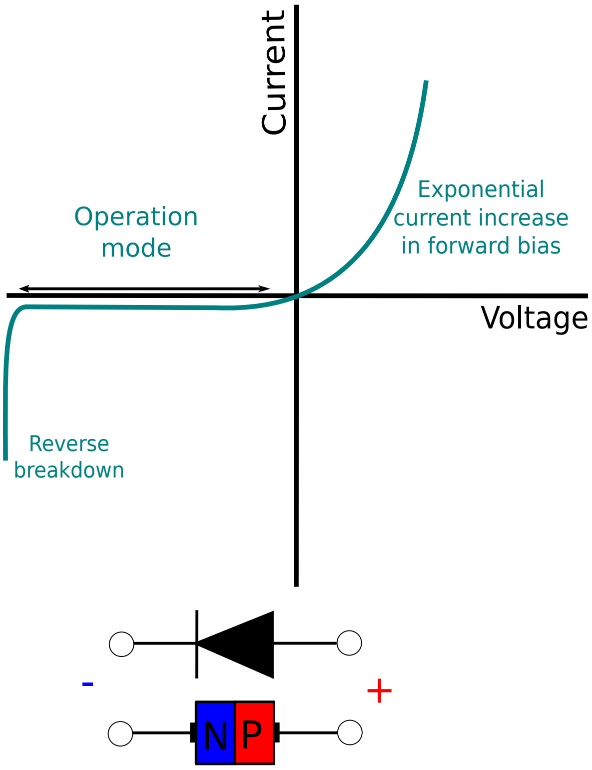

Figure 4.3: IV diagram of a pn junction (diode).

current follows the relation

$$I_{leak} \propto T^2 exp\left(\frac{-E_g}{2k_BT}\right), \tag{4.4}$$

hence, it is important to operate silicon detectors at low temperatures to reduce the leakage current specially after large radiation damage where there is the risk of thermal runaway. This equation is also useful to scale different measurements of leakage current to the same temperature (see section 6.6.4).

4.3 Pixel silicon detectors

Silicon detectors consist of a reverse biased pn junction, where particles crossing the silicon bulk create electron-hole pairs by ionization. The charge carriers are collected by heavily doped p-type and n-type regions (usually noted as p^+ and n^+, respectively), which play the role of electrodes. The most basic silicon detector is represented in figure 4.4 without pixel division (called pad diode). If a segmentation is performed in one dimension (parallel lines), the device is called strip detector and allows to measure trajectories in one dimension. A readout chip is connected in the end of the strips, connecting all the electrodes of the strip to read out channels in the chip. If the device is segmented in a two dimensional pattern, the device is called pixel detector and gives two dimensional

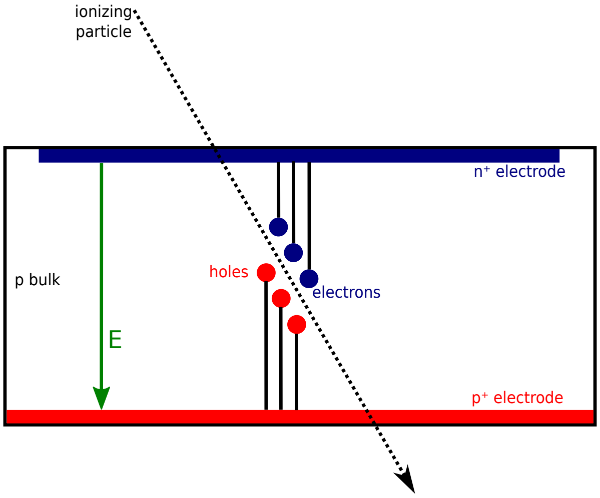

Figure 4.4: Sketch of a n-on-p pad diode with a ionizing particle producing e^-/h^+ pairs.

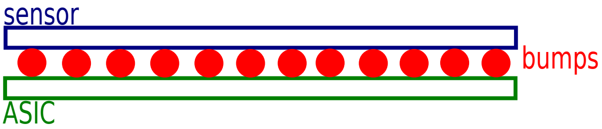

Figure 4.5: Sketch of a pixel detector connected via bump bonding to an ASIC (readout chip). Not to scale.

coordinates of the trajectories. The achievable pixel size is in the order of tens of micrometers, enough to give precision measurements in HEP experiments while coping with high particle densities and achieving high resistance to radiation. In pixel devices, all the electrodes are connected individually to a readout chip, via a complex process called bump-bonding (see figure 4.5).

Interaction of charged particles with silicon

Charged particles traversing a material lose energy by interacting with the electrons of the atoms that conform the material, hence continuously losing energy during their path through matter. For a range in momentum of $0.1 \leq \beta\gamma \leq 1000$ the mean energy loss per unit length (stopping power) can be described by the Bethe-Bloch [31] equation

$$-\left\langle \frac{dE}{dx} \right\rangle = Kz^2 \frac{Z}{A} \frac{1}{\beta^2} \left(\frac{1}{2} \ln \frac{2m_e c^2 \beta^2 \gamma^2 T_{max}}{I^2} - \beta^2 - \frac{\delta(\beta\gamma)}{2} \right) \tag{4.5}$$

where $K = 4\pi N_A r_e^2 m_e c^2$, A is the atomic mass of the absorber, Z is its atomic number, I is the mean excitation energy of the medium (in silicon 3.62 eV), T_{max} is the maximum single collision energy transfer, $\beta = v/c$, $\gamma = 1/1\text{-}\beta^2$ is the Lorentz factor and $\delta(\beta\gamma)$ is a density effect correction to the energy loss [32]. Figure 4.6 shows the stopping power of muons,

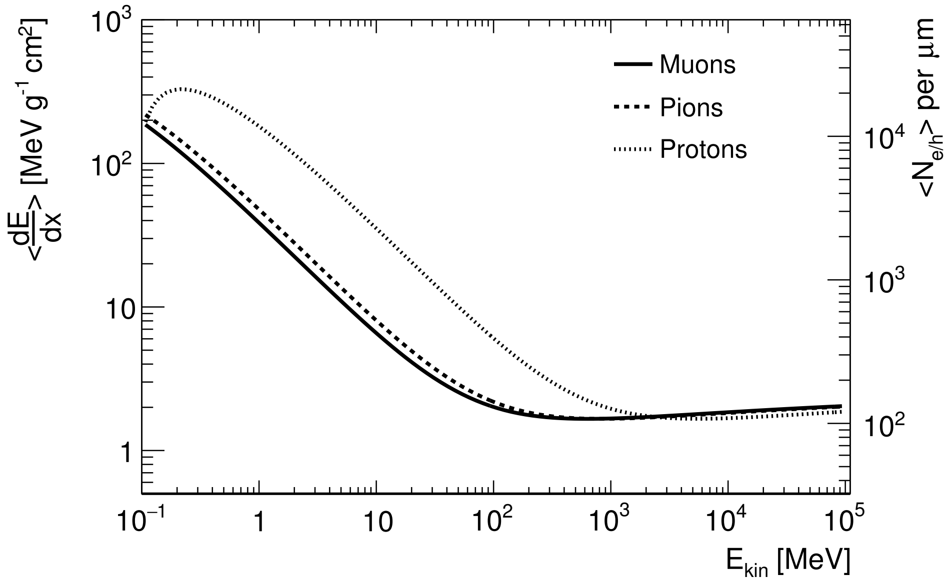

Figure 4.6: Average stopping power of muons, protons and pions in silicon and average number of electron/hole pairs per micrometre as a function of kinetic energy. Taken from [34].

pions and protons in silicon using Bethe-Bloch equation. A minimum in the distribution is observed, which is almost a plateau for several orders of magnitude of momentum. Particles with this minimum momentum are named minimum ionizing particles (MIP). A MIP in silicon has an average stopping power of 1.66 MeV cm^2 g^{-1} (107 e/h pairs per μm). Due to the slow increase in energy loss ratio, most relativistic particles detected in ATLAS have a stopping power similar to a MIP, and in general, can be considered as such. To do laboratory measurements for charge collection determination, electrons of $\sim$2 MeV energy from β radioactive sources (like ^{90}Sr) are used, since these electrons are already MIPs in silicon.

The energy loss probability distribution follows, in good approximation, a Landau distribution [33]. This distribution features long tails which experimentally affect the calculation of the mean energy loss. Therefore it is common to quote the most probable value (MPV). The MPV of the Landau distribution from a particle can be obtained by the following expression [31]

$$\Delta_p = \xi\left(\ln\frac{2m_e c^2\beta^2\gamma^2}{I} + \ln\frac{\xi}{I} + 0.200 - \beta^2 - \delta(\beta\gamma)\right), \tag{4.6}$$

with ξ = (K/2)Z/A(x/β^2) MeV for a detector with a thickness x in units of [g cm^{-2}]. Thus, the most probable energy loss over thickness Δ_p/x varies as a function of the thickness of the material as $a\ln x + b$. The energy deposition distribution for 500 MeV pions at different silicon thickness can be seen in figure 4.7. For instance, in 230 μm thick

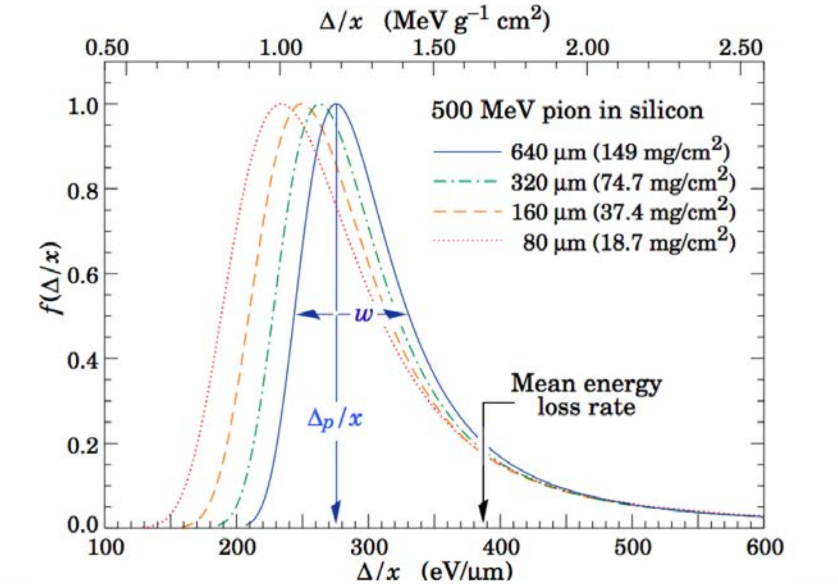

Figure 4.7: Energy deposition distribution for 500 MeV pions at different silicon thickness normalized to the most probable value of each distribution. Taken from [31].

silicon, the most probable energy loss for a MIP is $\Delta_p/x = 1.06$ MeVcm^{2}g^{-1} (69 e/h pairs per μm).

Charge collection

The particles going through the silicon sensor generate a number of free charge carriers which is proportional to the energy deposited by the particle. These carriers generated in the silicon bulk are under the influence of the depletion electric field and drift towards the electrodes with a drift velocity given by equation

$$v_{drift,e/h}(E) = \mu_{e/h}E \tag{4.7}$$

being e/h the type of charge involved (electrons or holes), E the value of the electric field and μ the mobility of the charge in the medium ($\mu_e = 1350$ cm^2 V^{-1} s^{-1} and $\mu_h = 480$ cm^2 V^{-1} s^{-1} at 300 K). The movement of the charge causes an induced current i in the read out electrode, given by the Shockley-Ramo theorem [35][36]:

$$i(t) = q\vec{v}_{drift,e/h} \cdot \vec{E_w} \tag{4.8}$$

with q the moving charge, v_{drift} its drift velocity and E_w is the weighting field of the read out electrode, which is defined as the negative gradient of the weighting potential, in turn obtained by solving the Laplace equation:

$$\nabla^2\phi_w = 0 \tag{4.9}$$

with ϕ_w a unit potential in the read out electrode and a zero potential to all the other electrodes. The integral over time of the induced current results in the collected charge

$$Q = \int_{t_1}^{t_2} i(t)dt = e\Delta\phi_w. \tag{4.10}$$

When all charge carriers reach the electrodes, the collected charge is equal to the number of generated electron/hole pairs (full charge collection), but after irradiation part of the charge carriers might be trapped during the collection time, resulting in charge collection efficiency loss (see section 4.4.2). If the charge falls below a certain value (or threshold), the signal is not propagated to the readout electronics and the particle is not detected. This is the reason why is so important to study how radiation limits the performance of the sensors.

4.4 Radiation effects

In HEP experiments, the silicon atoms of the pixel detectors are hit by multiple particles. The particles that penetrate the silicon sensor can scatter with the atoms of the crystalline structure and modify it. Hence, it is critical to understand how these particle interact with the silicon structure (referred to as radiation damage). The damage can be produced in the silicon bulk and in the interface with the SiO_2 layer (which is used in insulator layers and is also deposited on the sensor surface for protection). The defects created in the sensor are classified in bulk and surface defects. In HEP, the most important contribution comes from the bulk defects, but the surface defects have to be taken into account since they may create a positive charge density on the surface which attracts electrons (leading to a compensating effect of the doping between the implants).

The bulk defects are produced by high energetic particles which interact with the nuclei of the silicon atoms. If a colliding particle transfers an energy larger than 25 eV to a nucleus, it can be displaced from its original position in the crystal structure, thus creating a non reversible defect which can be charged and change the electrical properties of the material. As a result of this displacement a vacancy is left in the crystal and the recoiling atom can either move to an interstitial lattice position or, if the energy of the first particle is large enough, travel in the crystal displacing other atoms and creating further point-like defects. In case the transferred energy exceeds 2 keV, the atoms lose most of their energy in a localized area at the end of their path in the crystal, leading to so-called cluster defects [37]. The accumulation of these bulk effects create new energy levels, and with enough radiation damage, the electrical behavior of the sensor can deteriorate. The e^-/h^+ pairs that the MIPs generate in the bulk can be trapped in the crystal due to the new energy levels, hence reducing the charge collected. Also the leakage current is

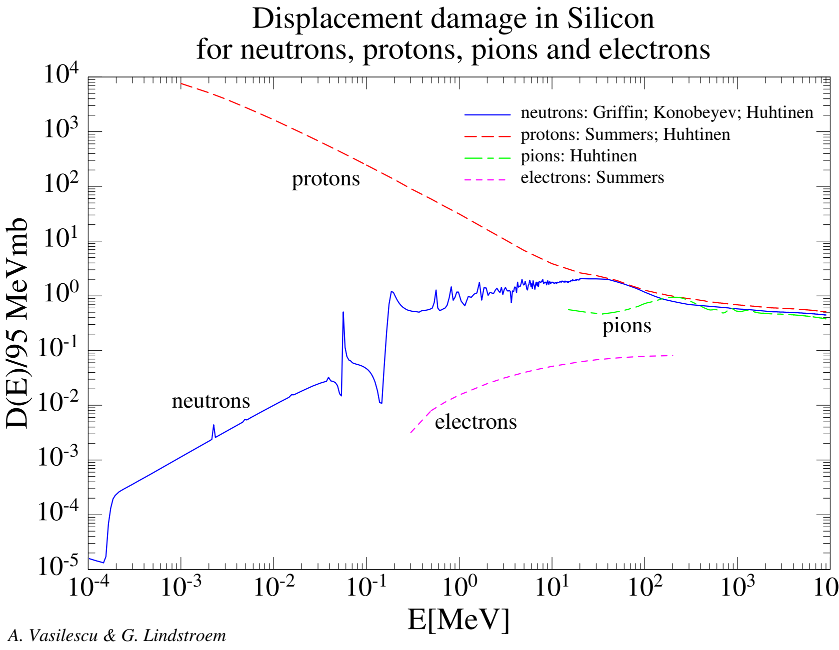

Figure 4.8: Displacement damage cross section for different particle types as a function of energy, normalized to 1 MeV neutrons. Taken from [38].

increased and the effective doping concentration is changed (hence changing the voltage required to deplete the bulk).

4.4.1 The NIEL Scaling Hypothesis

Since the interactions between neutral and charged hadrons with the silicon crystal differ, the resulting bulk defects depend on the radiation type. In order to parametrize and compare radiation damage effects caused by different types of particles and energies, the bulk radiation damage is expressed in terms of Non-Ionizing Energy Loss (NIEL) damage. The NIEL assumes a correlation between the amount of displacement damage with the energy transferred in the collision, hence removing the dependence of the particle type and the interaction process. The irradiation dose is measured in terms of particle fluence ϕ (number of particles per unit area) and it is typically scaled to the equivalent fluence of reference particles (1 MeV neutrons) with the same NIEL using the equation

$$\Phi_{eq} = \kappa\Phi = \kappa \int_{E_{min}}^{E_{max}} \Phi(E)dE \tag{4.11}$$

where κ is the hardness factor which, for each particle and energy, scales the displacement-damage integrated over the energy spectrum, to the 1 MeV neutrons equivalent. κ is obtained by weighting the fluence with an energy dependent damage cross section D(E) (see figure 4.8) and normalized to the integrated fluence and the damage cross section of the reference particles ($D(E_n = 1$ MeV$) = 95$ MeV mb):

$$\kappa = \frac{\int_{E_{min}}^{E_{max}} D(\mathrm{E})\Phi(\mathrm{E})\mathrm{dE}}{D(\mathrm{E}_n = 1\mathrm{MeV}) \int_{E_{min}}^{E_{max}} \Phi(\mathrm{E})\mathrm{dE}}. \tag{4.12}$$

4.4.2 Impact on sensor performance

As mentioned before, one consequence of the radiation induced impurities is the appearance of new energy levels in the band gap which produce three main effects: a change in the doping concentration an increase of the leakage current and a high probability of capturing the charge carriers moving in the silicon bulk (trapping).

Doping concentration

One effect of the bulk radiation damage is the variation of the doping concentration. An effective doping concentration can be defined as the difference between donors and acceptors ($N_{eff} = N_D - N_A$). The introduction of new energy levels in the band gap by radiation damage act as acceptors and after enough irradiation can change the dominant doping type in the bulk in n-type dope silicon, known as type inversion. In the case of p-type doped silicon (like the devices of this thesis) the type inversion does not happen. The doping concentration affects the depletion voltage for both doping types, as $V_{depl} \propto N_{eff}$ (see equation 4.3) and in case of p-type doping, the depletion voltage increases as a function of irradiation, hence a higher voltage is required to reach the full depletion of the bulk.

Leakage current increase

The appearance of new energy levels close to the middle of the band gap act as generation centers increasing the probability for electrons to be excited into the conduction band. This leads to an increase of the leakage current ΔI generated in the active volume of the semiconductor V which is proportional to the fluence Φ with the equation:

$$\Delta I_{leak} = \alpha \Phi V \tag{4.13}$$

with α being the current-related damage rate (see section 4.5), which is independent of the initial resistivity of the silicon, the doping concentrations and the type of irradiation. Also, as shown in equation 4.4, the leakage current depends also strongly on the temperature. Hence, after high irradiation doses, the increase of the leakage current can lead to the heating of the sensor and a consequent thermal runaway that would destroy the junction. To avoid this effect the detectors need to be properly cooled. Also, a reduced leakage current reduces the noise and the power consumption. The dependence of the leakage current with fluence and temperature is shown in section 6.6.

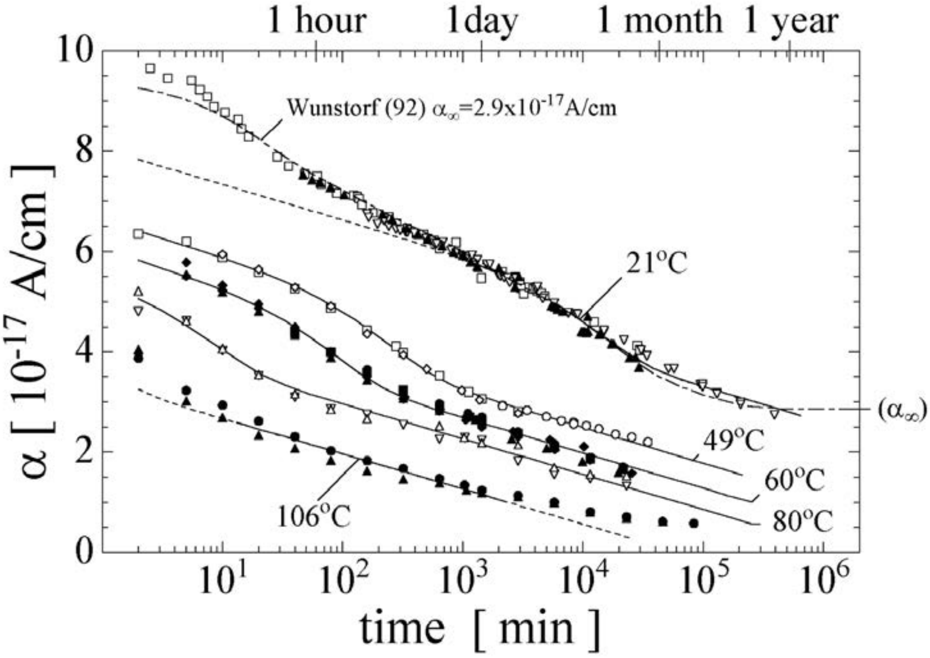

Figure 4.9: Damage rate constant α with respect to annealing time for different temperatures. Taken from [39].

Trapping

The defects in the silicon bulk can act as trapping centers because the energy levels created in the energy band gap can absorb the charge carriers, thus reducing the signal in the detector. The trapping is expected to be the main limiting factor for pixel sensors at the HL-LHC for fluences above 10^{15} n_{eq}/cm^2 because it reduces the Charge Collection Efficiency (CCE) which is defined as the ratio of the collected charge Q to the collected charge Q_0 measured at full depletion before irradiation (see figure 6.12 right).

4.5 Annealing

The previously defects created by radiation in the silicon bulk are not static, as they can evolve in the crystal structure, reacting with other defects or impurities or forming new defect structures. This evolution of the defects depends on time and temperature [39]. The effect of annealing in the damage rate constant α is illustrated in figure 4.9 and is always beneficial since it leads to a decrease of leakage current following the equation 4.13. On the other hand, the effective doping concentration (N_{eff}) also varies with the annealing time (see figure 4.10, starting with an initial short term beneficial annealing (few days) and a reverse annealing appearing in the long term (leading to a higher depletion voltage

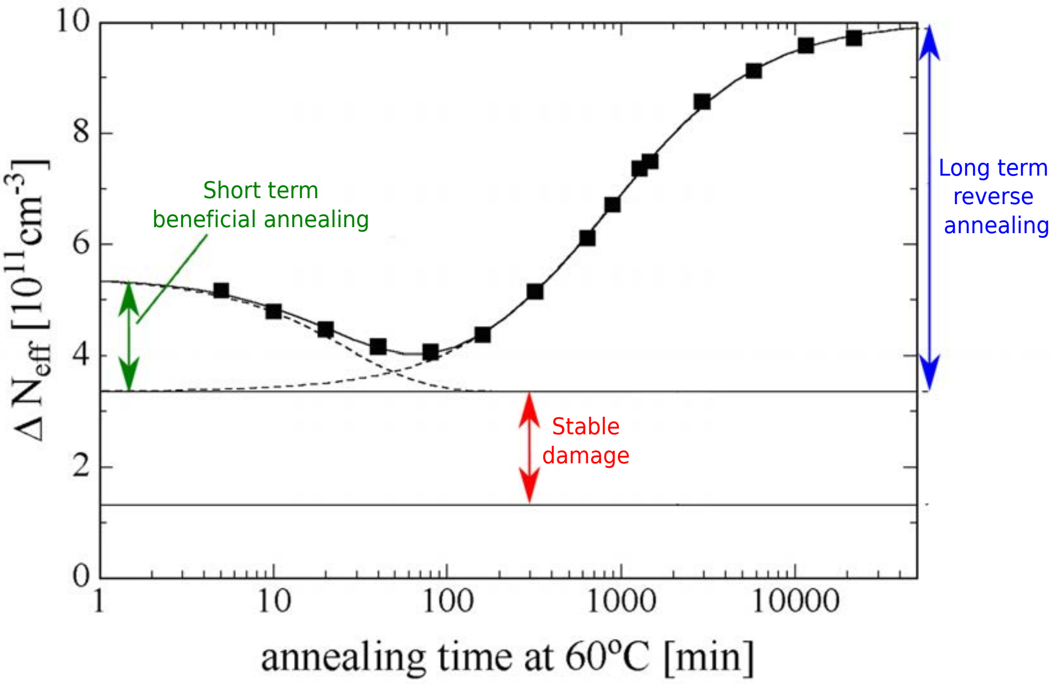

Figure 4.10: Effect of the annealing at 60 °C on the effective doping concentration. The beneficial annealing is shown in green and the reverse annealing in blue. A stable damage effect (red) is not affected by annealing. Adapted from [39].

($V_{depl} \propto N_{eff}$)). In particular, for p-type sensors, the V_{depl} decreases during the beneficial annealing and increases again for reverse annealing. Due to this behavior, the irradiated sensors studied in this thesis were usually annealed at room temperature during seven days to benefit from the short term annealing and kept at temperatures lower than 0 °C during storage and operations to avoid a degradation due to the long term annealing effect. This annealing procedure is standardized across the silicon community to compare the performance of irradiated sensors. Otherwise, results could be sensitive to small variation of annealing time related, for example, to handling of samples during transport or testing.

4.6 3D sensors

3D silicon sensors were first introduced in 1997 as an idea to improve the existing planar silicon sensors [40][41]. The novelty of 3D silicon pixel detectors is that the electrodes are shaped like columns penetrating the silicon bulk, while in the planar sensors the electrodes are implanted in the surface of the silicon (see figure 4.11). The fabrication of the 3D columns is achieved thanks to very precise etching techniques that allow to produce very thin and deep columns into the silicon. The advantage of 3D versus planar

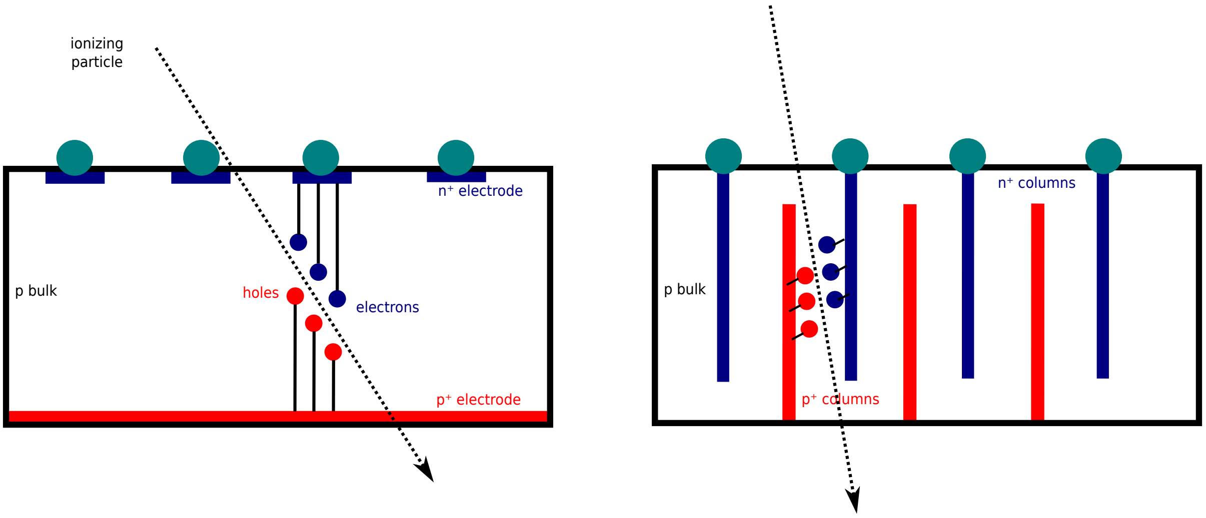

Figure 4.11: Comparison between a planar (left) and a 3D (right) sensor design.

is that, in planar, the distance between electrodes is defined by the active thickness of the silicon sensor while, in 3D, the distance between electrodes is disentangled from the thickness. Thanks to this, the 3D technology can provide small inter-electrode distances while keeping high charge collection (which depends on the thickness of the device) hence lowering the depletion voltage and thus lowering power dissipation. Also, thanks to the reduced inter-electrode distance, the probability of charge carriers to be trapped by radiation induced defects is reduced, making the 3D technology more radiation hard. The disadvantages of the 3D technology is that the production yield is lower and requires more production steps than planar sensors, which increases the cost of 3D.

Fabrication

In this section the fabrication process is briefly described (see figure 4.12). A polished p-doped silicon wafer is covered by a thin layer of SiO_2 by wet oxidation: water vapour at very high temperature (1000 °C) is used to grow an oxide layer. A photo-resist is deposited over the silicon dioxide and illuminated with UV light through a mask leaving open regions where the p-stop[1] will be implanted with boron ions. Columns of high aspect ratio of about 20:1 are etched in the silicon via a Deep Reactive Ionization Etching (DRIE) process. It consists of a series of alternating steps of plasma etching and a deposition of a passivation layer. The passivation layer protects the side-walls of the column from being further etched by the plasma, with the wafer oxide and photo-resist layers acting as a protection mask. After the etching of the columns has finished, the holes are partially

---

[1] High dose p^+ implantation surrounding the electrodes to isolate them, preventing unwanted currents between neighboring electrodes.

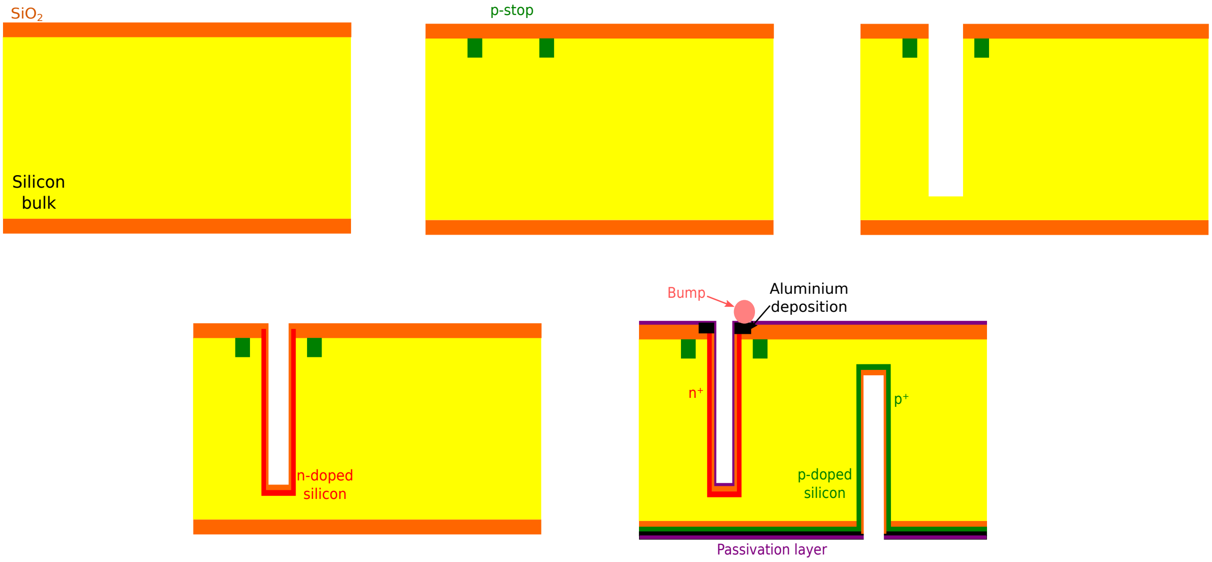

Figure 4.12: Sketch of the fabrication process of a double-sided 3D pixel sensor.

filled with silicon and doped with phosphorus ions to create the n$^+$ columns. A SiO$_2$ layer is grown afterwards in order to protect the n-doped region. The p$^+$ column is fabricated similarly to the n$^+$ column, although this time the doping ions are boron atoms.

In a double sided process the p$^+$ columns are etched from the back side of the wafer. Later, the columns on the back side are covered with aluminum to facilitate the electrical contact and the full wafer surface is passivated.

Chapter 5

Instrumentation and experimental methods

In this chapter the experimental setups and the methodology used to obtain the results presented un this thesis are discussed. In section 5.1 the different types of front-end chips are described and in section 5.2 the readout systems that allow the chip calibration and the data taking operations are detailed. The chip calibration procedure and the method to calculate the charge deposited in the sensor is described in section 5.3. A description of the beam telescopes and the technique to calculate the hit efficiency of the sensors is discussed in section 5.4.

5.1 Application-specific integrated circuits (ASICs)

The front-end (FE) chips (or ASICs) play a critical role in the overall performance of pixel devices. The signals provided by the pixel sensor are usually very small and need to be amplified and discriminated. The FE chip are thus connected to the pixel sensor in very close proximity through solder bumps (one bump per pixel). The sensor assembled with the ASIC is then glued and wire bonded to a Printed Circuit Board (PCB). The signal is then processed in the ASIC and then read out through the PCB by the DAQ system. The processes used to mount the devices will be explained more in detail in sections 6.3 and 6.4. The PCB is connected to one of the two readout systems described in section 5.2. As already mentioned, the ASICs used for the work in this thesis were the FE-I3 and the FE-I4, being the FE-I4 the most important since it is a superior chip in terms of performance and size.

The FE-I3 [47], shown in figure 5.1, contains 2880 pixels with a pitch of 50×400 μm^2 in an array of 160 rows and 18 columns resulting on an active area of 0.58 cm^2. It is produced in a 250 nm CMOS and its full size is 0.76×1.08 cm^2. The active area represents a 71% of the chip. Each pixel channel has an analogue and a digital part. In the analog part,

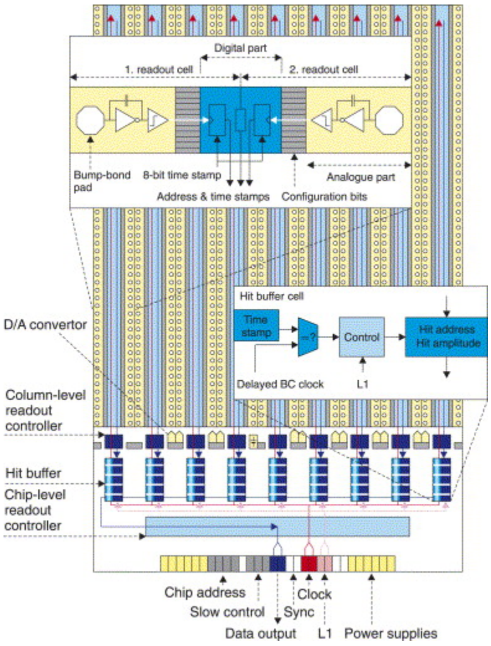

Figure 5.1: Overview of the elements in the FE-I3 pixel readout chip [47]. The active area represents a 71% of the chip.

the sensor charge signal is amplified and compared to a programmable threshold by a discriminator. In the digital part the pixel address and the times when the rising edge and the falling edge of the signal cross the threshold are registered. The pixel columns are connected in pairs to a buffer at the periphery of the chip where the digitised information is collected and transferred. In this area of the chip, called end of column (EOC), the Time over Threshold (ToT) is calculated and stored in an 8-bit register. The hit data are then matched to the trigger signal and transmitted serially out of the chip. Close to the EOC, a series of wire-bond pads provide contacts for powering the analog and the digital parts of the chip and for its communications. The digital part of the chip consumes ~20-40 mA from a 2 V supply while the analog part consumes ~60-80 mA from a 1.6 V supply resulting in ~100 mA (34.7 μA/channel). To fulfill the ATLAS requirements, the FE-I3 has a clock speed of 25 ns, which matches the nominal LHC frequency, and was designed to be radiation hard up to 10^{15} n_{eq}/cm^2 (100 Mrad). The standard threshold (see section 5.3.1) is 3.0 ke$^-$ with a noise of ~200 e$^-$ but the devices were shown to work at 1.5 ke$^-$.

The FE-I4 [48], shown in figure 5.2, has 26880 pixels with at pitch of 50×250 μm^2 in an array of 336 rows and 80 columns which results on an active area of 3.36 cm^2. It is designed in a 130 nm CMOS process and its full size is 2.0×1.9 cm^2. The active area represents a 88% of the chip. As for the FE-I3, each pixel consist of an analogue and a digital part. The analog part (figure 5.7) contains the amplifier for the charge signal, the discriminator and the injection system (see section 5.3.3) and is optimized for low noise

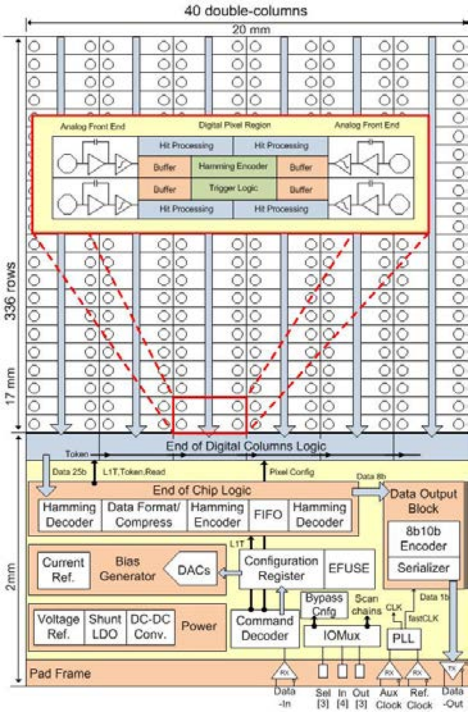

Figure 5.2: Overview of the elements in the FE-I4 pixel readout chip [42]. The active area represents a 88% of the chip.

which allows to set the threshold to values lower than the FE-I3. The standard threshold is 1.5 ke$^-$ with a noise of ∼100-150 e$^-$ while the minimum operational threshold achieved was 1.0 ke$^-$ in devices where the FE-I4 is connected to a sensor. The digital part is shared among four pixel channels. Differently from the FE-I3, the hit information is processed in a local buffer where the ToT is computed and stored in a 4-bit register. The trigger signal is also forwarded to this digital block and data are transmitted to the EOC in time with the trigger. Since the trigger verification is performed within the region, hits that do not belong to a trigger are discarded before being sent to the periphery. Therefore the dead time during the column readout is significantly decreased and at the same time a lower power consumption is achieved. On one side of the chip, wire-bond pads for communication and powering are implemented. The digital part of the chip consumes ∼120 mA from a 1.3 V supply and the analog part consumes ∼350 mA from a 1.6 V supply for a total of ∼400-500 mA (about 4μA/channel). The FE-I4 has a clock speed of 25 ns and was designed to be enough radiation hard to work in the IBL conditions, with a fluence of 5×10^{15} n$_{eq}$/cm^2 (250 Mrad).

For the characterization of the modules, two dedicated Printed Circuit Boards (PCBs), allow the readout of the FE-I3 (designed by INFN-Genova) and the FE-I4 chips (designed

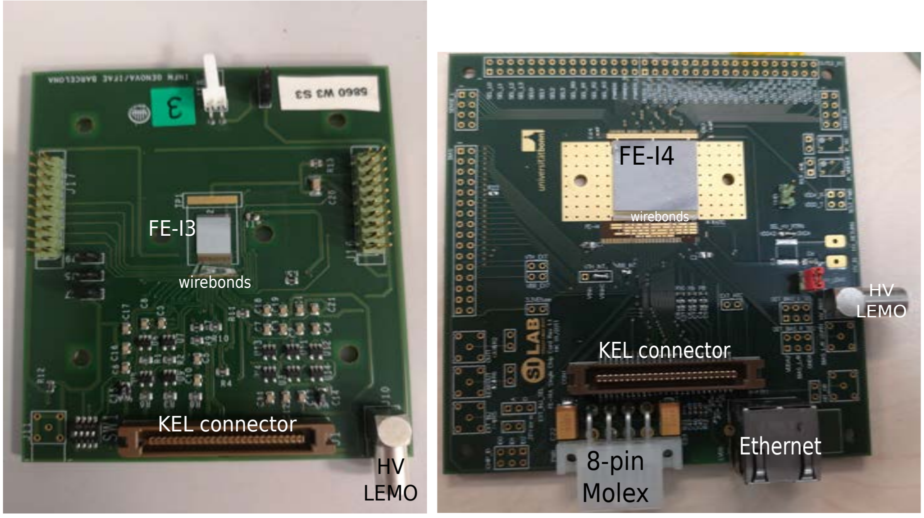

Figure 5.3: (Left) Picture of a single chip card with the FE-I3 device on top. (Right) Picture of a single chip card with the FE-I4 device on top.

by the university of Bonn) (see figure 5.3). They are equipped with a LEMO[1] connector that provides the bias voltage to the sensor and a KEL connector to send both analog and digital voltages together with the data stream. The FE-I4 single chip cards have in addition the possibility of routing the data stream via an ethernet cable while providing analog and digital low voltages for the chip on a separate 8-pin connector.

5.2 Readout systems

The bare-assembly sensors under study are usually mounted on a electronic board (printed circuit board or PCB) that facilitates handling and testing. For the chip calibration procedure and data taking the device board can be connected to two different readout systems. These are the HSIO-II and the USBPix and they are described in the following lines.

HSIO-II

The High Speed Input/Output II (HSIO-II) [45] is a DAQ system developed at the Stanford Linear Accelerator Center (SLAC) for ATLAS pixel development and upgrade applications which provides high speed data handling. The HSIO-II pixel module readout is shown in figure 5.4. The HSIO-II is connected via an Ethernet cable directly to a computer where the data is stored. Two dedicated software packages installed on the computer are used to communicate with the module: the calibGUI allows the chip cal-

---

[1] www.lemo.com

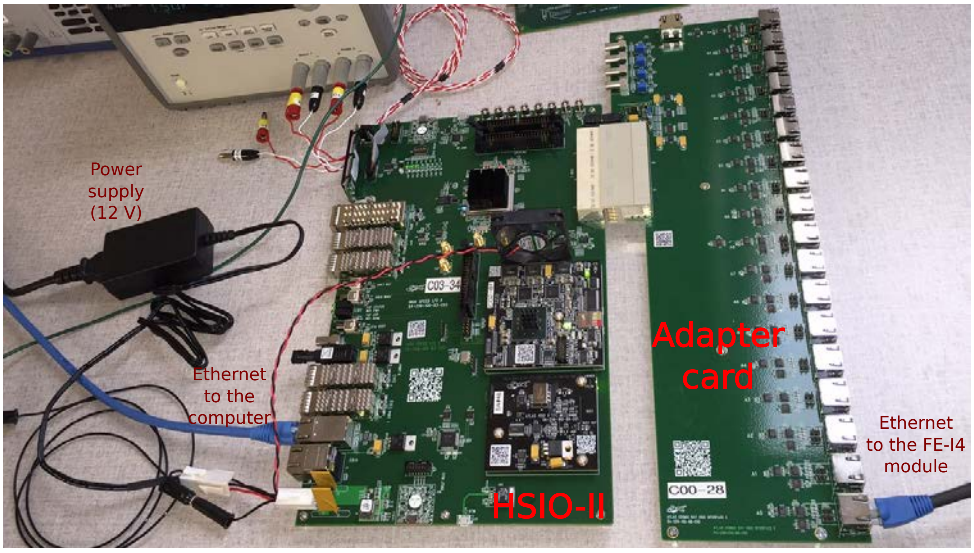

Figure 5.4: (Left) The HSIO-II readout board. (Right) The HSIO-II adapter card.

ibration and scans procedures to verify the calibration results (see section 5.3) and the cosmicGUI which provides an interface dedicated to beam test applications. The HSIO-II board is powered by an AC to DC power supply that ends in a 4-pin connector with 12 V. An adapter card is attached to the HSIO-II that allows to handle up to eighteen FE-I4 modules. The communication with the modules is done via an Ethernet cable, which manages the trigger signals and the data stream of the pixel modules.

USBPix

The USBPix [46] is a modular readout system based on a multi-purpose input/output Field-Programmable Gate Array (FPGA) board (Multi-IO board) designed by Bonn University for the ATLAS pixel community. The readout system is completed by dedicated adapter cards which offer the possibility of connecting either FE-I3 or FE-I4 chips. A setup for USBPix attached to a single FE-I4 chip card is shown in figure 5.5 with the adapter card of the FE-I3 below. The Multi-IO board handles the signal transmission to the chip and provides connections to the computer via the Universal Serial Bus (USB) protocol. The USBPix board is powered via a 4-pin connector at 2 V. An external trigger input connection via ethernet or LEMO is also available. The adapter cards are equipped with a KEL[2] connector which enables data flow and powering. In the case of the FE-I4 adapter there is also the option of an Ethernet connector for the data and a 8-pin connector for the analog and digital voltages. The system is controlled by a computer with the STControl software [46] which provides full access to the chip DAC registers as well as different calibration algorithms with adjustable parameters and scan procedures to verify

---

[2] www.kel.jp

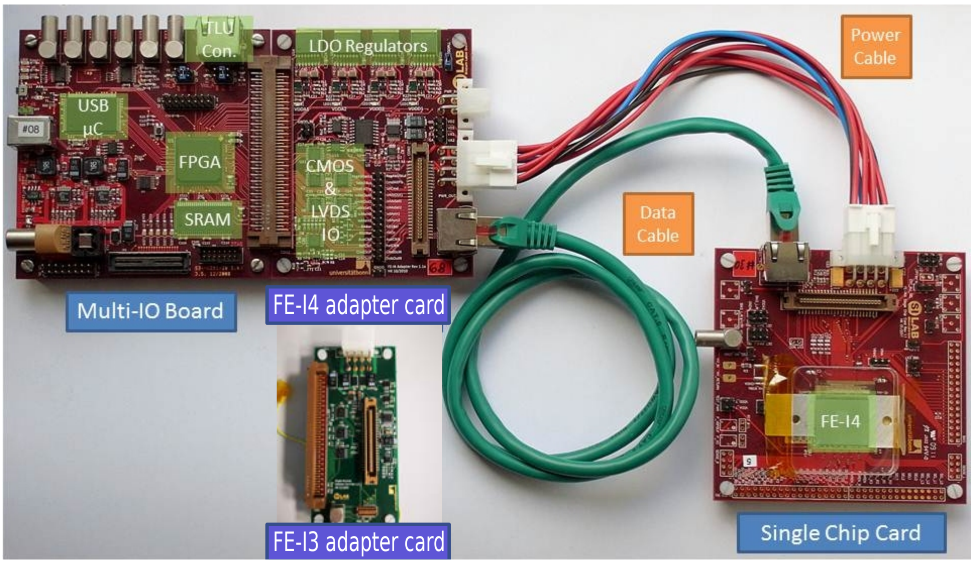

Figure 5.5: The USBPix setup with a FE-I4 single chip card with an adapter card for FE-I3 below (image adapted from [46]).

the calibration results.

5.3 Chip calibration

In this section the calibration procedure of the chip will be explained. The calibration procedure can be performed with any readout system and works in a similar way for both generations of chips. As shown in figure 5.7, each pixel channel has a discriminator which determines a threshold below which the collected charge is not registered. On the other hand, the ToT depends on the feedback current of the circuit, which changes the fall time of the signal. In figure 5.6 top, an example signal where the threshold and the ToT are indicated is shown. Due to production variations over the chip surface, the DAC settings needed to calibrate both ToT and threshold vary for each pixel. Hence, to homogenize the behavior and reduce the dispersion of the parameters, the calibration of the chip is needed. Figure 5.6 bottom shows how ToT and threshold are connected; a high or low charge modifies the ToT at a fixed threshold, a change on the threshold Digital to Analogue Converter (TDAC) changes the ToT, and a change of the feedback current DAC (FDAC) affects the ToT. Also, since the FDAC is placed before the discriminator which determines the threshold, a change in the FDAC modifies the threshold. Therefore, to do a proper calibration, an iterative procedure is needed to achieve an uniform tuning of both parameters.

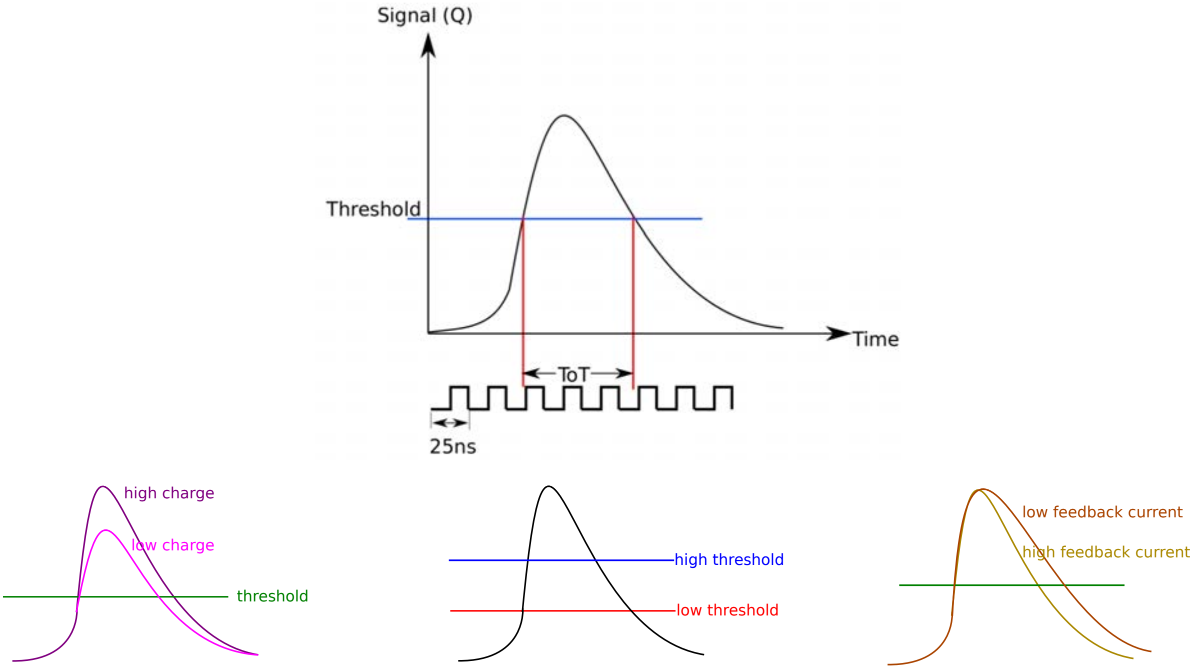

Figure 5.6: (Top) Description of threshold and tot over an example signal. (Bottom) Dependance of the preamplifier output signal from the settings of injected charge, threshold and feedback current.

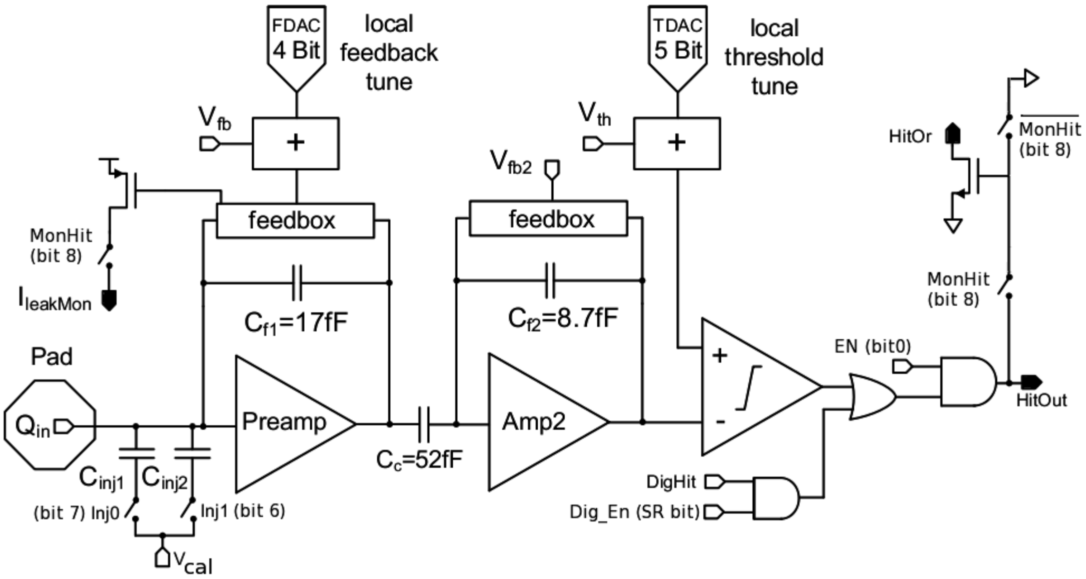

Figure 5.7: The analog circuit of a pixel in the FE-I4 readout chip [42].

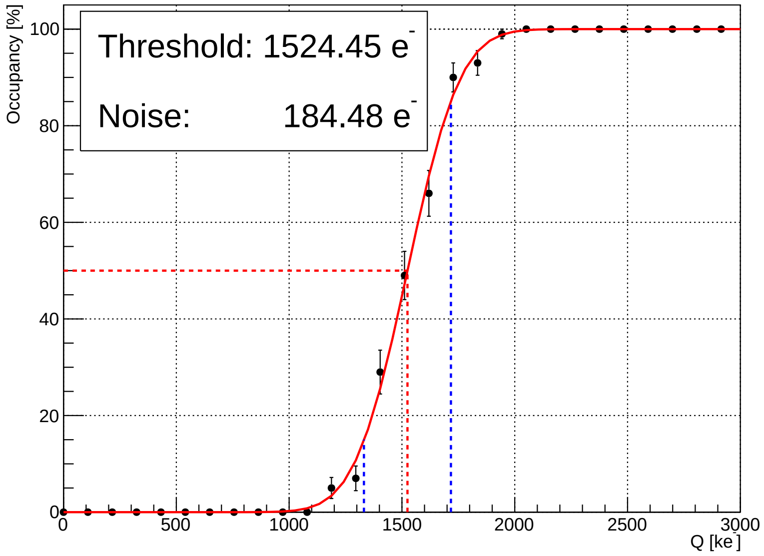

Figure 5.8: Threshold measurement for a single pixel of a FE-I4 chip. The red dotted line shows the 50% occupancy point which defines the threshold value. The noise is defined by the distance between the red and the blue dotted lines, which corresponds to one standard deviation of the convoluted Gaussian (see text).

5.3.1 Threshold

The threshold is measured for each pixel by injecting a charge multiple times over the full charge range of the injection circuit and recording the percentage of signals detected (occupancy). The capacitors on the input of the pre-amplifier are charged with a voltage (V_{CAL}) and then discharged in the the pre-amplifier (see figure 5.7 and section 5.3.3). For a perfect discriminator, the number of observed pulses as a function of injected charge should follow a step function, which changes form 0 to 1 at the threshold value. Due to the noise, the response function is a convolution of this step function and a Gaussian distribution, known as an S-curve. Figure 5.8 shows the distribution of a typical threshold measurement for one pixel. The distribution is fitted with a S-curve and the value of the threshold is defined as the one that corresponds to an occupancy of 50%.

In a pixel detector the threshold is crucial for the particle detection efficiency and it is also linked to the spacial resolution. If the value of the threshold is too high, the particles may be not detected hence lowering the efficiency of the detector. When a particle passes between two pixels one can determine its position by calculating the percentage of charge that goes to each pixel. If due to the high threshold, one pixel does not detect any charge, the position of the particle will be affected hence degrading the spacial resolution. On the other hand, for a very low threshold, a high level of noise appears on the readout

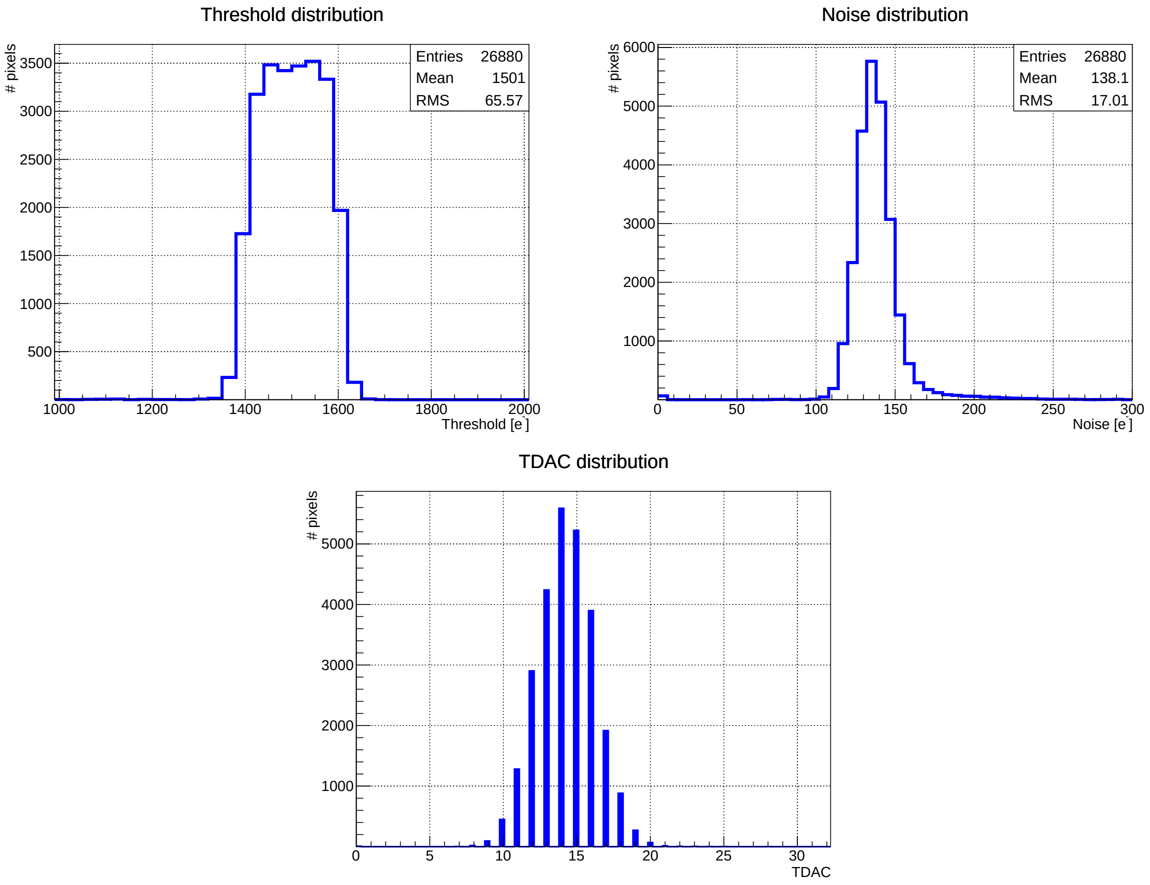

Figure 5.9: Example of a tuning in an FE-I4 before irradiation. Distributions of threshold (top), noise (center) and local TDAC register value (bottom).

electronics, resulting in fake hits.

The aim of a threshold calibration is to achieve the same value of the threshold in every pixel to have a uniform response over the entire module. For the FE-I4 the standard target for the threshold is 1.0 or 1.5 ke$^-$. This is possible by changing the global and local discriminator stages in the chip via two digital registers, GDAC and TDAC, respectively. The GDAC sets a common value of the discriminator over the entire chip. It is 5-bit long in the FE-I3 chip and 16-bit long in the FE-I4 chip. The TDAC allows to fine tune the threshold of every single pixel independently and it is 7-bit long in the FE-I3 chip and 5-bit long in the FE-I4 chip.

Two different algorithms can be used to adjust these registers. First, the algorithm called GDAC_TUNE is used to set the GDAC register. It goes over all the charge range of the injection circuit and calculates the threshold for every pixel, selecting a global GDAC value that gives the threshold closest to the target. The threshold can be fine tuned for every pixel using the local algorithm called TDAC_TUNE which modifies the TDAC register. Similarly to the GDAC_TUNE, this algorithm goes over all the charge range of the

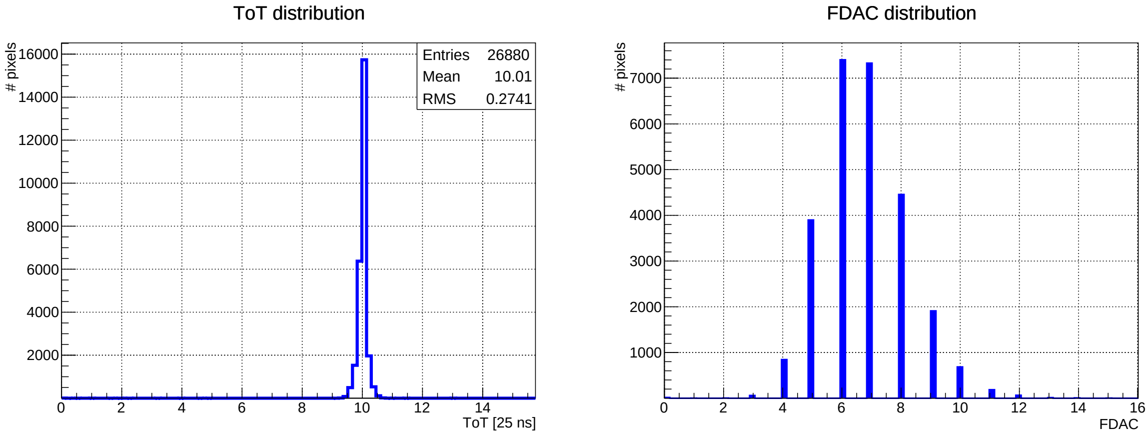

Figure 5.10: Example of a tuning in an FE-I4 before irradiation. Distributions of ToT (top) and local FDAC register value (bottom).

injection circuit to calculate the threshold for every pixel. Then, if the threshold is lower (higher) than the target value, the TDAC register of the pixel is increased (decreased) by a defined step, increasing (decreasing) the threshold. This process is progressively repeated reducing the step size to converge on the best register value to achieve the target threshold.

Since the above procedure for GDAC/TDAC adjustment (GDAC/TDAC tuning) is rather slow (∼30 min), fast versions of these algorithms are implemented (∼5 min) in the calibGUI and in the STControl software (GDAC_FAST_TUNE and TDAC_FAST_TUNE), which inject only the target threshold charge instead going over the full charge range. The measured occupancy for each pixel allows to decide whether the actual threshold was higher or lower than the injected charge and change the register setting accordingly to approach the 50% occupancy. The biggest advantage of this fast algorithm is that reduces considerably the amount of computational time, especially given the high number of channels in the FE-I4 chip. On the other hand it is less robust, in particular for irradiated modules where noisy and inefficient pixels can compromise the assumption made when measuring the occupancy. An example of threshold and noise distributions for a non irradiated FE-I4 module after the described tuning procedure is shown in figure 5.9.

5.3.2 ToT

The Time over Threshold (ToT) corresponds to the number of clock cycles (25 ns) that the signal is above the threshold and is a function of the deposited charge. As for the threshold, the ToT response is calibrated to obtain an uniform behavior over all the module. The ToT is measured by injecting a known reference charge (see section 5.3.3) and measuring the ToT output of the chip. Typical reference charges are 20 ke$^-$, which corresponds approximately to the average charge deposited in a 230 μm thick silicon detector by a minimum ionizing particle. A ToT is then selected to match to this reference charge (our target is usually 10ToT@20ke$^-$, to stay approximately in the center of the ToT dynamic range, which goes from 0 to 15). A similar method used to adjust the threshold values is used to calibrate the ToT values, but in this case the register used for the global tuning is the PrmpVbpf, which is 8-bit both in the FE-I3 and the FE-I4. The ToT pixel tuning is done using the FDAC registers, which are 3-bit long in the FE-I3 chip and 4-bit long in the FE-I4. The PrmpVbpf register controls the global feedback current of the preamplifier by adjusting the signal falling time. The target charge is injected into each pixel (20 ke$^-$) through the injection circuit and a scan over the register range is performed to find the value that gives the closest ToT response to the target (10 ToT). An example of the ToT tuning and the FDAC distribution can be seen in figure 5.10.

5.3.3 Charge calibration injection

In sections 5.3.1 and 5.3.2 the charge injection mechanism is used to adjust the threshold and ToT DACs. As already mentioned, the charge is injected through the charge injection mechanism that is close to the input pad (Q$_{in}$) in figure 5.7 at the bottom left of the image. By using the adjustable voltage V$_{cal}$ and a set of capacitors (C$_{inj1}$ and C$_{inj2}$) a test pulse of charge V$_{cal}\times$C$_{inj}$ can be injected at the preamplifier input. The injection total capacitance has a typical value of ~6.1 fF and the V$_{cal}$ is 1.5 mV/DAC, but both were measured at the wafer for all the FE-I4 chips used in this thesis by different institutions that carried out the wafer probing measurements (Bonn, LBNL...). The injected charge is calculated using the equation:

$$Q_{inj} = C_{inj} \times V_{cal} \tag{5.1}$$

however a ToT to charge calibration is needed in order to correlate the injected charge with the measured charge of a source.

5.3.4 ToT to charge calibration

As mentioned in section 5.3.2, the ToT (which is the output signal of the FE-I3 and FE-I4 chips) can be converted into charge. The conversion can be parametrized with a 2nd degree polinomial function. To do the parametrization a ToT to charge calibration procedure was implemented in STControl and calibGUI: pulses of different charges are injected using the charge injection mechanism covering the full range of possible charges. As the amount of charge injected is known, the ToT is then correlated with the charge injected which allows for a first calibration. The three parameters of the 2nd degree polinomial are calculated (see figure 5.11) and used to convert the ToT measured when using external particles to

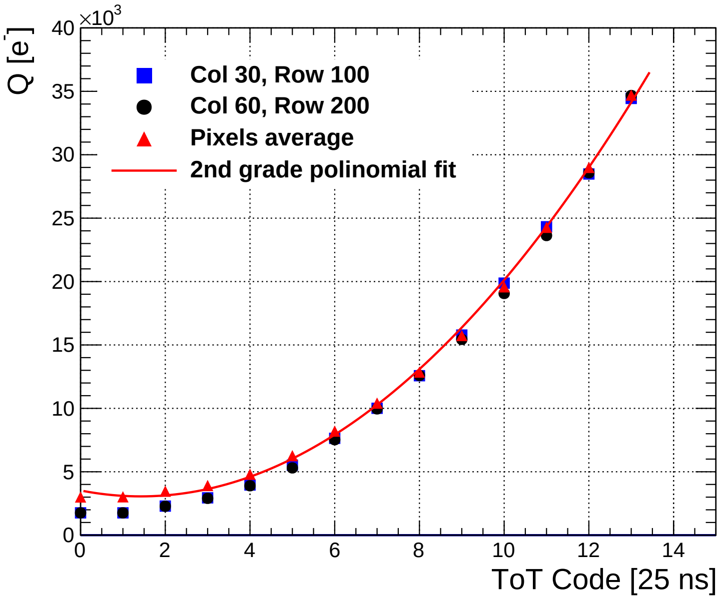

Figure 5.11: Charge injected as a function of the measured ToT for 2 pixels in the center of the FE-I4 chip and the average of all the pixels. The calibration was done for 10ToT response at a charge of 20 ke$^-$. The dependence of the Q with the ToT can be parametrized with a 2nd degree polynomial, but in a small range around the targeted ToT it can be considered lineal.

charge. This calibration is corrected using radioactive gamma sources with a well known spectrum (^{241}Am[3] or ^{109}Cd[4]) by measuring the detector response of such sources. Since the peaks of the photon spectra for the radioactive source and the expected amount of electron-hole pairs generated by that energy are known, it is possible to calibrate the charge collection by comparing the detector response with the expected charge. For the FE-I4 sensors the collected charge measured with an ^{241}Am source was 11.0 ke$^-$ (expected 16.6 ke$^-$) and with the ^{109}Cd source was 4.8 ke$^-$ (expected 6.1 ke$^-$), hence a calibration factor of 1.4 was calculated [49]. For the FE-I3 sensors no calibration factor was needed (see section 6.6.1).

It is important to study the performance of the devices with minimum ionization particles. A ^{90}Sr source is used on the laboratory for this purpose. The ^{90}Sr decays through β disintegration to ^{90}Y and then to ^{90}Zr. The first electron is usually stopped before reaching the detector due to its low energy, but the second has an energy of 2.28 MeV which, on the 230 μm thick Si detector, corresponds to a charge collection of 16.8 ke$^-$. To avoid the loss of collected charge when charge sharing happens, the ToT is added from neighboring hit pixels in a procedure named clustering (see section 5.4.3).

---

[3] E_γ=59.5 keV for the ^{241}Am used for calibration with a signal in Si of 16.6 ke$^-$.

[4] E_γ=22.0 keV for the ^{109}Cd used for calibration with a signal in Si of 6.1 ke$^-$.

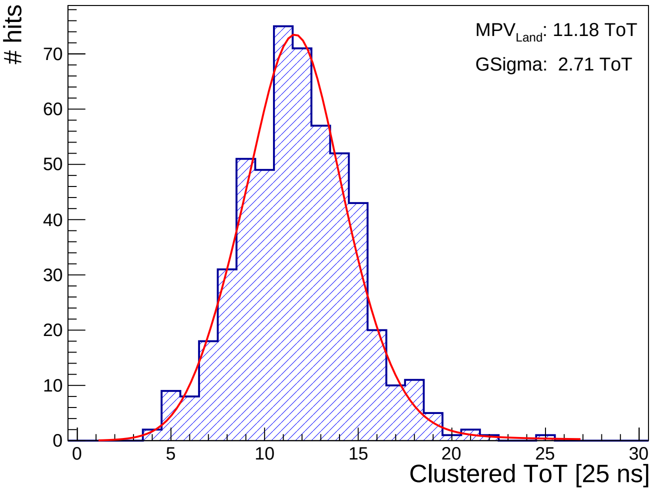

Figure 5.12: Example of a source measurement of the ToT distribution after clustering, performed with a ^{90}Sr on the device W4-E (the collected charge of some devices with the FE-I4 chip is shown in figure 6.10 right). See text and figure 5.13 for the conversion of the ToT into charge.

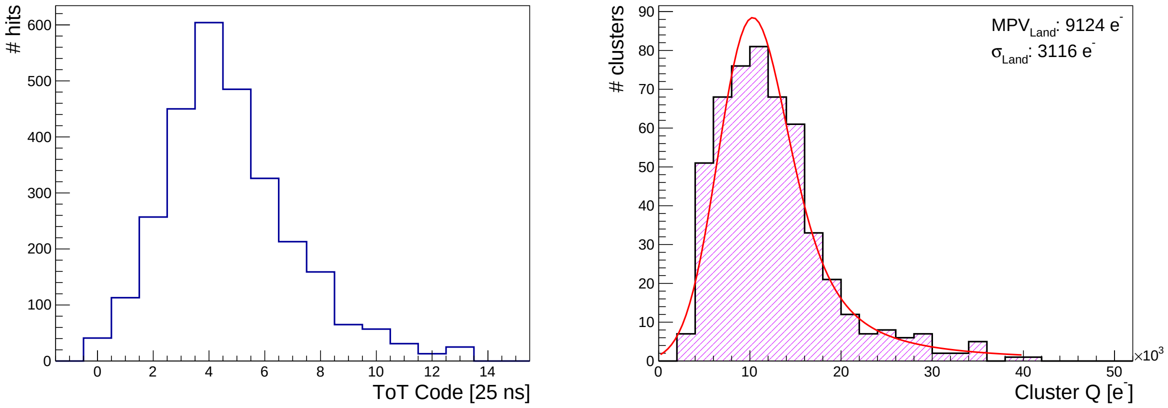

Figure 5.13: (Left) ToT distribution obtained directly from the STControl software (ToT Code). (Right) Charge distribution after the conversion of ToT Code using the 2nd degree polynomial for each pixel (a different polynomial is calculated for each pixel, similar to the figure 5.11).

A typical ToT distribution measured with a ^{90}Sr source is shown in figure 5.12 with calibration parameters of 2ke^{-} as threshold and 10ToT response for a charge of 20 ke^{-}. The value of ToT is extracted by doing a fit of the distribution with a Landau convoluted with a Gauss distribution and taking the Most Probable Value (MPV). As a charged particle source, the Landau distribution describes the energy loss of the hitting particle while the Gaussian distribution accounts for detector fluctuations and noise [33], which widens the distribution. The conversion of the ToT to charge is done using the three parameters of the 2nd degree polynomial fit on the ToT measured directly from the chip (in figure 5.13 left). In the case of figure 5.12 the clustered ToT with a MPV of 11.18 is converted to a charge distribution with a MPV of 9.1 ke^{-} (see the charge distribution in figure 5.13 right). The MPV of the charge is the corrected with the calibration factor of 1.4 calculated previously, resulting on a charge of 12.7 ke^{-}. This value is similar to the expected charge of 16.8 ke^{-} within the uncertainties of 20% (see section 6.5).

5.4 Beam tests

The beam tests are the most crucial part of the characterization of the detectors to be used in high energy physics (HEP) experiments. The aim is to demonstrate the capability of the pixel modules and establish their performance at the conditions required in the experiments. High energy particle beams are provided by dedicated accelerator facilites with well defined characteristics (energy and intensity). To have a reference for tracking purposes, an array of detector devices are arranged as a sequence of layers (so called beam test telescope), which are aligned along the beam line. The beam in combination with particle telescopes, can provide the particle trajectory and allows to determine the impact points on the devices under test (DUT), placed usually on the center of the telescope planes. The information obtained can be used for performance studies like cluster properties, position resolution, hit efficiency, etc. In this section the different beam test facilities and telescope setups are mentioned, and the measurements and analysis methods used are described.

5.4.1 Beam lines

The beam test results presented in this thesis were obtained using the high energy particle beams provided at two accelerator facilities: DESY and CERN. The differences between the two locations do not affect the results obtained in the beam tests in terms of performance, but they play a role in the resolution of the data due to the type of particles and their energies.

DESY

The Deutsches Elektronen-Synchrotron (DESY) is at Hamburg and is one of the accelerators providing beam test facilities. The main electron/positron beam at the DESY II synchrotron generates bremsstrahlung radiation that is converted into electron and positrons by directing the photons to a metal plate. Thanks to this method, the accelerator provides a continuous electron or positron beam. There are beam test lines with up to 1000 particles per cm^2 per second with an energy up to 6 GeV. The spread of the particle momenta in the beam is around 5%. The type of particle wanted is selected with a magnetic dipole which spreads horizontally the particle beam, and is collimated and delivered to the beam lines.

Super Proton Synchrotron (SPS)

The Super Proton Synchrotron (SPS) at CERN is the other facility to perform beam test studies. The SPS has almost 7 km in circumference and is used for several experiments beyond the beam tests. It includes seven beam lines, four of which are dedicated to beam test in the North Area hall. A proton beam is extracted from the SPS accelerator and directed onto two primary targets serving several beam lines. The protons are converted into pions and selected by momenta when passing through a dipole magnet. The energy of the pions used in beam test studies presented in this thesis was of 120 GeV. In this case, the provided beam is delivered in spills which last ∼5 seconds and are delivered every 14-48 seconds depending on the test beam settings. The maximum number of particles per spill is 2×10^8.

5.4.2 Telescopes

To analyze the performance of the sensors one needs a reference telescope to reconstruct the particle trajectories. The most commonly used were the EUDET telescopes, but also a telescope of FE-I4 sensors produced by IFAE[5] was used in particular cases when the EUDET telescope was not available. In both setups there are 6 telescope planes placed 3 upstream and 3 downstream of the DUT, mounted on a movable stage which allows to fine tune the alignment. In this stage a box, which contains the DUT, blocks the external light and also allows to provide the cooling to operate irradiated modules. A chiller sends a cold liquid to a cooling coil inside the box and a fan helps to homogenize the temperature inside. A temperature of -50 °C can be reached. In case the chiller is not available the irradiated modules were cooled using dry ice. A setup mounted in CERN SPS beam line can be observed in figure 5.14.

---

[5] Institut de Física d'Altes Energies, Campus UAB, 08193 Bellaterra, Barcelona, Spain.

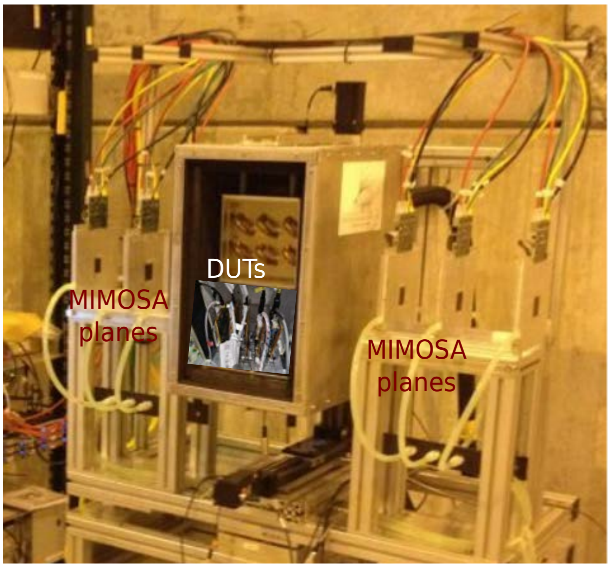

Figure 5.14: Setup of EUDET telescope in SPS beam line.

EUDET

EUDET beam telescopes are based on the MIMOSA [50] detector. The MIMOSA are monolithic active pixel sensors (MAPS) fabricated in the AMS 350 nm OPTO technology. Each MIMOSA sensor is 25 μm thick with 576×1152 pixels of 18.4×18.4 μm^2 size, for a total of 1x2 cm^2 area coverage. The extremely low thickness of the sensors make the telescope specially suitable for tracking of low energy particles, since the resolution is strongly affected by multiple scattering. This is particularly important in the DESY accelerator with its 6 GeV electron beam, but in SPS with the 120 GeV pion beam multiple scattering does not present a problem. The readout is triggered with four scintillators, two at the front and two at the end of the telescope. The maximum achievable pointing resolution is $\sim 2\mu$m and the integration time is 115.2 μs. It is possible to combine the telescope DAQ with USBPix and HSIO-II readout systems including FE-I3 and FE-I4 as DUT. The MIMOSAs have a large integration time compared with the 25 ns of the FE-I4. Due to this, a reference device is needed in addition (usually a FE-I4) to the other DUT to select the in-time tracks. There are several copies of the EUDET telescopes, one installed at DESY and other, property of ATLAS, installed in the SPS.

FE-I4 telescope

A FE-I4 telescope was created by IFAE to be used when the EUDET telescope is not available. It is composed by three FE-I4 planes with 3D sensors at each edge of the telescope making a total of six tracking planes. The pixel cell of the FE-I4 is rectangular, and to maximize the resolution in horizontal and vertical directions, the telescope planes are rotated alternatively in both coordinates. The planes are also inclined by 15° in the direction of the shorter pixel to maximize the efficiency of the 3D sensors (see section 6.7.1) and to improve position resolution. The telescope is read out with the HSIO-II system and can be used to study FE-I4 devices (or other devices compatible with HSIO-II). The trigger is produced by the first and the last planes in the telescope. This allows to fully profit from the area of the telescope in the DUT. Also, thanks to the high clock speed of the FE-I4 this telescope is able to profit from the beam intensity of the SPS beam lines, and also allows to avoid the use of the reference plane for time matching.

5.4.3 Track reconstruction

The EUTelescope framework [51] (EUDAQ software) was used to reconstruct the particle tracks. The track reconstruction is divided in five steps (see figure 5.15): first the trigger information is decoded, and the events are defined (when a hit is recorded in any device within a 25 ns interval). Also, the pixels that show an excessive firing frequency are considered noisy and are suppressed. The second step is the clustering, where the adjacent hits in each event for each detector (MIMOSA planes and DUT) are grouped together defining cluster structures from which the coordinates of the particles crossing the DUT are calculated. In the next step the extrapolated coordinates are transformed into the global reference frame of the telescope according to each plane position and rotation in space. The fourth step is the most crucial for the track reconstruction, and consists in the alignment of the telescope and the DUT planes. This is performed in two phases: first the hits on all the planes are selected and associated to possible tracks. The second phase uses the Millepede-II [52] package to perform an iterative alignment of all planes with a Kalman filter [53] approach. In the last step the hits on the telescope planes are interpolated with a broken-line fit [54] and the crossing coordinates on the DUT are calculated. Using together the coordinate of the track on the DUT and the real hit information different analyses can be performed.

5.4.4 Data analysis

The information of the track calculated in EUTelescope is stored together with the DUT data for further study. The TBMon2 framework [55] was used for the subsequent studies, with some tweaks added for the particular sensors analyzed in this thesis. The data of the DUT are reprocessed to match the requirements of the different specified analysis. The noisy pixels, unresponsive pixels and the ones masked during data taking are identified and excluded (also the nine surrounding pixels are excluded from the analysis). The clusters are formed by grouping together adjacent pixels in space and time. The tracks calculated in EUTelescope are associated to the closest reconstructed cluster (within a

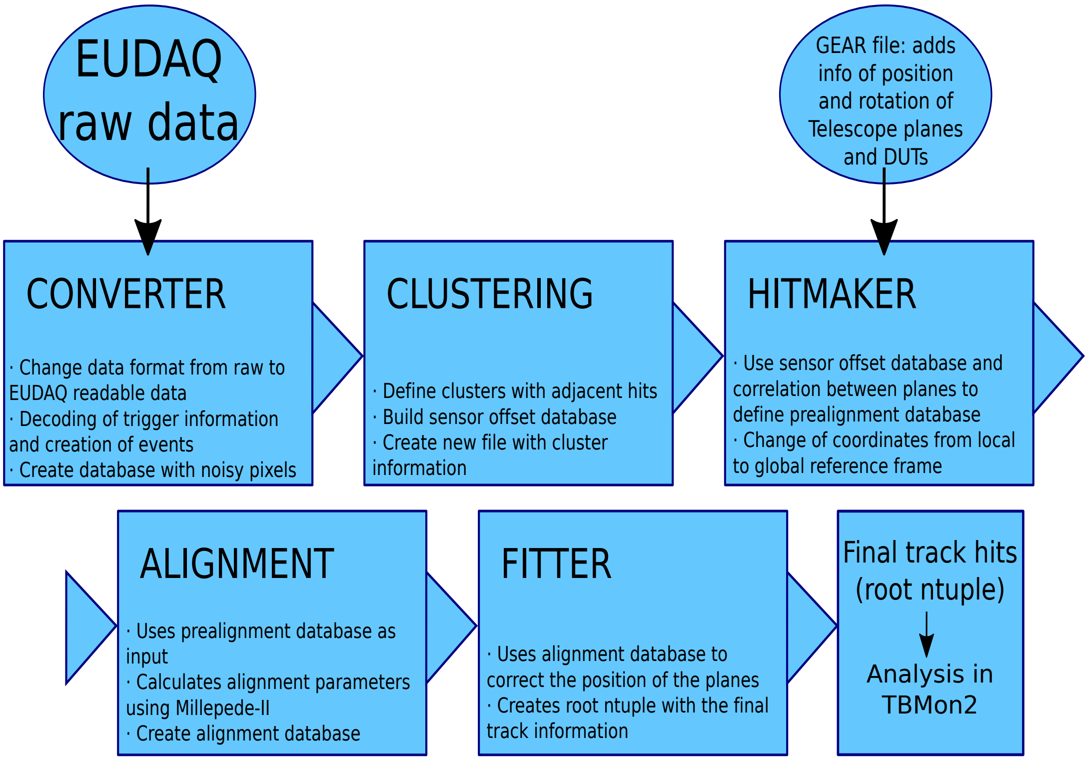

Figure 5.15: Diagram of the steps used in the track reconstruction.

maximum distance of 1.5 times the pixel size in each direction) by looking at their impact points on the DUT.

Cluster properties

A single particle crossing perpendicularly the limit between two or more cells can produce a signal in multiple pixels due to the diffusion of the charge over the silicon bulk, or by non perpendicular particles crossing several pixels. The hits that are adjacent in both space and time are assumed to be produced by the same particle, hence considered a cluster. One can define the cluster size as the number of pixel cells activated in the cluster. The cluster information helps to define the position of a particle hit on the sensor. For single pixel clusters, the geometrical center of the pixel is the best approximation of the particle coordinates. If the cluster size is larger than one, the particle hit can be determined with a better precision by calculating a weighted average of the ToT of each pixel.

Hit efficiency

The hit efficiency of a sensor is calculated as the ratio of the hits associated to a reconstructed track in a cluster measured on the DUT to the total number of tracks reconstructed by the telescope crossing the active area of the DUT. The track reconstructed by the telescope is interpolated on the DUT, and the clustered hits of the DUT are associated to this track if they are inside a matching window (usually two times the size of the FE-I4 pixel, 500 μm on x direction and 100 μm on y direction). The efficiency is usually defined over a big area in a sensor, but thanks to the pointing resolution of the telescope it is possible to determine the hit efficiency in a small area of the sensor. In particular, it is important to focus in single pixel cells to see the effect of the columns in the 3D sensors or study the borders of the sensors. For these high resolution measurements it is necessary to collect high statistics, so the information is projected from all the structures onto a single one. For the hit efficiency value an absolute systematic uncertainty of 0.3% is associated to all the measurements [56]. This systematic uncertainty is dominating over the statistic uncertainty due to the high statistics that are usually collected at beam tests. In general the uncertainties are calculated as the sum in quadrature of the systematic and the statistical uncertainty obtained [57].

Spatial resolution

The spacial resolution of a pixel detector can be extracted from the residual distribution. The residuals come from the difference between the position hit in the DUT and the reconstructed impact point of the closest track associated to it. Due to the special shape of the pixel cells (see section 6.2) the residuals are calculated independently in both directions of the pixels. Since the particle flux is uniform, the residual distributions for single pixel clusters are expected to be box shaped with smearing at the edges of the pixels due to the resolution of the telescope. If the cluster size is larger than one, the resolution improves with the charge information and the expected residual distributions have a Gaussian shape.

5.5 Irradiation facilities

The irradiation facilities where used to duplicate the conditions of the sensors after different time periods under the conditions of the HL-LHC. Before describing the facilities, three concepts need to be explained: fluence, hardness factor and Total Ionizing Dose (TID). The particle fluence is the number of incident particles on the surface of a material divided by the area of the surface and is measured in particles per cm^2. Since the devices were irradiated with different particles and energies, the damage is expressed in terms of Non-Ionizing Energy Loss (NIEL). To have the same NIEL units, the fluence is scaled to the equivalent fluence of reference particles, in general to 1 MeV neutrons (neutron equivalent) per cm^2 (noted as n$_{eq}$/cm^2). The conversion factor between any particle to neutron equivalent is called hardness factor and is extracted from the dependence of the leakage current with the radiation damage (see section 4.4). On the other hand, the TID reflects the radiation damage effect of charged particles and affects mostly electronic devices that are sensitive to small charge deposits (like transistor and insulator layers). The TID varies between the different facilities. The facilities used for the irradiation of the sensors have the following characteristics:

TRIGA Mark II reactor (Ljubljana)

The TRIGA Mark II research reactor at the Jožef Stefan Institute (JSI) in Ljubljana is a light water pool type reactor, cooled by natural convection. It is used as a source of neutrons and γ rays for irradiation of silicon modules and related radiation damage studies. To reach the reactor core, the facility offers four channels (empty fuel roads), with a diameter of 15.5 cm, where the silicon detectors can be irradiated at different temperatures. Since the components of the FE-I4 chip are activated when irradiated by neutrons [58] this facility was used only for irradiation of sensors with FE-I3 chip and strip detectors. These irradiations were useful to compare the power dissipation between the neutrons and protons and the different types of sensors. The highest achievable neutron flux is in the central channel, where it can reach almost 2×10^{13} cm^{-2}s^{-1} at the reactor full power of 250 kW. The most significant radiation damage for silicon detector comes from fast neutrons with energy $\geq$ 100 keV which have a flux of up to 5×10^{12} cm^{-2}s^{-1} with a TID per fluence of about 10 kGy[6] per 10^{15} n$_{eq}$/cm^2 at 250 kW and a hardness factor of 0.9. The contribution of thermal neutron and gamma irradiation is not significant since their damage in silicon is negligible compared to that of fast neutrons.

Compact Cyclotron (KIT)

The Zyklotron AG provides a 23 MeV proton beam from the cyclotron installed at the Karlsruher Institut für Technologie (KIT). The protons have a hardness factor of 2.0 with a TID per fluence of 1.5 MGy per 10^{15} n$_{eq}$/cm^2 and a typical flux of about 9×10^{12}cm^{-2}s^{-1}. The samples are hosted in a cooling box where the temperature is monitored to avoid annealing during the irradiation. A moving table allows to scan the beam across the detector surface to achieve a uniform irradiation of the samples over an area larger than the 7 mm beam spot size. The full modules can be irradiated directly while mounted on PCBs. The PCB components can be protected with a 2 cm thick screen made of high purity aluminum. This avoids repeating the wire bonding of the chips to the cards and possible damages during the handling. Because of the low energy of the protons (hence larger TID) the maximum achievable fluences at the KIT facility are limited by

---

[6] 1 Gy = 100 rad = 1 J/kg.

the damage induced in the readout chips by the ionising radiation. The FE-I4 modules at KIT were irradiated to a maximum fluence of 1×10^{16} n_{eq}/cm^2.

IRRAD Proton Facility (PS)

The IRRAD Proton Facility provides a proton beam from the Proton Synchrotron accelerator installed at CERN with an energy of 23 GeV. The beam spot size is usually 12 mm resulting in a non uniform irradiation over the surface of the sensor. This allows to explore different fluences on the same sensor at the expense of not being able to study power dissipation. In some cases the beam spot used was 6 mm due to the necessity on other experiments. The protons have a hardness factor of 0.60 with a TID per fluence of 0.4 MGy per 10^{15} n_{eq}/cm^2 and a typical flux about 3×10^{10} $cm^{-2}s^{-1}$. The modules are mounted on a table and several of them can be irradiated together directly mounted on the PCB. The beam profile is measured with an aluminum foil placed close to the sensor. The foil size is 2×2 cm^2 and is divided in pieces to have a more precise measurement of the irradiation profile of the sensor. Thanks to the higher energy of the protons which allows to achieve higher fluences with lower TID, the maximum fluence achieved in a working FE-I4 sensor was 3.1×10^{16} n_{eq}/cm^2.

Chapter 6

3D sensors for the ITk pixel detector

The main purpose of this chapter is to demonstrate that 3D sensors are a suitable option for the innermost layer or layers of the ATLAS pixel detector for the HL-LHC due to their excellent performance after high levels of irradiation. The objective is to demonstrate that the small sized pixel (50×50 μm^2 or 25×100 μm^2) 3D sensors have better radiation hardness that sensors used in the previous experiments (Run 1 pixel detector (50×400 μm^2) and IBL (50×250 μm^2)). The first production of 3D sensors with small pixel size (referred to them as small pitch devices) was finished in December of 2015, but the chip that will be used in the ITk pixel detector (the RD53 ASIC) was still under development[1]. Due to this, the small pitch sensors were adapted and tested in the existing FE-I4 chip.

A total of nine small pitch sensors bump-bonded to FE-I4 chips were successfully tested before and after irradiation, showing that they fulfill the requirements of the innermost layer of ITk. These requirements include a minimum efficiency of 97% after the maximum irradiation of 1.4×10^{16} n$_{eq}$/cm^2 (considering one replacement and a safety factor of 1.5) and a very low power dissipation (limited by a maximum current of 10 nA per pixel). The efficiency was measured on beam tests for devices with a pixel size of 50×50 μm^2 irradiated uniformly at KIT up to 10^{16} n$_{eq}$/cm^2 and non uniformly up to 2.8×10^{16} n$_{eq}$/cm^2 achieving the minimum 97% efficiency with sufficient voltage. The low voltage required by 3D sensors to achieve the 97% efficiency results in low power consumption. The power dissipation was measured for the 10^{16} n$_{eq}$/cm^2 fluence point, giving a value of 8 mW/cm^2 (at 100 V to reach the 97% efficiency). Compared to other competing technologies, like thin planar sensors (500 V for 97% efficiency, and 25 mW/cm^2), the power dissipated by 3D sensors is significantly lower.

This chapter is organized as follows: first, in section 6.1 the radiation hardness limit of the IBL technology is explored. In section 6.2 the geometry of the small pixel size sensors is explained. In the sections 6.3 and 6.4, the fabrication of 3D sensors, the adaptation to the FE-I4 chip and the assembly process are described. The results of the chip calibration

---

[1] The first prototype of the ITk pixel chip, the RD53A, was available in 2018.

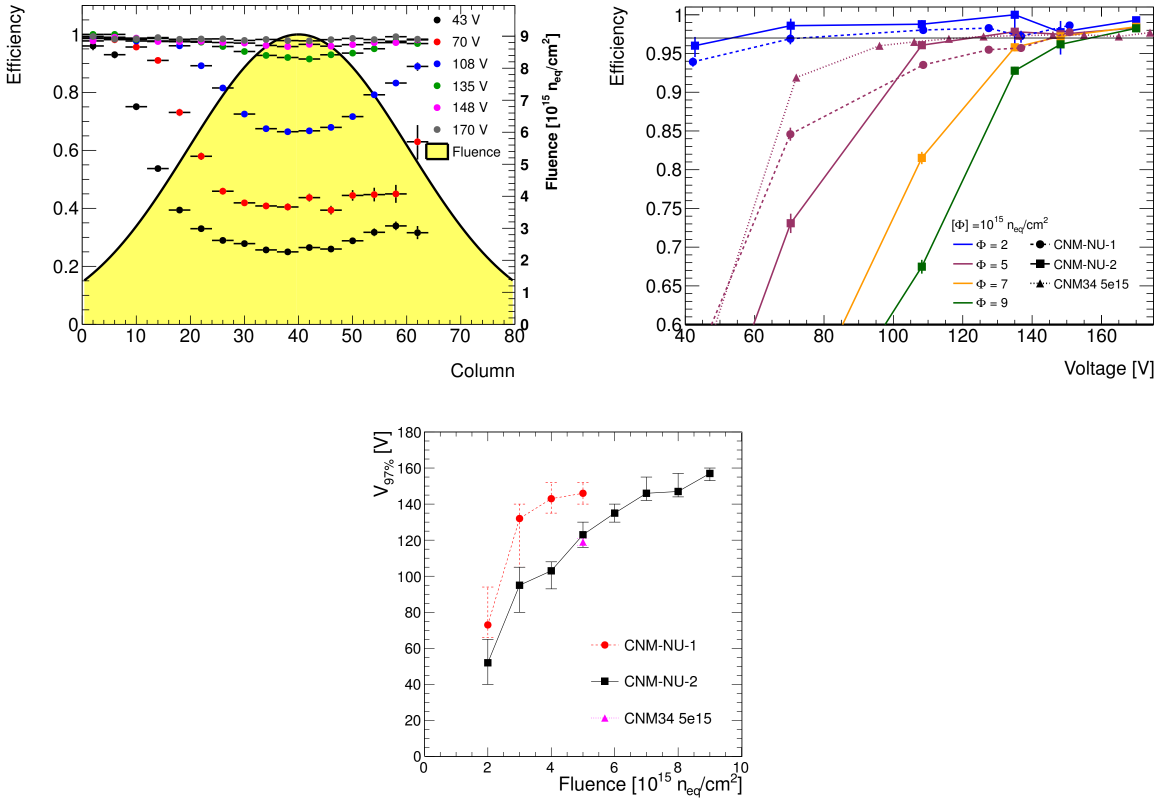

Figure 6.1: Top left: Hit efficiency as a function of pixel column number for different voltages for CNM-NU-2. The corresponding fluence distribution is also shown. Top right: Hit efficiency versus voltage for different fluences for all devices. The 97% benchmark efficiency is marked. Bottom: Voltage needed to reach 97% efficiency as a function of fluence.

and the measurements of the charge collected by the devices are covered in section 6.5. Measurements on standard FE-I3 sensors, small pitch strips and small pitch pixel sensors on FE-I4 irradiated to HL-LHC fluences are shown on section 6.6. Finally, the results of the beam test measurements are presented in section 6.7.

6.1 Limits of the IBL 3D sensors

As mentioned before, the IBL generation devices have a pixel size of 50×250 μm^2 and are coupled to the FE-I4 chip. The FE-I4 chip was specified to withstand an ionizing dose of 250 Mrad and a fluence of 5×10^{15} n_{eq}/cm^2. However, before the first small pitch devices were ready to be tested, the limits of the 3D IBL generation devices in terms of radiation hardness were tested. To do so, two devices were irradiated with a non uniform beam (12 mm beam size) to a maximum fluence on the peak of 5.6×10^{15} (CNM-NU-1) and 9.1×10^{15} n_{eq}/cm^2 (CNM-NU-2). The fluence ranged from a 15% at the device edge to a 100% in the center of the device. They were compared to a FE-I4 device irradiated uniformly to a fluence of 5×10^{15} n_{eq}/cm^2 (CNM34). The TID for these irradiations (shown in table 6.3) already exceeds the specifications of the FE-I4. The threshold is set to 1500 e^-.

The fluence distribution for the device with highest irradiation is shown in figure 6.1 top left. The hit efficiency, overlaid to the fluence, is shown at different voltages. A minimum in efficiency can be observed at the maximum fluence on the center of the device, as expected. For a fixed fluence, the dependence of the efficiency with the voltage can be extracted (see figure 6.1 top right). The hit efficiency of the two non uniformly irradiated devices agree reasonably well, and at 5×10^{15} n_{eq}/cm^2 they also agree with the uniformly irradiated device.

The voltage needed to reach the benchmark of 97% efficiency (named $V_{97\%}$) is shown in figure 6.1 bottom. For the IBL target fluence of 5×10^{15} n_{eq}/cm^2, the $V_{97\%}$ obtained for these devices ranged from 120 to 145 V[2] (linearly interpolated between measurement points). For the highest fluence measured of 9×10^{15} n_{eq}/cm^2, the $V_{97\%}$ is about 155 V. A lower $V_{97\%}$ is needed for small pitch devices as it will be demonstrated in section 6.7.

6.2 Small pitch sensors for the HL-LHC

During Run 1, the pixel detector of ATLAS had three cylindrical layers of pixel sensors which use the FE-I3 chip. During the first long shutdown (LS1), in 2014, a new layer of pixel sensors was introduced closer to the beam pipe (called Insertable B-Layer (IBL)) which improves the capabilities of the ATLAS detector (see section 3.2.1). The sensors used in the innermost layer during Run 2 and Run 3 are coupled to the FE-I4 chip. The 3D sensors have a pixel cell of 50×250 μm^2 with two n^+ column-like electrodes connected together surrounded by six p^+ ohmic implants. The two n^+ readout columns are connected together and also to the readout ASIC through a solder bump pad. This is referred to as 50×250 2E configuration, with a distance between electrodes (inter-electrode distance or L_{el}) of 67 μm. For the HL-LHC upgrade, the pixel sizes proposed are of 50×50 μm^2 with one 3D n^+ electrode per pixel surrounded by four p^+ ohmic implants (50×50 1E) and 25×100 μm^2 either with two n^+ electrodes per pixel surrounded by 6 p^+ ohmic implants (25×100 2E) or with one electrode per pixel surrounded by 4 p^+ ohmic implants (25×100 1E). The geometry of the IBL pixel sensors and the small pixel size sensors is shown in figure 6.2. The 50×50 1E sensor has a L_{el} of 35 μm, for the 25×100 2E the L_{el} is 27 μm and the 25×100 1E has a L_{el} of 52 μm. These three sensor options for the HL-LHC would operate with the new RD53 chip which has a pixel cell of 50×50 μm^2.

The 50×50 μm^2 geometry keeps the same resolution than IBL in the r-φ direction while increasing the resolution in the z direction. It is the easiest 3D sensor configuration

---

[2] The $V_{97\%}$ of 120 V from the uniformly irradiated device is taken for future comparison.

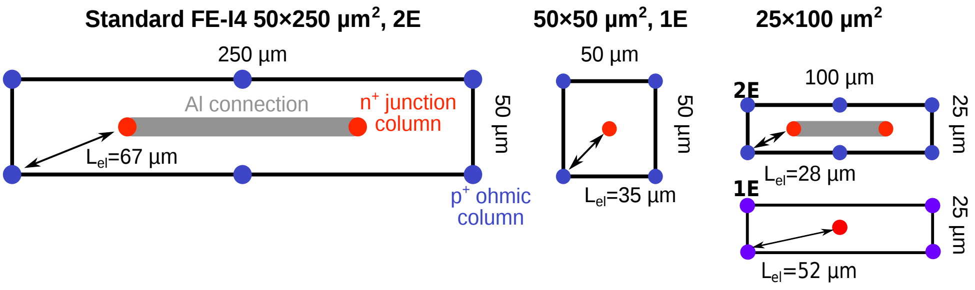

Figure 6.2: Geometry of a 3D pixel cell for a standard IBL FE-I4 pixel with 50×250 μm^2 2E configuration (left), a pixel of 50×50 μm^2 1E (center) and a pixel of 25×100 μm^2 (right) 2E (top) and 1E (bottom).

to fabricate and has the same pixel size than the future RD53 ASIC[3]. The 25×100 μm^2 1E improves the r-φ resolution (which yields a better b-tagging efficiency) at the expense of increasing the inter-electrode distance. The higher L$_{el}$ means lower radiation hardness and it was expected that it could not fulfill the ITk requirements. To improve the radiation hardness of the 25×100 μm^2 1E, the 25×100 μm^2 2E pixel size was proposed. It keeps the better position resolution in the r-φ direction but also reduces the inter-electrode distance compared to the 50×50 μm^2 1E pixel, increasing the radiation hardness. However this pixel geometry is very difficult to produce with a single sided fabrication process (see next section) due to the lack of space to place the bump bond pads (see on figure 6.3 bottom right that the distance between the bump pad and the p$^+$ column is very small (a short circuit can be caused if the bump pad touches the p$^+$ column)).

Another important factor that determines the sensor performance is its thickness. The IBL 3D sensors were 230 μm thick, but for ITk the target is to reduce the active thickness to 150 μm (to reduce occupancy) while maintaining a total thickness of 250 μm to provide a better bump-bonding yield (thin sensors are more sensitive to deformation in the flip-chip cycle that may cause unconnected bumps). In this thesis the small pitch sensors studied have a thickness of 230 μm.

6.3 Fabrication of the small pitch sensors

As mentioned before, the first production of 3D detectors with small pixel size was fabricated at CNM[4] and finished in December 2015 (run number 7781). The wafers were similar to the ones used in the IBL production: p-type wafers with 230 μm active thickness and 20 kΩcm resistivity (instead of the 150 μm active thickness that is expected to be used for the HL-LHC (with 250 μm total thickness)). They were prepared to be

---

[3] The final version of RD53 ASIC is expected to be fabricated in 2020.

[4] Centro Nacional de Microelectrónica, Campus UAB, 08193 Bellaterra, Barcelona, Spain.

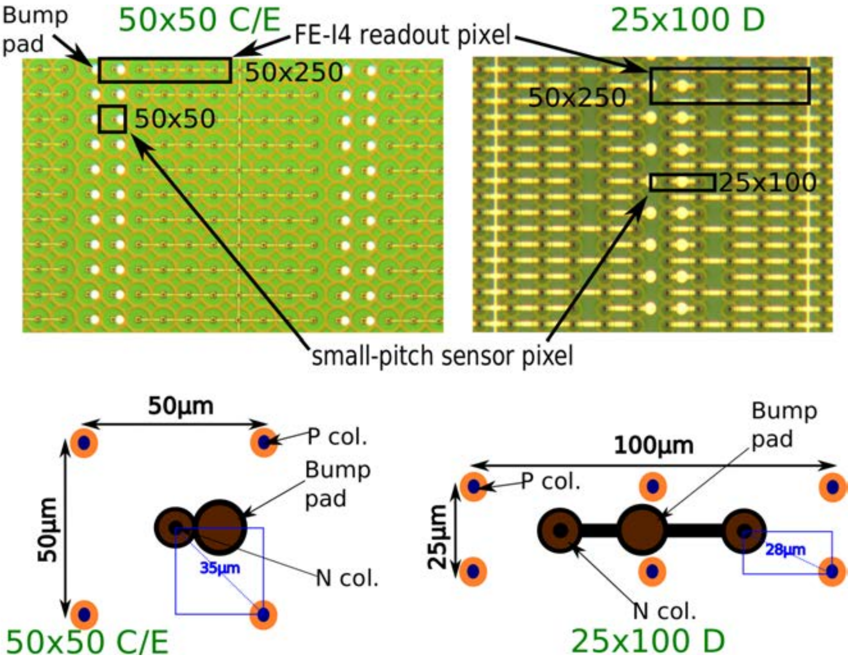

Figure 6.3: Top: microscope picture of a 50×50 μm^2 (left) and 25×100 μm^2 (right) sensors with the pixel size of the FE-I4 and the small pitch pixels (black rectangles). Bottom: Schematics of the 50×50 μm^2 1E and 25×100 μm^2 2E pixels.

coupled to the ATLAS FE-I4 chip. Using a double side process, the 3D p$^+$ ohmic columns were etched and doped from the back side and the n$^+$ junction columns from the front side. These columns are non-fully passing through, stopping at about 30 μm of the other surface (which avoids the risks of short circuit, hence the fabrication of 25×100 μm^2 2E configuration with a double sided process is safe). This helps to avoid that one particle crossing the detector in perpendicular incidence is undetected if it goes through the column (see figure 6.17). The nominal value of the column diameter is 8 μm, which ranges from 10 μm on the surface to 5 μm close to the column tip. Compared to the 3D CNM IBL production, a diameter reduction of 2 μm was achieved in average (figure 6.4 right). This reduction of the column diameter is also desirable to reduce the particle detection inefficiency associated to them.

The double side process was chosen by its simplicity compared to the single sided (which consist on etching and doping both type of columns from one side) because the difficulty of doping the two different kinds of holes from the same side is avoided. A sketch of a double sided fabrication process of 3D sensors is shown in figure 4.12. The silicon on the back surface does not need any patterning since it shorts all the holes together. Another advantage of having one kind of holes etched from the back side is that in this way it is possible to apply the high voltage bias to the back surface of the detector by simple wire bonding (a negative voltage is applied on the back side while the front side is

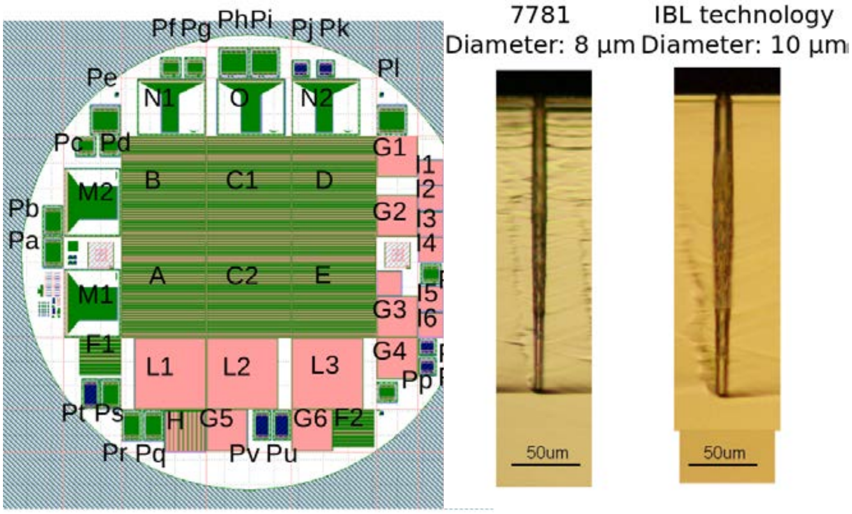

Figure 6.4: Mask layout of the wafers of the run 7781. The FE-I4 small pitch sensors are the C, E (both 50×50 1E) and D (25×100 2E). The device A is a standard IBL-like 50×250 μm^2 2E and B is a small pitch device with a pixel size of 25×100 μm^2. There is also one small pitch FE-I3, named as F2 (50×50). On the right, a microscopic lateral view of a column of the small pitch production compared to the IBL.

connected to ground via the wirebonds). This avoids complicated rerouting in detectors for readout electronics such as for the FE-I4, which do not have any structure to apply the bias from the bump bonded side. The limit of the double side process comes from the thickness of the sensors (very thin sensors may break while handling during the etching). The chosen active thickness for the ITk 3D sensors of 150 μm is probably very thin to achieve a good production yield with the double sided process. Due to this, the ITk sensors (of 150 μm active thickness) will be done with a single side process. As mentioned before, the 150 μm active thickness is chosen to reduce occupancy in the ITk high dense medium.

A mask layout has been designed for the fabrication of the first prototypes of 3D sensors with the ITk pixel geometries but compatible with the FE-I4 ASIC. The mask also included test structures, pad diodes, microstrip detectors, ITk pixel geometries compatible with the FE-I3 ASIC and other pixel detectors for other experiments (as shown in figure 6.4). Though this thesis studies pixel detectors, strip detectors with similar geometries (strips can be seem as pixels connected together) can be useful to understand some properties of pixel sensors. The strips were tested by measuring their electrical characteristics after irradiation and compared with standard 3D FE-I3 (50×400 μm^2) pixel sensors irradiated to HL-LHC fluences (to see the effect of the L_{el} on the leakage current (see section 6.6)). The strip detectors can also be wire-bonded to analog readout electronics to be tested to study charge collection on a special setup (measurements of

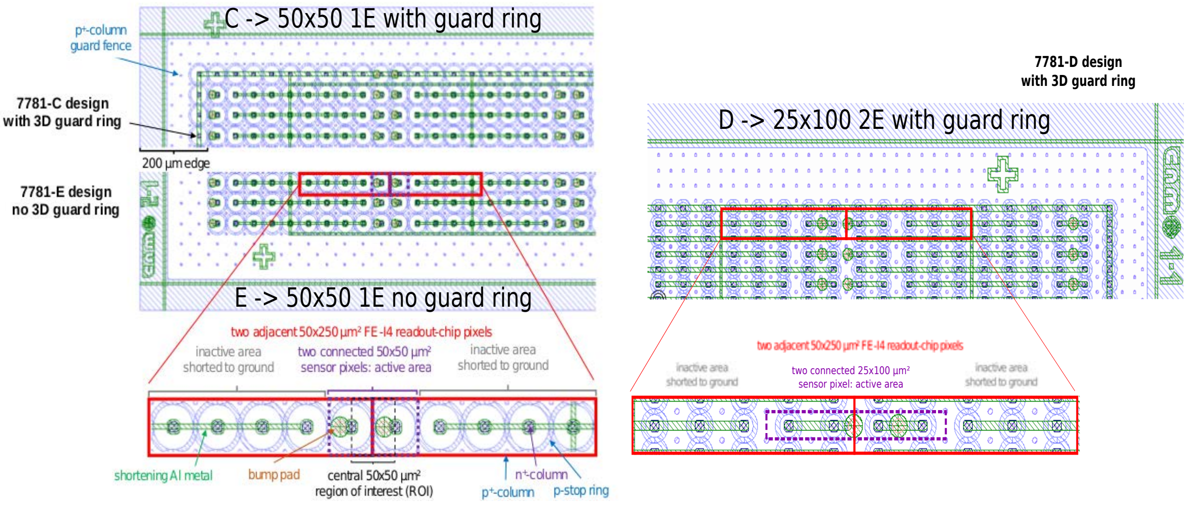

Figure 6.5: Top: layout of small pitch 3D pixel prototype sensors of run 7781 matched to the FE-I4 readout chip in two different edge designs: with (“C” and “D”) and without (“E”) 3D guard ring. Bottom: layout of the 50×50 1E (left) and 25×100 2E (right) geometries inside the FE-I4 pixel. The 25×100 1E configuration was not produced in this run.

charge collection efficiency on TCT [59]).

To adapt the 50×50 1E sensors to the FE-I4 chip a group of five horizontal pixels was considered, thus having a 50×250 μm^2 structure like the FE-I4 pixel size. A sensor pixel in the edge is connected (through the n$^+$ junction column) to the readout bump of the FE-I4 while the other four are not connected to the readout, but shorted together to ground (figure 6.3 and 6.5 left). This allows to have the pixels at the same potential than the ones being read out (“C” and “E” devices).

The sensors with 25×100 μm^2 pixel size included in this run had two n$^+$ electrodes per pixel (25×100 2E devices named as “D”). Considering a FE-I4 chip pixel of 50×250 μm^2, the sensor pixel of 25×100 μm^2 is contained inside of the FE-I4 pixel. The two n$^+$ columns of the sensor pixel are connected together to one of the FE-I4 bump pad. Since the pitch of the sensor is 25 μm in y axis and for the chip is 50 μm, there is a gap in this direction of 25 μm between the consecutive pixels that are read out. The sensor pixels that are not connected to the readout are connected to ground at the same potential (see figure 6.3 and 6.5 right).

The edge termination was performed with a 3D guard ring of shortened n$^+$ type columns around the active area connected to ground, in combination with a 3D guard fence of p$^+$ columns which are connected to the high voltage (“C” and “D” devices). Alternatively, some sensors were fabricated without the 3D guard ring and only with a 3D guard fence (“E”), allowing the collection of charge beyond the physical boundaries of the last pixel [60]. For all the pixel sensors the distance between the border of the last pixel and the diced edge is 200 μm (figure 6.5 top). The small pitch sensors cover the full area of the FE-I4 chip (80×336 pixels).

The mask of the small pitch runs (see figure 6.4) included three 50×50 1E (two C and one E) and one 25×100 2E (D) sensors per wafer that were tested in the laboratory and beam tests. Some strip detectors are also present in the wafer (named as M with 50×50 μm^2 pixel size and N with 25×100 μm^2 pixels) and were irradiated and used to measure the leakage current and power dissipation (see a list of the tested devices in table 6.1).

It should be noted that this first production of small pitch 3D devices compatible with the FE-I4 chips suffered from very low yield. Several wafers broke during or immediately after production (due to damage induced in the wafer edges while processing), and the leakage current performance of the final sensors was not optimal (see section 6.5) due to defects in the column sidewall appearing during the DRIE. The 3D sensor production yield increased significantly after the problems were addressed [61] using a protection on the edges of the wafer while the process parameters of the DRIE were optimized to reduce damage to the column sidewall. Due to these problems of the first production, only 9 small pitch FE-I4 pixel sensors were produced (out of 5 wafers) with good electrical properties to be used, all belonging to this first production (run number 7781). Part of the problem explaining the low yield are related to under bump metallization, as explained below.

In order to connect electrically the sensor pixel pad to the readout pad of the ASIC with a solder bump, an additional metal layer has to be deposited on the sensor aluminum bump pad. Such process is called under bump metallization (UBM) [62]. Two types of UBM were be performed at CNM: electro-plate and electro-less. The electro-less UBM was done with a chemical bath of Ni-Au but is not meant for small bump pads (typical diameter of bump pad between 10 and 20 μm). The advantage is that it can be performed on single (diced) sensors and is cheap compared with electro-plating. The electro-plating UBM, on the contrary, was done on the full wafer depositing a W-Ti alloy, Cu and Au. It potentially does a more precise deposition of metal on the bump pads[5], but it is more costly than the electro-less UBM. Two batches of pixel sensors were fabricated with electro-less UBM and one of electro-plate UBM. The first electro-less batch failed to deposit gold on a large fraction of bumps. For the second batch, the parameters of the UBM were adjusted and the quality of the deposition was greatly improved. Since the electro-plate method is being developed at CNM, it resulted in medium quality metal deposition. In total nine of the sensors with UBM were successfully processed for R&D purposes (see table 6.2 for the list of sensors and the UBM applied). Afterwards, the wafers were diced at CNM and sent to IFAE, where the hybridization (connection between sensor and readout electronics) is performed.

---

[5] This process is still under development at CNM.

Device name	Device type	Guard ring	Geometry	Measurements	Irradiations (Fluence[n_{eq}/cm^2])
W4-C1	Pixel	3D+fence	50×50 1E	Leakage current Charge collection Beam tests	Non uniform @ PS
W4-D	Pixel	3D+fence	25×100 2E	Leakage current Charge collection Beam tests	Non uniform @ PS
W8-C1	Pixel	3D+fence	50×50 1E	Leakage current Charge collection	Not irradiated
W8-C2	Pixel	3D+fence	50×50 1E	Leakage current	Not irradiated
W8-E	Pixel	Fence only	50×50 1E	Leakage current	Not irradiated
W3-E	Pixel	Fence only	50×50 1E	Leakage current Charge collection Beam tests	Not irradiated
W5-C2	Pixel	3D+fence	50×50 1E	Leakage current Charge collection Beam tests	Uniform @ KIT
W3-C1	Pixel	3D+fence	50×50 1E	Leakage current Charge collection Beam tests	Uniform @ KIT + Non uniform @ PS
W4-E	Pixel	Fence only	50×50 1E	Leakage current Charge collection Beam tests	Uniform @ KIT
W4-M1	Strip	No	50×50 1E	Leakage current	Uniform @ TRIGA (5×10^{15})
W4-M2	Strip	No	50×50 1E	Leakage current	Uniform @ TRIGA (1×10^{16})
W4-N1	Strip	No	25×100 1E	Leakage current	Uniform @ TRIGA (5×10^{15})
W4-N2	Strip	No	25×100 1E	Leakage current	Uniform @ TRIGA (1×10^{16})

Table 6.1: Devices of the run 7781 with characteristics and measurements done listed. The leakage current and beam test measurements were done before and after irradiation. The charge collection was done only on non irradiated devices. The detailed irradiations of the FE-I4 devices are listed on table 6.3.

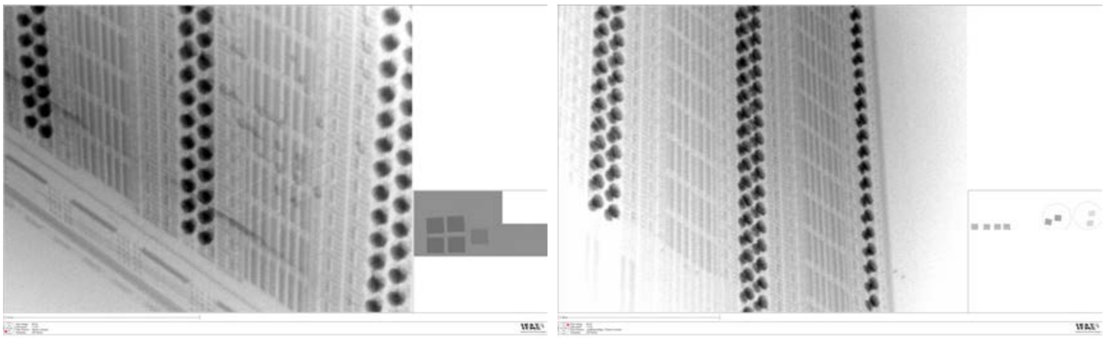

Figure 6.6: X-ray image of two small pitch pixel sensors in an area of correctly connected bumps (left) and an area of disconnected bumps (right). Note that the correctly connected bumps have a spherical shape while the disconnected bumps have a hourglass shape.

6.4 Assembly of small pitch modules on FE-I4 chip

After dicing, the sensors are flip chipped to the front-end chip, and then glued and wire bonded to a dedicated readout board at IFAE. The flip chip is done with a Süss Microtech FC-150 bonder machine with a reflow arm. The sensors and the chips are aligned on the machine, heated to 260 °C for a short period and pressed together. After flip chip, the bare assembled sensors are processed in a fluxless formic acid reflow oven which helps to strengthen the connection between the chip and the sensor.

For a good quality hybridization a good UBM and a good flip-chip process is needed. The flip-chip worked for two sensors of the first samples with electro-less UBM, but they have a large number of disconnected pixels ($\sim$80%) due to the bad UBM. Three sensors with electro-plate UBM also have several disconnected pixels ($\sim$40-50%) and even one detached during handling. Four sensors of the third electro-less UBM show excellent hybridization with almost no disconnected pixels (only one device (W3-E) has some disconnected pixels in a corner). A verification of the connected pixels with a ^{90}Sr source is shown in table 6.2.

To check the quality of the bare assembled sensors before mounting on the readout board an x-ray machine was used. The images taken with the x-ray machine show a spherical form on the bumps if a good connection was achieved (as can be seen in figure 6.6 left), but other forms (specially hourglass shape) on the bumps can be seen when the connection failed (figure 6.6 right). The failures on the bump bonding appear mostly in the edges of the devices probably due to thermal deformation during the bonding cycle.

The dependence of the current (leakage current) with the high voltage applied (the I-V curve) is measured on the bare module using a probe station. Two needles are used to apply the voltage, one in contact with the back side of the sensor (which provides the negative HV) and one connected to the front side through a pad (pad number 132) on

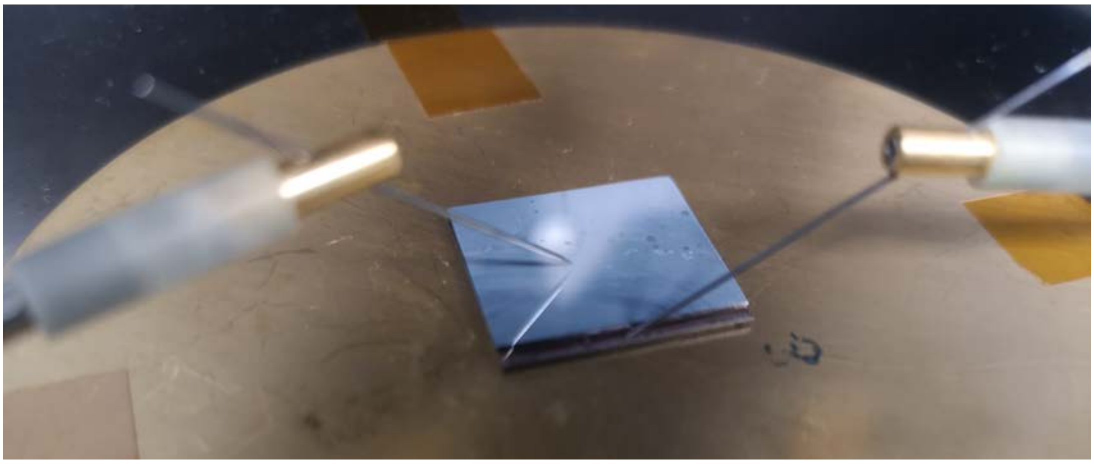

Figure 6.7: Picture of the probe station needles connected to a small pitch sensor to do the IV curve before mounting on the readout board.

the FE-I4 (connected to ground), as shown in figure 6.7. The leakage current measured using this method and the measured using the readout board (section 6.5) are expected to be similar (see figure 6.8), specially below the breakdown voltage, where the devices are operated (only the devices from the wafers 4 and 8 were measured on the probe station, hence not all the 9 devices are represented in this figure).

The devices are then glued to the readout boards and the pads of the FE-I4 chip are wirebonded to the readout board circuit. The gluing is performed with 50 μm thick doubled sided TESA tape and/or ARALDITE 2011. The back side of the sensor is connected to a LEMO connector to be able to apply the high voltage. The chip can be powered via a molex connector with 8 pins and read out via an ethernet interface or powered and read out together from a flat ribbon cable (see figure 5.3 right). Quality assurance measurements are done after the device is mounted on the PCB: the chips are calibrated as shown in section 5.3 and a charge collection verification is performed with a ^{90}Sr source (table 6.2).

6.5 Laboratory characterization of the devices

Once the devices are mounted on the readout boards they are thoroughly tested. The most simple and fundamental test of the device is the leakage current measurement. The I-V is measured to determine the overall quality of the sensor (determined by the breakdown voltage V_{bd} and the current values) and to determine the range of usable voltages to work in order to avoid damaging the sensor. To measure it, a voltage supply applies a negative voltage through the LEMO connector of the readout board. As mentioned before, all the sensor pixels are at the same potential, hence the measured current corresponds also to the

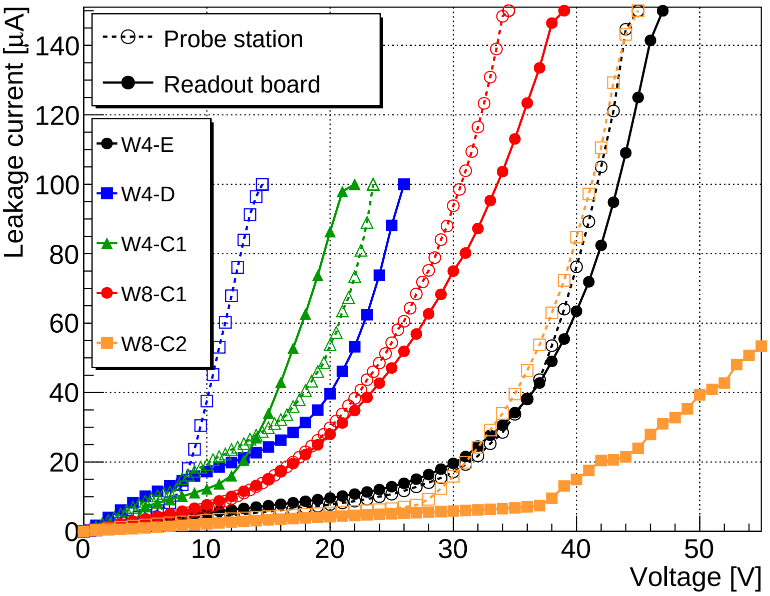

Figure 6.8: Comparison between leakage current measured via the probe station to the measurement on the readout board through the LEMO HV. Only 5 of the 9 devices produced (of the wafers 4 and 8) were measured on the probe station.

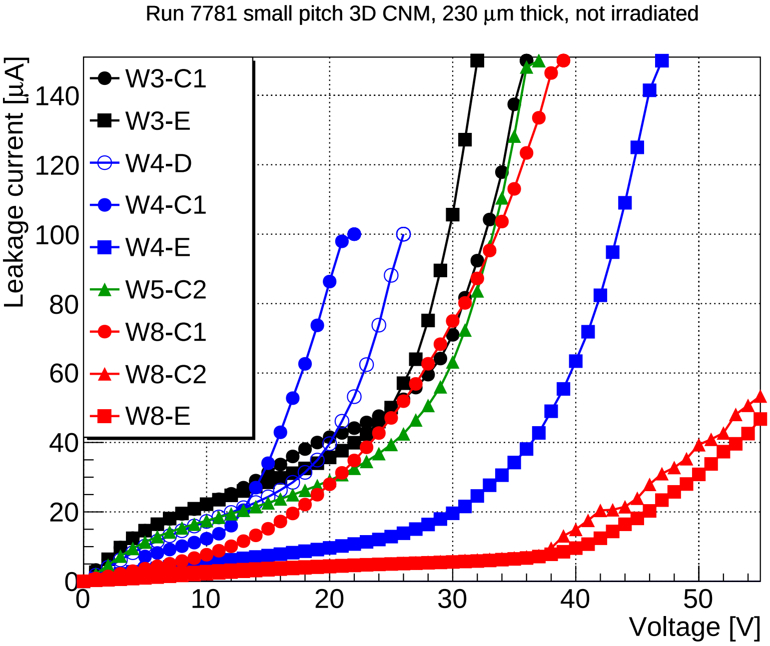

Figure 6.9: Leakage current vs. reverse bias voltage for the 3D small pitch prototypes (run 7781 - see table 6.2) measured at room temperature before irradiation. For each curve the number represents the wafer and the letter the position on the wafer corresponding to figure 6.4.

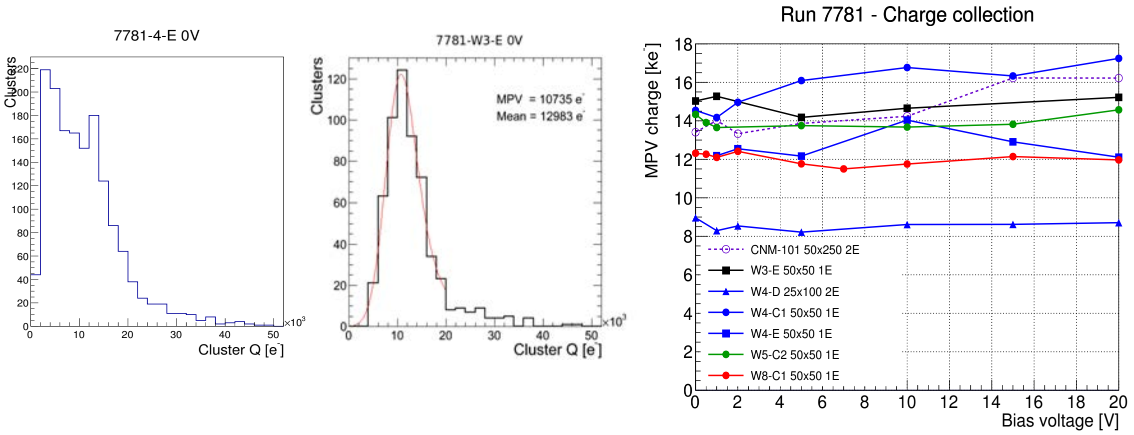

Figure 6.10: (Left) Clustered charge distribution for all the cluster sizes together. (Middle) Clustered charge distribution fitted with a Landau-Gauss (only cluster size 2 - see text). (Right) Collected charge of the small pitch sensors compared to an IBL FE-I4 3D sensor (CNM-101).

pixels that are not being read out. Even with the sensor production problems mentioned in section 6.3, the measured devices can be operated at least to 12 V before going into soft breakdown (see figure 6.9), which is enough for testing purposes since the full depletion is expected to happen at very low voltages before irradiation (see section 6.7). None of these devices have a hard breakdown voltage (the current increases drastically after surpassing the breakdown voltage (as in figure 4.3)), however the soft breakdown voltage (V_{bd}) is defined as the point at which the leakage current slope increases substantially.

The next step is to test the chip communication. In general, for the initial testing the readout system used is the USBpix. The distributions of the Threshold and ToT are homogenized over the chip using the USBpix algorithms. The method to homogenize their values is explained in section 5.3 (as mentioned in that section, typical values of tuning are 1 or 1.5 ke$^-$ threshold with 10 ToT response at 20 ke$^-$ and the noise level is between 100 and 200 e$^-$). All the devices show good performance (similar distributions to the figures 5.9 and 5.10). Once the chip is tuned, a test with a ^{90}Sr source is made to confirm that the charge collection mechanism works properly and to verify the connection between the chip and the sensor. The results of the test with the source are shown in table 6.2. The quality of the devices varies through the production for the reasons explained in sections 6.3 and 6.4.

The collection of charge for the different devices was also studied with the ^{90}Sr source and compared with a standard FE-I4 3D sensor from the IBL production (CNM-101) as can be seen in figure 6.10. The signal given by the FE-I4 chip is the ToT from which the collected charge can be obtained (see section 5.3.4). The source has a divergence and typically several pixels fire for each traversing particle, which are clustered together. In

Device	**3D Guard ring**	**UBM/Batch**	**Assembly date**	**V_{bd} [V]**	**Source Hit map**
W4-C1 50×50 1E L_{el} = 35 μm	yes	Electro-less/1	07/02/2016	12	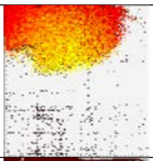
W4-D 25×100 2E L_{el} = 28 μm	yes	Electro-less/1	07/02/2016	17	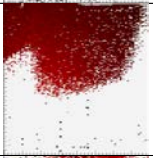
W8-C1 50×50 1E L_{el} = 35 μm	yes	Electro-plate/1	29/04/2016	20	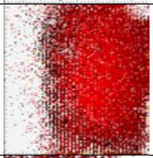
W8-C2 50×50 1E L_{el} = 35 μm	yes	Electro-plate/1	29/04/2016	38	
W8-E 50×50 1E L_{el} = 35 μm	no	Electro-plate/1	29/04/2016	40	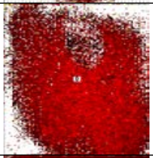
W3-E 50×50 1E L_{el} = 35 μm	no	Electro-less/2	27/07/2016	25	
W5-C2 50×50 1E L_{el} = 35 μm	yes	Electro-less/2	27/07/2016	25	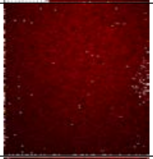
W3-C1 50×50 1E L_{el} = 35 μm	yes	Electro-less/2	27/07/2016	25	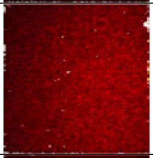
W4-E 50×50 1E L_{el} = 35 μm	no	Electro-less/2	23/03/2017	30	

Table 6.2: Characteristics of successfully mounted and tested devices from run 7781. Note that only one device with pixel size of 25×100 μm^2 has been successfully mounted and only measured before irradiation. The assembly date of the devices is interesting to understand the quality of the UBM (source hit map - see text). A soft breakdown voltage (noted as V_{bd}) usually appeared on these sensors (see figure 6.9 and explanation on text).

order to reduce charge loss to the non sensitive sensor pixels that are not connected to the readout and due to the low resolution of the measured ToT on the FE-I4 chip (only 4-bits), the collected charge was constrained to only events which fire two pixels (see distribution of charge for all cluster sizes in figure 6.10 left). The most probable value (MPV) of the cluster charge is obtained from a Landau-Gauss fit (see figure 6.10 middle). As explained in section 4.3 the expected MPV charge on a 230 μm thick Si is 15.9 ke$^-$. A calibration factor (correction needed between the collected charge and the expected charge on the FE-I4) of 1.4 was calculated with a ^{241}Am and ^{109}Cd sources (see section 5.3.4). The measurements show that for most of the devices the collected charge is around the expected value and similar to the standard FE-I4 reference device even at 0 V within the calibration uncertainties of ∼20%. The source of this large uncertainty comes from the resolution when measuring the ToT of the FE-I4 chips. In the case of one sensor, W4-D, the charge collected is lower than expected. As mentioned before, to adapt the D geometry to the FE-I4 chip each 25×100 μm^2 pixel only has neighbours in one direction, hence more charge is lost to the insensitive regions than for the other geometries.

6.6 3D sensors irradiated to HL-LHC fluences

As mentioned before, the sensors are expected to work in a high radiation environment, hence it is critical to demonstrate that they are able to cope with the fluences expected in the HL-LHC ATLAS pixel detector. Simulations indicate that the maximum expected fluence is 2.8×10^{16} n$_{eq}$/cm^2 in the innermost layer of the detector, including a safety factor of 1.5 [29][63]. Due to the front-end limitations in terms of radiation hardness (the RD53 chip is specified only to withstand 500 Mrad (1×10^{16} n$_{eq}$/cm^2)), it is planned to replace the inner layers of the detector after half of the lifetime, reducing the requirement to 1.4×10^{16} n$_{eq}$/cm^2 (720 Mrad). If the safety factor is not included, the dose is reduced to 470 Mrad.

The pixel sensor leakage current is a critical parameter to study. The current is related to the sensor quality (usually a large leakage current indicates that the sensor quality is low), and it increases with irradiation. It is important to understand the evolution of the leakage current as it impacts on power dissipation and noise. On the other hand, the bias voltage has to be increased with irradiation (also impacts on power dissipation), to ensure that enough charge is collected in the sensor. Also, the current has a strong dependence on temperature which is increased by the dissipated power, and can lead to thermal runaway if an infinite feedback is generated between the dissipated power and the temperature. Thus, irradiated devices need to be cooled in order to avoid the onset on thermal runaway.

The leakage current of three different types of devices was studied: 3D FE-I3 devices

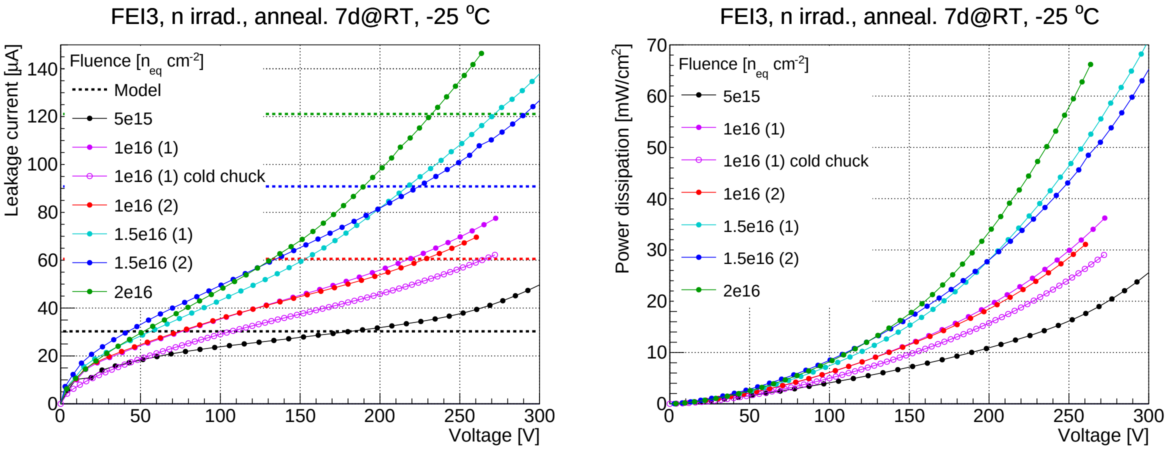

Figure 6.11: Leakage current (left) and power dissipation (right) of FE-I3 sensors from the IBL production irradiated up to HL-LHC fluences, measured in a climate chamber at -25 °C mounted in a readout board. Two different sensors were measured at 1×10^{16} and 1.5×10^{16} n_{eq}/cm^2 (1 and 2). The discontinuous lines correspond to the expected current assuming it is described by radiation-induced bulk damage (see section 4.5 and [39]). For a fluence of 10^{16} n_{eq}/cm^2, sensor 1 was also measured in direct contact with a cold chuck without the readout board (open points) for a better thermal contact and hence more efficient cooling.

fabricated during the IBL production, strip sensors from the small pitch production and the small pitch sensors using the FE-I4 chip mentioned in previous section. The FE-I3 and strip sensors were irradiated with neutrons, while the FE-I4 was irradiated with protons because the FE-I4 chip has tantalum which becomes highly radioactive after neutron irradiation[6] [58]. The irradiations were done uniformly over the surface of the sensors to study the dependence of the leakage current with fluence. A climate chamber was used, set at -25 °C to do the measurements (always with the chip not powered), which was the baseline temperature for the ATLAS detector in the HL-LHC phase when the measurements were performed.

The FE-I3 sensors and the strip detectors were irradiated at JSI Ljubliana and the FE-I4 sensors at KIT. The FE-I3 fluences were of 5×10^{15} (IBL benchmark), 1×10^{16}, 1.5×10^{16} and 2×10^{16} n_{eq}/cm^2 while the strip detectors and the FE-I4 sensors were irradiated to fluences of 5×10^{15} and 1×10^{16} n_{eq}/cm^2. These irradiated FE-I4 sensors were also measured in the beam tests (see section 6.7). All the sensors were mounted on a specific readout boards and annealed during one week at room temperature.

6.6.1 Sensors on FE-I3 chip at HL-LHC fluences

The first 3D sensors irradiated to HL-LHC fluences were fabricated during IBL production and coupled to FE-I3 readout chips (50×400 μm^2 pixel size and 230 μm thickness). The sensors have a configuration of 3 electrodes per pixel, resulting in a L_{el} = 71 μm (larger than the IBL generation, see figure 6.2). However, at first order, one may expect that the leakage current is dominated by the current produced in the bulk [39], hence it is interesting to study also these early devices. The leakage current was measured applying a voltage to the back side of the sensor and connecting the front side through the FE-I3 chip to ground in a similar way than for the FE-I4 chip. Previous measurements at lower fluences tend to show a plateau starting at the voltage where the sensor is fully depleted [64] (or a voltage range where the leakage current has a smaller slope, as in figure 6.9). However, for the high fluences measured here, no real plateau is visible; only for 5×10^{15} n_{eq}/cm^2 there is a region of reduced slope. The expected dependence of the leakage current with fluence is linear at low fluences if dominated by the radiation effects in the bulk [39]:

$$I = \alpha \Phi_{eq} V \tag{6.1}$$

with $\alpha = 4.67\times10^{-17}$ A/cm after one week annealing at room temperature (current related damage rate - see section 4.5), Φ_{eq} is the 1 MeV neutron equivalent fluence and V is the volume of the depleted region. In theory, the current at the plateau should match the model after depletion. The leakage current of equation 6.1 was calculated and compared with the current of the FE-I3 devices and it is shown in figure 6.11. It can be seen that the current is in the range of the expected values for all the fluences, and the measurements match the theory at a voltage ranging 150-250 V. It should be pointed out that two different sensors were measured at fluences of 1×10^{16} and 1.5×10^{16} n_{eq}/cm^2, and their currents show good agreement.

In addition, to verify the thermal contact between the chip and the climate chamber one of the FE-I3 sensors irradiated to a fluence of 1×10^{16} n_{eq}/cm^2 was measured with the chip in direct contact with the cold chuck without the readout board. In this way the chip dissipates the heat better than in the board (in contact only with air inside the climate chamber), hence the temperature of the chip is reduced more efficiently and the measured leakage current is lower. The comparison between the measurements of the current differ by 20% (see figure 6.11).

Charge collection measurements were done also on these devices and compared before and after irradiation [65]. The method to perform these measurements is very similar to the FE-I4 explained in section 6.5. The results are shown in figure 6.12. It can be seen that the collected charge of the non irradiated sensors is in agreement with the expected

---

[6] The activation from tantalum requires a long time to decay to acceptable levels (∼1 year).

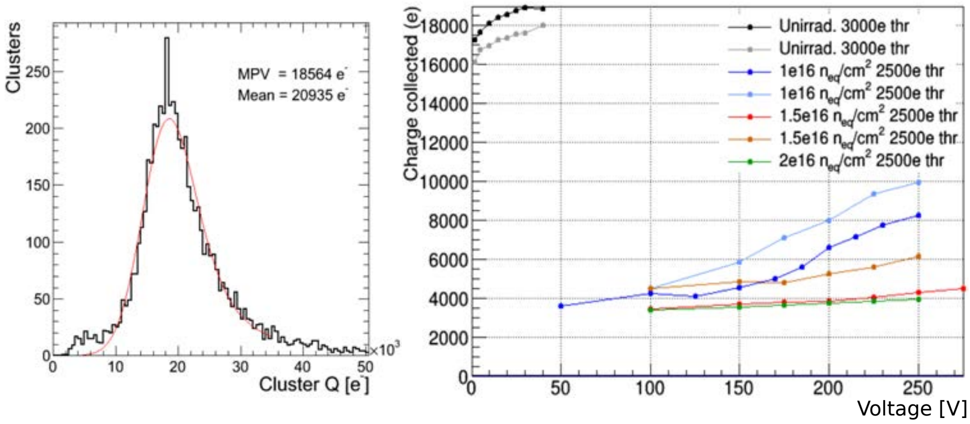

Figure 6.12: (Left) Clustered charge distribution of the FE-I3 sensor fitted with a Landau-Gauss. Note that the binning is much smaller than in the figure 6.10 thanks to the higher number of bits dedicated to measure the ToT in the FE-I3 (8-bit) compared to the FE-I4 (4-bit). (Right) Collected charge of the FE-I3 sensors before and after irradiation of 1, 1.5 and 2×10^{16} n$_{eq}$/cm^2.

value of ∼17 ke$^-$ for 230 μm. For the irradiated devices, this collected charge drops down to 4 ke$^-$ at 2×10^{16} n$_{eq}$/cm^2 at 200 V (still a 20% of the non irradiated at this highest fluence) and 8 ke$^-$ at 1.5×10^{16} n$_{eq}$/cm^2 at 200 V (a 50% of the non irradiated). It is important to point out that these values are for a threshold of 2500 electrons (2.5 ke$^-$) and a L$_{el}$ of 71 μm while the small pitch sensors have lower L$_{el}$ and can be tuned down to 1 ke$^-$. On the other hand, the active thickness of the 3D devices coupled to the FE-I3 chip are 230 μm while for the final sensors of ITk the active thickness will be 150 μm which reduces the collected charge, in contrast to the effect of lower threshold and lower L$_{el}$. Overall, the early results with FE-I3 3D sensors, are quite encouraging in terms of the prospects for radiation hard 3D sensors in ITk.

6.6.2 Small pitch strip detectors at HL-LHC fluences

The leakage current of the strip sensors from the small pitch production which have 3D unit cells of 50×50 and 25×100 μm^2 (L$_{el}$ = 35 and 52 μm respectively) was measured. These strip detectors were studied because their production and testing is easier (and faster) than for the pixel sensors. Strip detectors of 80×80 μm^2 (L$_{el}$ = 57 μm) 3D unit cell from the IBL production, and the FE-I3 from the previous section were also studied for comparison (50×400 μm^2 3E configuration means 3D unit cell of 50×133 μm^2). The strip devices are formed by 128 single strips which are wire bonded together to a readout board where the leakage current of all the strips can be measured together. The aim is to compare the leakage current and power dissipation of the new structures with small pixel

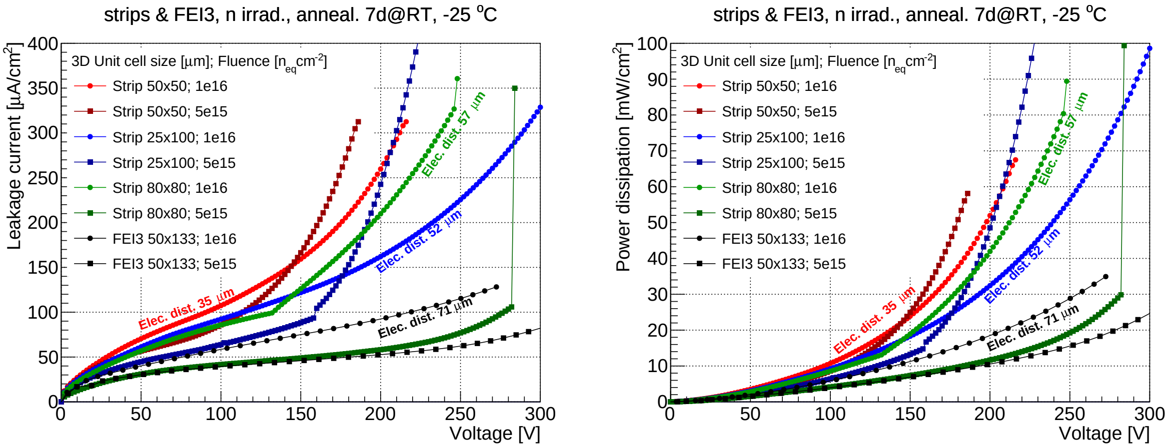

Figure 6.13: Leakage current per area (left) and power dissipation (right) of small pitch irradiated strip detectors measured in a climate chamber at -25 °C, compared to strip detectors and FE-I3 sensors from the IBL production for fluences of 5×10^{15} and 1×10^{16} n_{eq}/cm^2. The inter-electrode distance is specified.

size with the measurements of the devices from the IBL generation. Hence, the current was scaled by area to compare devices of different sizes (since all the devices have the same thickness). The measurements were carried out in a climate chamber at -25 °C. The main differences between the small pitch strips and the FE-I3 3D sensors are the electrode distance and the column diameter. The other parameters of the strips where copied from the IBL production (p-type wafers, thickness, resistivity and double side process - see section 6.3).

As mentioned before, the model predicts a linear dependence between the leakage current and the fluence, and this is approximately confirmed in the figure 6.13 (for example at 100 V, the leakage current increases by a factor of ∼1.5-2 when doubling the fluence for the same electrode distance). The leakage current shows an inversely proportional dependence with the electrode distance at fixed fluence and voltage for most of the devices (only the 80×80 strip at 5×10^{15} n_{eq}/cm^2 not following this scaling). This increase of leakage current at lower electrode distance could be an effect of charge multiplication in higher electric fields at smaller inter-electrode distances or a real effect that generates larger leakage currents with smaller L_{el} (given the larger electrode column density). Nevertheless, the operation voltages for small pitch sensors are lower for smaller 3D cell sizes, as it will be demonstrated in the section 6.7, which will have a compensating effect on the dissipated power.

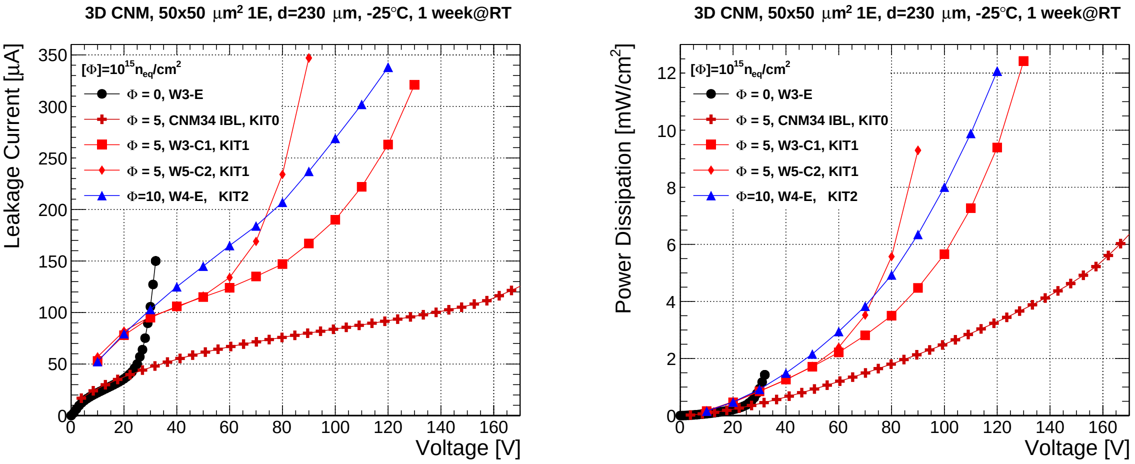

Figure 6.14: Leakage current and power dissipation as a function of voltage before and after uniform KIT irradiation, measured in a controlled climate chamber set at -25 °C with readout chip not powered. Not all the FE-I4 devices from the table 6.2 are represented here since not all were uniformly irradiated, see table 6.3 for the details of the FE-I4 irradiated devices.

6.6.3 Small pitch sensors on FE-I4 chip at HL-LHC fluences

The study of the leakage current dependence with the voltage for the FE-I4 devices has been performed in a temperature controlled climate chamber with the readout chip off to avoid heating up the sensor. The default temperature during testing was -25 °C. The measurements were done with the device mounted on the readout board. As shown in section 6.6.1, due to poor thermal contact of the sensor with the air, the leakage currents have larger values than if the sensor is contacting directly with the cooling medium. For the final ITk application, a better thermal conductivity to the cooling structure is expected, hence the values shown in figure 6.14 are upper limits. The results show the small-pitch prototypes before and after irradiation and a standard $50{\times}250\ \mu\text{m}^2$ 2E IBL FE-I4 for comparison. The current before irradiation is typically 20-40 μA before the breakdown voltage of 15-40 V. It can be seen how the current (before breakdown) increases with fluence, but so does the breakdown voltage, which makes the devices operable at higher voltages after irradiation. The currents of the two different devices at $5{\times}10^{15}$ $\text{n}_{eq}/\text{cm}^2$ agree at low voltages, but the breakdown voltage is different. Comparing to the standard FE-I4 device at the same fluence, it can be seen that the current at a fixed voltage is higher for the new small pitch generation as it was seen in the 3D strip detectors. Again, an explanation could be higher electric fields causing charge multiplication due to the smaller inter-electrode distance and column diameter, or simply that the higher electrode density increases defects in the bulk which lead to higher leakage currents. However, as it will be shown in section 6.7, at the operation point where the benchmark efficiency of

97% is reached, the power dissipation is much smaller for the small pitch sensors than for the IBL devices (40 V for small-pitch, 120 V for IBL and power dissipation of 1.5 vs 3.5 mW/cm^2).

6.6.4 Temperature scaling

As mentioned before, the dependence of the leakage current with the fluence is lineal if it is dominated by the radiation effects in the bulk. This also means that the dependence on the leakage current with the temperature can be described with the formula:

$$\frac{I}{I_0} = \left(\frac{T}{T_0}\right)^2 exp\left(\frac{-E_g}{2k_B}\left(\frac{1}{T} - \frac{1}{T_0}\right)\right), \tag{6.2}$$

with E$_g$=1.2 eV and k$_B$=8.62×10^{-5} eV/K [39]. Measurements of the leakage current of the FE-I3 devices and strips from the previous section were performed at different irradiation levels and temperatures, and the scaling with temperature was confirmed, as can be observed in figure 6.15. This scaling works very well for the strips and the FE-I3 devices. The data follows the model independently of the irradiation level and the pixel size. Overall, this shows that for this thickness (230 μm) the leakage current after irradiation is mostly dominated by bulk effects.

6.7 Beam test characterization of the sensors

The irradiated small pitch FE-I4 pixel detectors were measured in the beam test at the Super Proton Synchrotron (SPS) H6 beam line at CERN with 120 GeV pions. The HSIO-II readout system was used for communication and data transfer from and to the FE-I4 readout chip. The devices were cooled in a custom made cooling box in the beam test to temperatures estimated between -10 and -30 °C on sensor. The temperature set on the cooling box is between -40 and -50 °C, but it is higher on the sensor due to the heating caused by the power dissipated on the chip. This estimated temperature on sensor was extracted from the leakage current values using the equation 6.2 from section 6.6.4.

As explained in section 5.4 for the reconstruction of reference tracks in the beam test the EUDET telescope was used in general and the reconstruction and analysis were done with the EUTelescope and TBMon2 frameworks respectively. The DUT are placed between the two arms of the telescope which are made of 3 planes each. The triggering is done with scintilators of 1×2 cm^2, so that only part of the FE-I4 DUT is studied for each configuration. To take into account the 20% of the small pitch prototype that is connected to the readout (as explained in section 6.3), the tracks used in the analysis were constrained to the active area inside the FE-I4 pixel. In order to also avoid the smearing effects due to the telescope resolution, the region of interest (ROI), for which

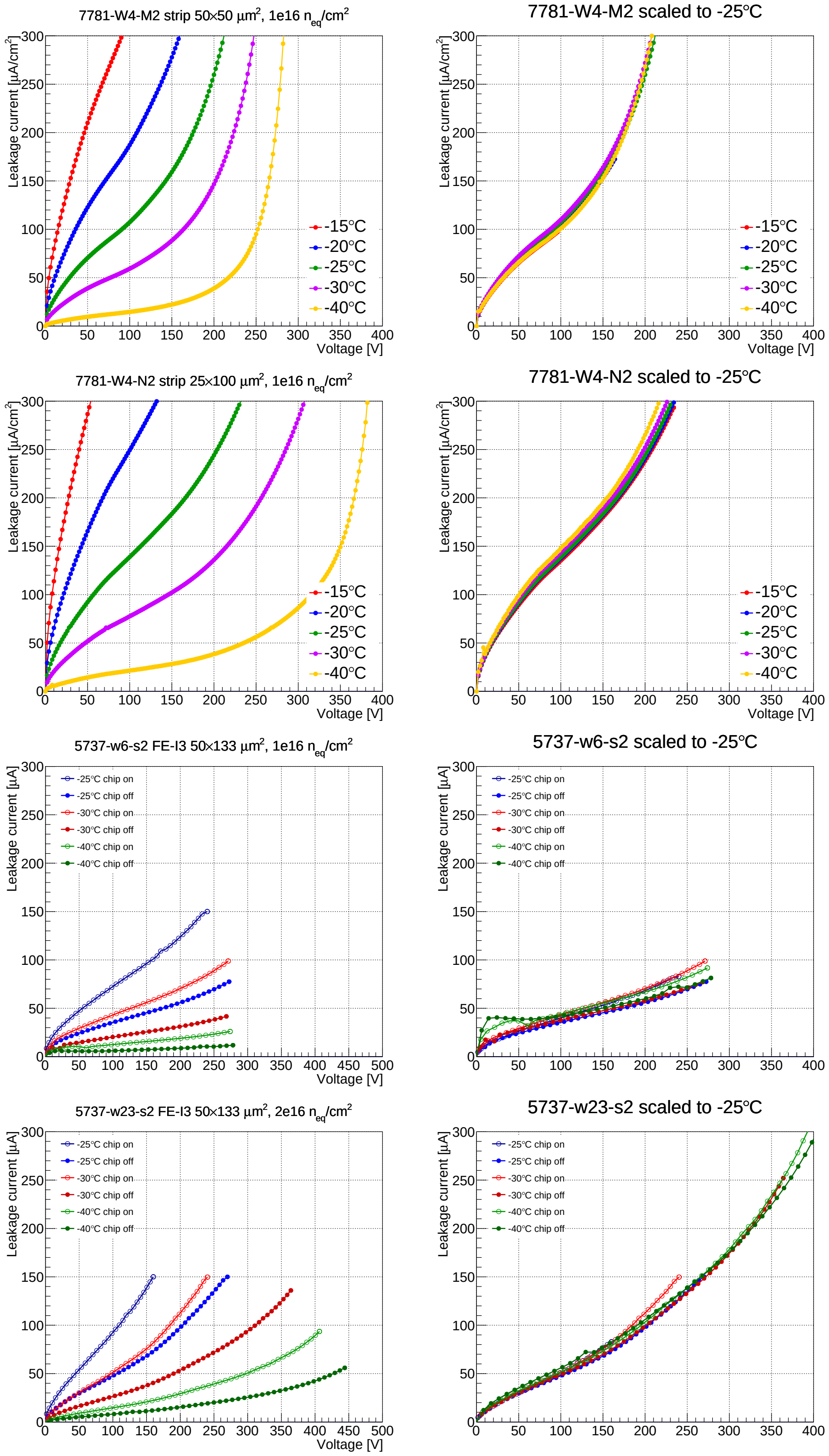

Figure 6.15: Leakage current of strips and FE-I3 irradiated with neutrons at different fluences and at different temperatures (left) scaled to the same temperature (right). The scaling to the same temperature was done using equation 6.2.

the average results will be shown in the following, was further reduced to the central 50×50 μm^2 region of the two horizontally adjacent sensor pixels that were readout (see figure 6.16 top left). For the 25×100 μm^2 pixels the central region was also taken, but due to the absence of a neighbor active pixel in the vertical direction both directions were reduced resulting in an area of 2.5×100 μm^2 (see figure 6.16 top right).

The beam test measurements were done at perpendicular beam incidence with respect to the sensor surface (0° tilt), as well as at 15° tilt and at a tilt of 80°. These angles explore the different incident tracks that will be encountered in the final detector.

6.7.1 Analysis of sensors before irradiation

The first devices measured in a beam test were the W4-C1 (50×50 μm^2) and W4-D (25×100 μm^2), see table 6.2. The EUDET telescope had some problems during the data taking hence the 3D FE-I4 telescope was used (see section 5.4.2). The device W3-E with pixel size of 50×50 μm^2 was measured in the EUDET telescope during a later beam test. Due to the hybridization problems mentioned in section 6.3 and to the fact that only one device with this configuration is present on each wafer, no other 25×100 μm^2 pixel size sensor was measured. The chip calibration of these devices was set to 1500 e^- of threshold and a ToT of 10 bunch crossings for 20ke^- (see section 5.3 for an explanation of the chip calibration procedure).

Figure 6.16 shows the in-pixel hit efficiency maps for reconstructed tracks restricted to the active area of the two horizontally neighboring pixels for W4-C1 (top left) and W4-D (top right) taken with the 3D FE-I4 telescope. The middle hit efficiency map corresponds to the data taken with the EUDET telescope of the device W3-E. This device has better quality thanks to the improvements in the fabrication process (see section 6.3) but confirmed the results obtained on the device W4-C1. The hit efficiency for this ROI as a function of bias voltage is shown in the figure 6.16 (bottom) for the three measured devices compared with a standard FE-I4 reference at 0° and 15°.

The small pixel devices reach their plateau efficiencies of 96–98% at already at 0–2 V. The two devices measured with the FE-I4 telescope show ∼1% lower efficiency than the one measured with the EUDET telescope. The results obtained with EUDET telescope are more reliable thanks to the higher granularity of the telescope planes. The standard FE-I4 device needs 4 V for similar full efficiency due to larger inter-electrode distance and hence later full depletion. The high efficiency found in the small pixel devices can be explained thanks to the large depletion region and signal just due to the built-in voltage of the pn junction (as explained in section 4.2) in combination with the small inter-electrode distance. High-quality class standard FE-I4 devices can even reach up to 99% at 0° [42], which might be achievable as well for small pixel devices in the future. However, it is shown that the efficiency can be improved (to 99.9% in the standard FE-I4 and ∼98.5-99%

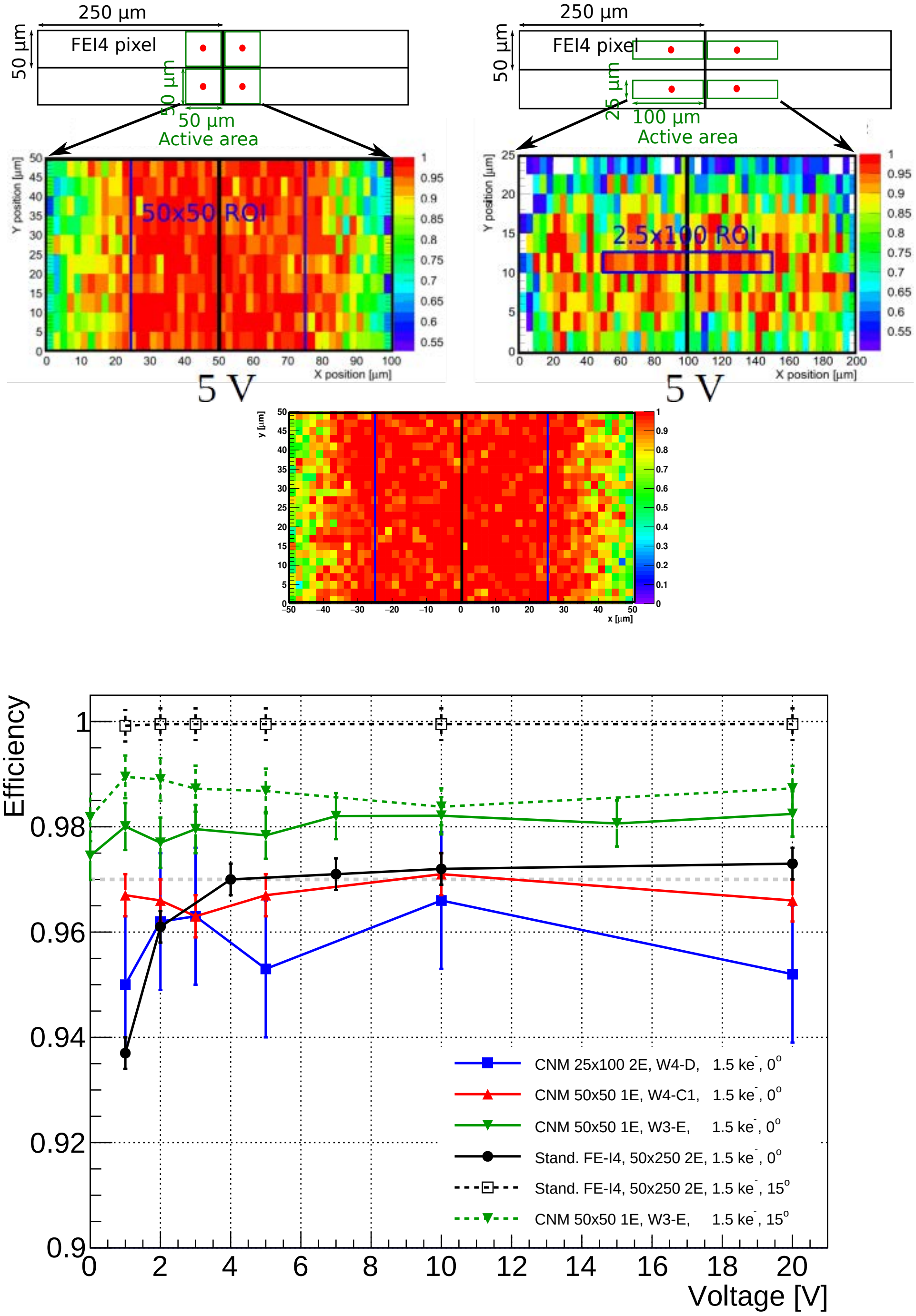

Figure 6.16: Top: sketch of a 50×50 μm^2 (left) and 25×100 μm^2 (right) sensor pixel matched to the FE-I4 chip pixels. Middle: the corresponding hit efficiency maps for 2 horizontally neighboring sensor pixels at 5V measured with the 3D FE-I4 telescope (above) and with the EUDET telescope (below) for the 50×50 μm^2. Bottom: average hit efficiencies in ROI vs. voltage for 50×50 and 25×100 μm^2 pixel geometries compared to a standard FE-I4 at 0 and 15°.

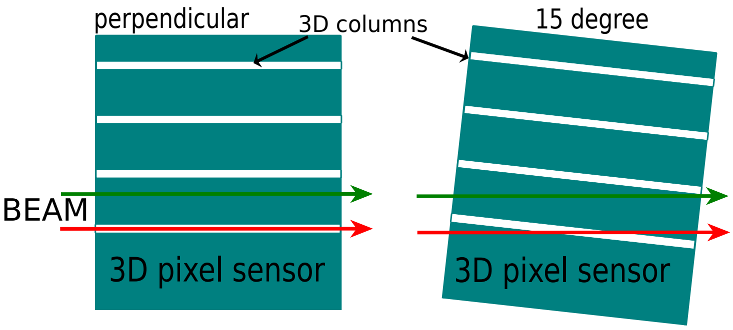

Figure 6.17: Left: beam test in perpendicular incidence where the red particles pass the sensors undetected when coinciding with a 3D column. Right: beam test with a device at 15° favors that the red particles do not pass undetected.

in the small pixel devices[7]) by tilting by 15° the device due to minimizing the influence of low efficiency regions from the 3D columns or low field areas (see figure 6.17).

The small pitch devices reach the benchmark efficiency of 97% at perpendicular incidence even without bias voltage before irradiation thanks to the lower electrode distance compared to the standard FE-I4 devices. The 25×100 μm^2 2E device marginally reaches 97% efficiency, but it is expected that this limitation is due to a residual charge sharing effect that even affects the restricted ROI selected for this device. The perpendicular beam incidence is the worst case scenario of incidence tracks, and at 15° and improvement of efficiency is already observed. The improvement on operation voltage (defined as the voltage needed to reach the benchmark efficiency of 97%) for the small pitch devices shows already that they are a good candidate for the HL-LHC upgrade. To verify that these sensors fulfill the requirements on radiation hardness, they were irradiated and measured in beam tests.

6.7.2 Irradiations

To irradiate the small pixel devices two facilities were used, KIT and CERN-PS for uniform and non uniform irradiations respectively. At KIT, three devices were irradiated. Two of them (W3-C1 and W5-C2) to 5×10^{15} and one (W4-E) to 1×10^{16} $\mathrm{n}_{eq}/\mathrm{cm}^2$. The devices were irradiated at -36 °C and annealed for seven days at room temperature (∼22 °C) after irradiation (referred to as "7d@RT"). The fluence was measured with a nickel foil with an accuracy of 10%. The irradiation facility and fluence of 5×10^{15} $\mathrm{n}_{eq}/\mathrm{cm}^2$ were chosen to directly compare the new small pixel sensors with the IBL generation. Thanks to the uniformity of the fluence over the sensor surface the analysis and the determination of

---

[7] This difference can be originated from a charge loss to the insensitive areas of the device. The hit efficiency increases up to 99.9% with the first production of sensors coupled to the RD53A chip [69].

Device		Irradiation	$\Phi_{eq}[10^{15}$ $n_{eq}/cm^2]$		TID[MGy]		Annealing	Status
Name	Geometry	Step+Label	Step	Total	Step	Total	step	
CNM small pitch run 7781 Irradiations and Beam Tests								
W3-E	50×50 1E	Unirradiated	-	-	-	-	-	Measured
W8-C2	50×50 1E	Unirradiated	-	-	-	-	-	Detached
W8-E	50×50 1E	Unirradiated	-	-	-	-	-	Not working
W4-D	25×100 2E	PS1	15	15	6.6	6.6	7d@RT	Not working
W4-C1	50×50 1E	PS1	15	15	6.6	6.6	7d@RT	Measured
		PS3	11	26	4.8	11.4	18d@RT	Measured
		PS4	6	31	2.6	13.6	15d@RT	Not working
W8-C1	50×50 1E	PS1	15	15	6.6	6.6	7d@RT	Not working
W5-C2	50×50 1E	KIT1	4.6	4.6	6.9	6.9	8d@RT	Measured
		PS3	10	15	4.4	11.3	18d@RT	Not working
W3-C1	50×50 1E	KIT1	5.4	5.4	8.1	8.1	8d@RT	Measured
		PS2	7	12	3.1	11.2	15d@RT	Working
		PS3	11	23	4.8	16.0	18d@RT	Measured
		PS4	5	28	2.2	18.2	15d@RT	Measured
		PS5	3	31	1.3	19.5	21d@RT	Working
W4-E	50×50 1E	KIT2 NoAnn	10.4	10.4	15.6	15.6	0	Measured
		KIT2	10.4	10.4	-	15.6	7d@RT	Measured
CNM IBL runs (earlier studies)								
CNM34	50×250 2E	KIT0	5	5	7.5	7.5	120min@60 °C	Measured
CNM-NU-1	50×250 2E	PS0	6	6	2.6	2.6	7d@RT	Measured
CNM-NU-2	50×250 2E	PS0	9	9	4.0	4.0	7d@RT	Measured

Table 6.3: Devices and irradiations. For the non uniform irradiations, the values are refered to the maximum achieved in the peak. For more details on the sensor properties see sections 6.2 and 6.3.

the power dissipation is simpler. The higher fluence of 1×10^{16} n_{eq}/cm^2 is chosen due to its proximity to the ITk baseline target fluence assuming one replacement for the inner layer. Higher fluences were not considered due to the low energy protons provided by KIT, since they deliver a high ionization dose which could damage the FE-I4 chip.

To reach higher fluences beyond the baseline scenario while avoiding a large ionization dose, the 24 GeV proton beam of the CERN-PS was used. These higher energy protons provide higher fluences while reducing the ionization dose provided by KIT (see section 5.5). The beam profile varied in the different irradiation campaigns between 12 and 20 mm FWHM, providing a non uniform irradiation over the area of the sensor and allowing to study a broad range of fluences on one single detector. The inconvenient of the non uniform irradiation is that the irradiation profile and its uncertainties need to be determined. The profile has been determined firstly using beam monitors in the beam line for all irradiations. The overall average fluence over the sensors has been obtained with gamma spectroscopy of an activated 20×20 mm^2 aluminum foil for each irradiation. These two methods were found to be consistent with each other. Two working sensors

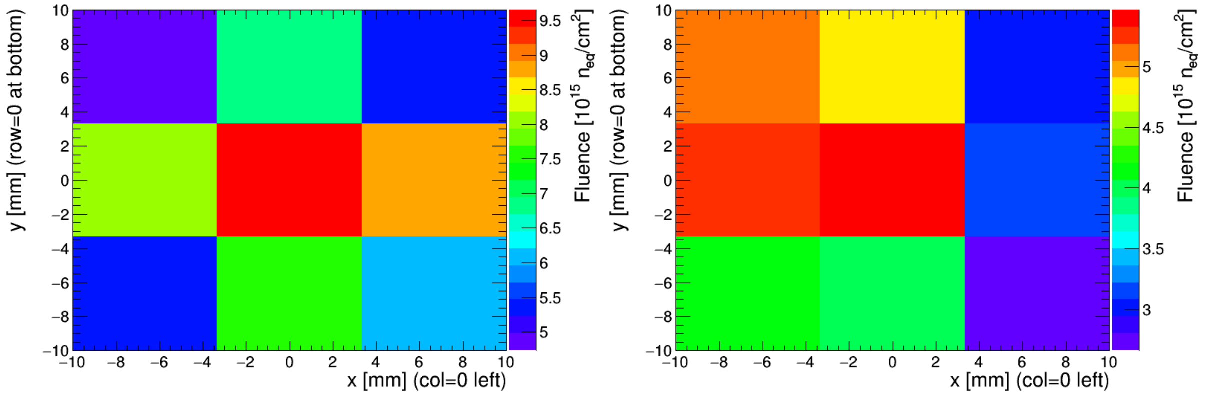

Figure 6.18: Measured beam profiles of the PS3 (left) and PS4 (right) beam periods using a matrix of 3×3 Al sub-foils.

were irradiated at CERN-PS (W4-C1 and W3-C1, the latter after the uniform irradiation at KIT). The devices are irradiated at room temperature. Moreover, after each irradiation step, about 1–3 weeks of storage at room temperature were needed for some initial decay of short lived isotopes before handling. This extra annealing time was added to the baseline of 7 days. The details of all the irradiated devices, irradiations and annealing times are included in table 6.3. It is important to say that for these irradiations the chip was pushed significantly beyond its specifications since it was only qualified for the IBL with a TID of 250 Mrad and fluences of $5{\times}10^{15}$ n_{eq}/cm^2.

A more detailed fluence was determined for the periods PS3, PS4 and PS5 (see table 6.3) by cutting the foil in 3×3 equal sub-foils, which were measured individually and fitted with a Gaussian. This also allows to determine the center of the beam with respect to the foil. As can be seen from figure 6.18, the beam hit the foil centrally for PS3, but with an offset of 3.5 mm in x and 2.1 mm in y for PS4. For PS1 and PS2 no sub-foil method was performed and the beam center has been determined in-situ on the pixel devices themselves using the fluence dependence of the noise, the threshold before tuning and the optimal chip parameter values after threshold tuning. This is only possible for the first irradiation step of each device since subsequent irradiation steps overlay each other. The resulting integrated fluence distributions for each combination of studied pixel devices and irradiation periods are shown in figure 6.19 top. The peak fluences reached range from $1.5{\times}10^{16}$ to $2.8{\times}10^{16}$ n_{eq}/cm^2. The maximum fluence quoted in the analysis of section 6.7.4 can be slightly lower due to large disconnected regions of device W4-C1 (roughly the 60% of the sensor, see table 6.2) and binning effects.

The fluence uncertainties have been estimated by varying the following parameters: the fluence normalization by 7% (PS) or 10% (KIT) according to the uncertainties quoted by the irradiation centers; the beam center by 1 mm; the Al foil centre with respect to the

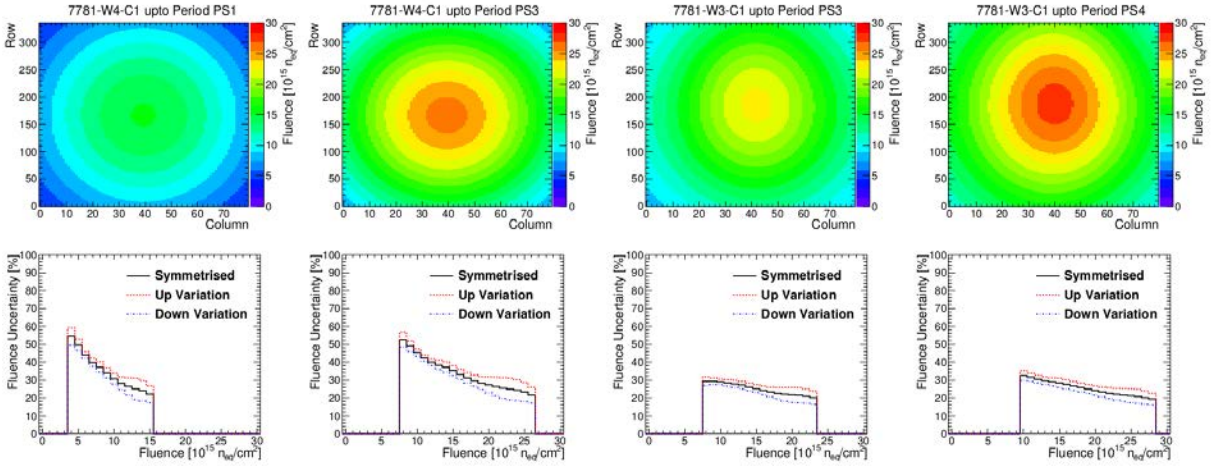

Figure 6.19: Top: integrated fluence maps as a function of pixel column and row numbers for all combinations of devices and PS irradiation period studied. Bottom: corresponding systematic uncertainty as a function of fluence (up and down variations, as well as their symmetrized mean values).

device by 1 mm; and the beam σ by 1 mm. Since these irregular systematic shape effects do not propagate following the standard uncertainty formula of Gaussian distributions, a very conservative estimate has been obtained using the most extreme deviation of all variation combinations. The resulting maximum deviation as a function of fluence is shown in figure 6.19 bottom after each integrated fluence period. For a pure PS irradiation (W4-C1, PS1 and PS3), the uncertainty increases steeply from the highest fluence range with typically about 20% to the lowest fluence range with up to 50%. For W3-C1, this dependence is less strong due to the fact that the first irradiation step has been performed at KIT with a flat 10% normalization uncertainty.

6.7.3 Analysis of uniformly irradiated sensors

The hit efficiency is defined as the fraction of events in which a particle passing through a DUT causes a recorded hit to the total number of tracks reconstructed by the telescope, as explained in section 5.4.4. In this section the hit efficiency was studied for three devices, irradiated in KIT to 5×10^{15} n_{eq}/cm^2 (W3-C1 and W5-C2) and to 1×10^{16} n_{eq}/cm^2 (W4-E). In this case, the chip calibration used for these uniformly irradiated devices is 1000 e^- of threshold with a ToT of 10 bunch crossings for 20ke$^-$, and in some cases a threshold of 1500 e^- was also used. The minimum hit efficiency target for ITk is 97% throughout the whole lifetime since lower values would cause problems for track pattern recognition [63]. The hit efficiency in the central ROI as a function of bias voltage for an unirradiated device and the ones irradiated at the different thresholds are shown in figure 6.20 at 0°

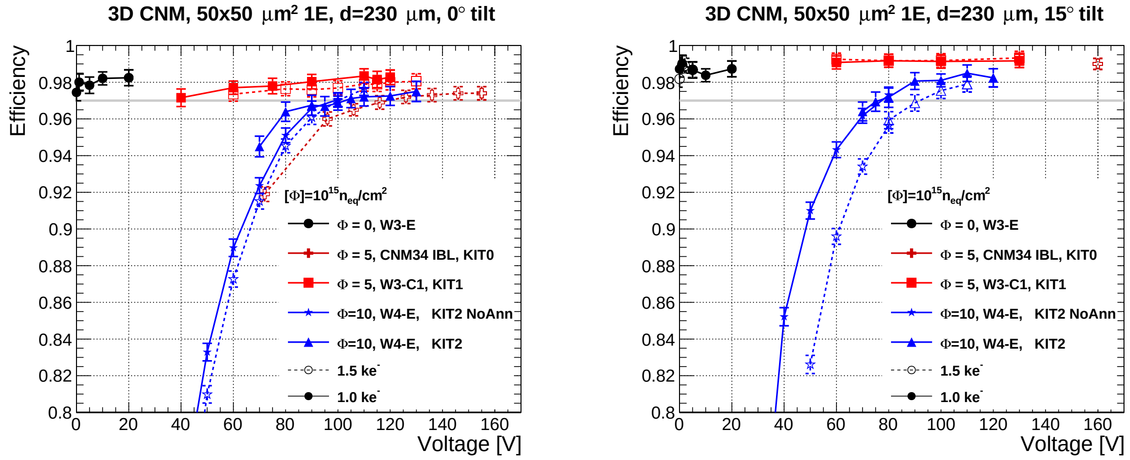

Figure 6.20: Hit efficiency as a function of voltage before and after uniform irradiation at KIT at 0° (left) and 15° (right) tilt. The full markers refer to a threshold of 1.0 ke$^-$, while the open ones refer to 1.5 ke$^-$. Uncertainties shown are statistical and systematic combined.

(left) and 15° (right) and compared to the results obtained for IBL-like FE-I4 devices. Systematical uncertainties as obtained from repeated measurements and different analysis variations are estimated as 0.3% and added in quadrature to the statistical uncertainties. The efficiency is found to be slightly lower at 0° compared to 15° due to the effect shown in figure 6.17; a particle can pass exactly through a insensitive 3D column at 0° while this is not possible after tilting. The efficiency at 1.5 ke$^-$ threshold is slightly lower that at 1.0 ke$^-$. The hit efficiency before irradiation is also shown for the device measured with EUDET telescope. At $5{\times}10^{15}$ n$_{eq}$/cm^2, the efficiency at 1.0 ke$^-$ threshold and 0° reaches the ITk benchmark of 97% already at 40 V, increasing to 98% at about 100 V. At 15°, a plateau efficiency of 99% is observed.

It can be seen that the efficiency of the new small pitch generation with $50{\times}50$ μm^2 1E pixels is significantly higher than the one for the IBL generation with $50{\times}250$ μm^2 2E pixels (which reaches 97% only at 120 V), thanks to the smaller inter-electrode distance and hence less trapping. At $1.0{\times}10^{16}$ n$_{eq}$/cm^2, the efficiency drops at a fixed voltage with respect to lower fluences, but 97% is reached at about 100 V (80 V) for 0° (15°) tilt at 1.0 ke$^-$ threshold. The two measurements before and after annealing to one week at room temperature agree well (in particular in the voltage needed for 97% efficiency), except for low voltages (70–80 V) at 0° tilt, for which the annealed device shows a few % higher efficiency. It is not understood if this is a real annealing effect or an artifact of the analysis, but no other annealing studies were done.

From the hit efficiency measurements, the power dissipation at the point of operation (minimum voltage needed to achieve the ITk benchmark efficiency of 97%, named V$_{97\%}$) can be extracted. The operation point for a fluence of $5{\times}10^{15}$ n$_{eq}$/cm^2, is 40 V which gives a power dissipation of 1.5 mW/cm^2 and for a fluence of 1×10^{16} n$_{eq}$/cm^2 the operation voltage is 100 V, giving a power dissipation of 8 mW/cm^2 (see figure 6.14). The most radiation hard planar pixel technology with 50×50 μm^2 pixels and 100 μm thickness, evaluated to 1.0×10^{16} n$_{eq}$/cm^2 has a V$_{97\%}$ about 500 V with a power dissipation of 25 mW/cm^2 [67]. This value is about 3 times bigger than for the 50×50 μm^2 1E 3D sensors, demonstrating that the 3D technology with small inter-electrode distance has superior radiation hardness while consuming less power.

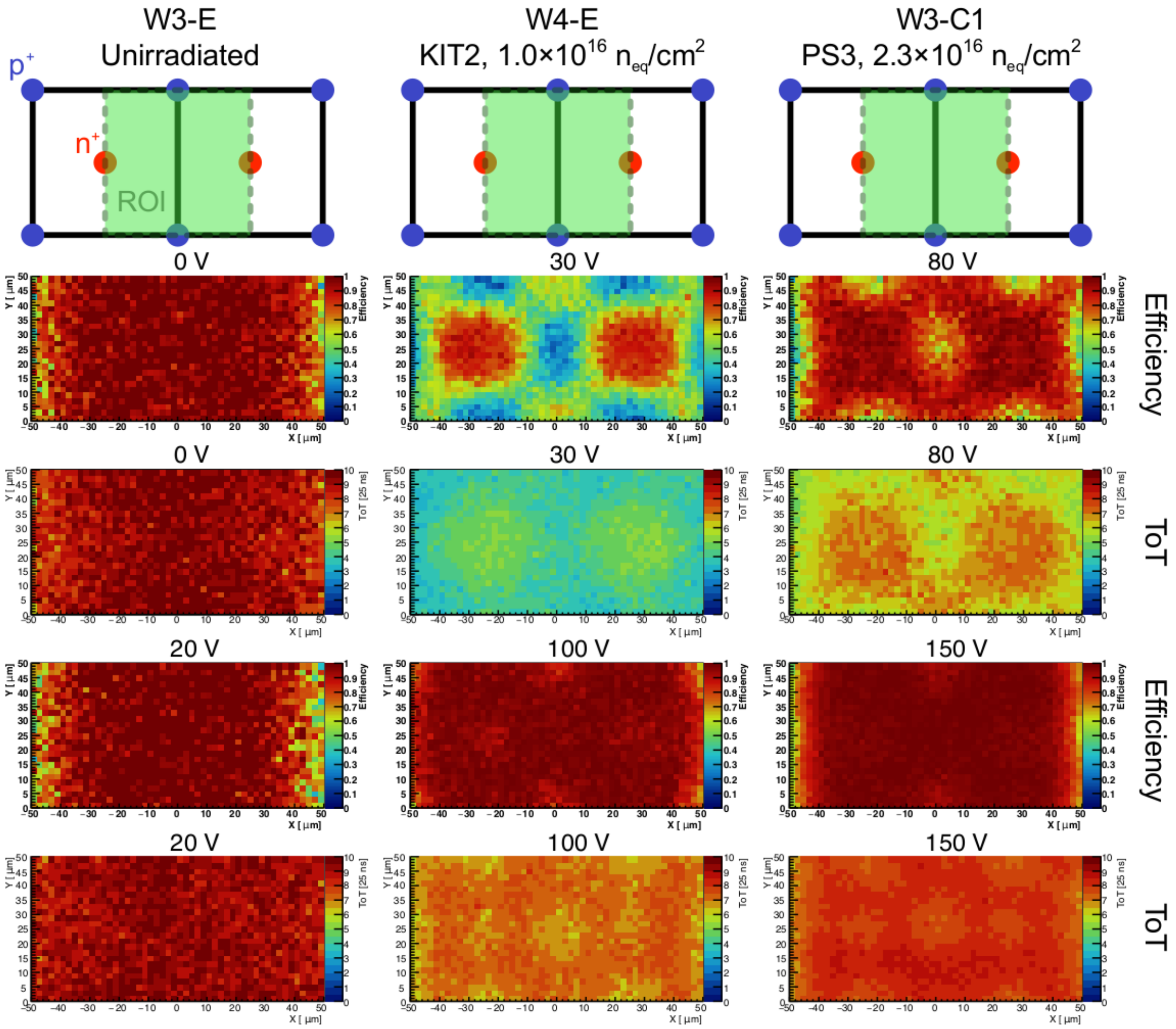

Figure 6.21: Top: sketch of two adjacent pixels with 50×50 1E configuration. The p$^+$ columns are drew in blue and the n$^+$ in red. Bottom: In-pixel average-ToT and efficiency maps restricted to the sensitive area of two adjacent 50×50 μm^2 sensor pixels connected to the readout chip for selected samples, fluences and voltage.

In figure 6.21 the in pixel efficiency maps at 0° tilt are shown, along with their average ToT maps, of two adjacent 50×50 μm^2 sensor pixels at different voltages for three devices: before irradiation at 0 and 20 V, after uniform irradiation to 1.0×10^{16} n$_{eq}$/cm^2 at 30 and

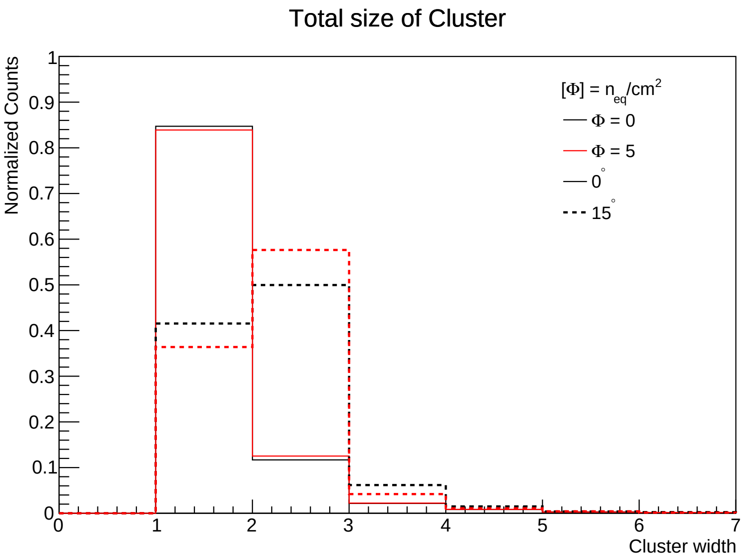

Figure 6.22: Cluster size distribution of the non irradiated sensors and irradiated at $5{\times}10^{15}$ n_{eq}/cm^2 with a voltage higher than $V_{97\%}$ at 0° and 15°.

100 V, and after a non uniform peak fluence[8] of $2.3{\times}10^{16}$ n_{eq}/cm^2 at 80 and 150 V[9]. Before irradiation, the ToT and efficiency is observed to be very uniform and high, even at 0 V. Only at the edges at $x = \pm 50$ μm close to the insensitive area, the efficiency is reduced due to the telescope resolution smearing. After irradiation, the ToT drops in the area between p^+ columns due to the larger drift distances and the smaller electric fields (hence having low efficiency) and the ToT is higher around the 3D columns, especially around the n^+ junction columns in the middle of the $50{\times}50$ μm^2 pixel sensor, which leads to relatively high efficiencies there. However, as can be seen, at high voltages the absolute value as well as uniformity of both parameters are restored. Only small effects are seen from the partly insensitive 3D columns, which sometimes cause locally low charge and inefficiencies at 0° tilt. This effect is less pronounced here than for previous generations due to the fact that these columns are non fully passing through, the diameter has been reduced with respect to the IBL generation by 2 μm down to nominally 8 μm, and the columns are narrower at the tip (see section 6.3). Moreover, the telescope resolution of about 4 μm is close to the column diameter and is hence diluting the effect.

The cluster size is define as the number of hits produced by a single particle in the detector (see section 5.4.4). For perpendicular incidence the most probable value is 1 while for 15° incidence is 2. It is important to say that the maximum cluster size distribution

---

[8] The real fluence on the sensor is the average over all the pixels, hence it is lower than the specified here.

[9] The in pixel efficiency map is averaged over all the pixels, hence not considering the different fluences on each pixel (see next section for detailed analysis).

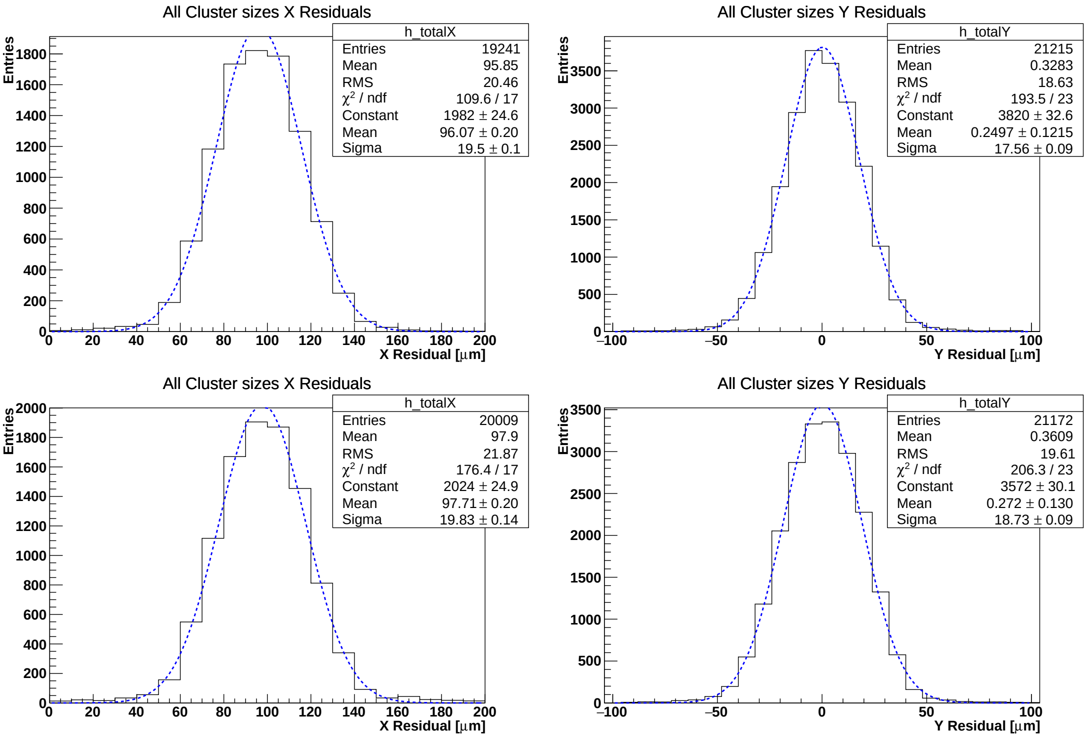

Figure 6.23: Residual distribution of non irradiated sensors at 0 V (top) and 20 V (bottom) in X (left) and Y (right).

of the small pitch sensors in X is 2 by construction (see figure 6.5). The distributions for non irradiated devices and the devices irradiated uniformly at KIT to 5×10^{15} n_{eq}/cm^2 are shown in figure 6.22. The cluster size 1 for perpendicular incidence is the dominant while cluster size 2 becomes very relevant when the incidence angle is 15°. There is no relevant difference between the irradiation levels for the cluster size.

The spacial resolution of the detector can be obtained by subtracting the extrapolated position of the track calculated by the telescope to the real position of the hit on the DUT. Some distributions at different voltages are shown in figure 6.23. The resolution obtained from these residuals are calculated by doing a Gaussian fit and taking the standard deviation. It can be seen from the fit that the resolution of the detector is $\sim$20 μm in both X and Y, as expected from the pixel size of 50×50 μm^2 $(50/\sqrt{12})$.

6.7.4 Analysis of non uniformly irradiated sensors

To do the analysis of the non uniformly irradiated devices, the fluence on the device has been determined as explained in section 6.7.2. The efficiency is then calculated combining the fluence map over the sensor surface with the particle hitmap in order to estimate the efficiency for different fluences. The devices measured where the W4-C1 and the W3-C1, irradiated in different steps at PS (check details in table 6.3). They were usually measured

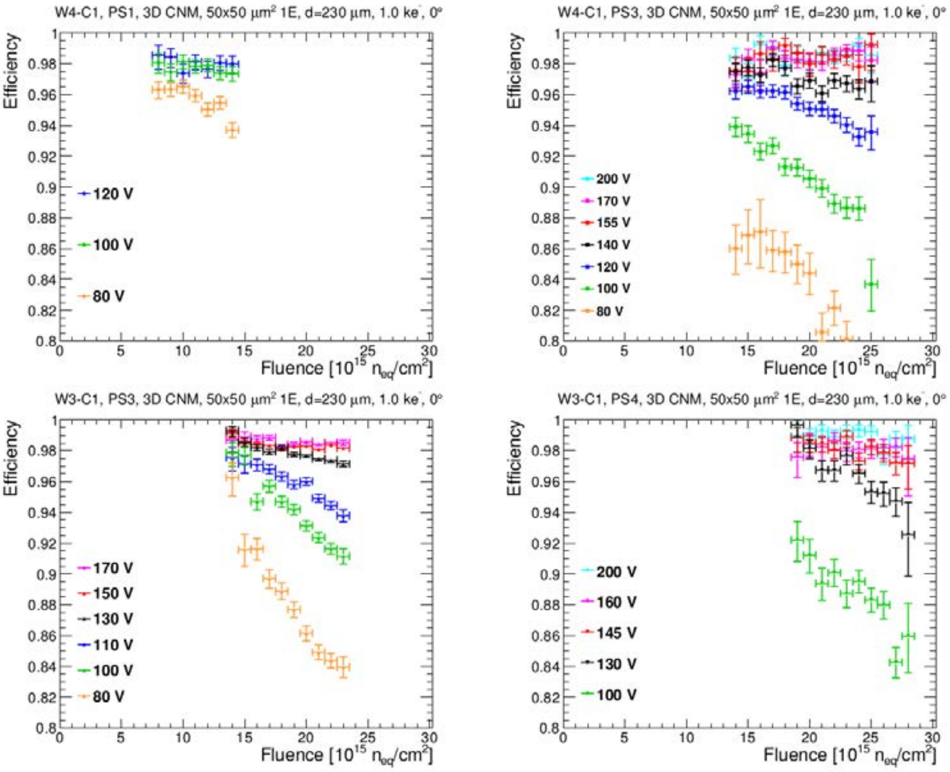

Figure 6.24: Hit efficiency as a function of fluence for different voltages at 0° and 1.0 ke$^-$ obtained from one single pixel device: W4-C1 (top) and W3-C1 (bottom) at two different irradiation periods (left/right). The bars shown refer to combined statistical and systematic uncertainties for the efficiency and the bin size for the fluence. The systematic fluence uncertainties as displayed in figure 6.19 are larger than each bin and are not shown for visibility.

at 0° and sometimes at 15°, but the reconstruction on EUTelescope for the inclined cases was not successful (the Millepede-II algorithm did not manage to align the devices). The standard tuning was a threshold of 1.0 ke$^-$ with a ToT response of 10 bunch crossings at 20 ke$^-$. The tuning of non uniformly irradiated devices is specially difficult to perform since the non uniform radiation damage on the chip requires that the chip register values are set as a function of the pixel position. Nevertheless, in most cases after some manual fine tuning of the register values the results were satisfactory. However, at the highest fluence step measured (2.8×10^{16} n$_{eq}$/cm^2), the targeted ToT calibration was not possible hence a value ofToT of 10 bunch crossings for 10ke$^-$ was used instead. This problem with the calibration is highly related with the chip, which is already working way beyond its specifications, hence no further studies were performed. A more systematic study of the chip calibration effects will be performed in combination with the RD53A readout chip, which is designed specifically for the HL-LHC pixel upgrade, to be operated at higher fluences and lower thresholds than the FE-I4.

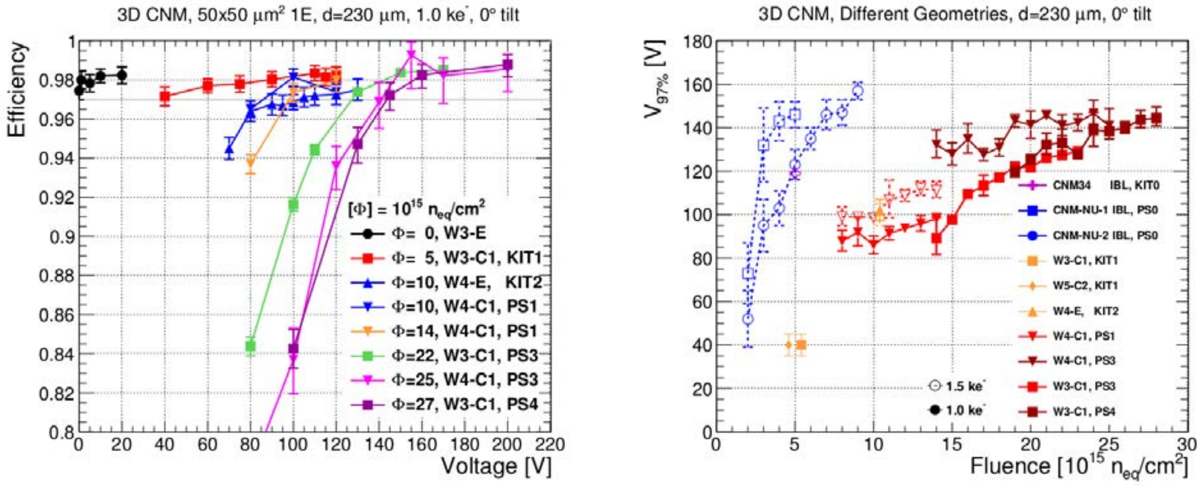

Figure 6.25: Left: hit efficiency as a function of voltage for different fluences at 0° and 1.0 ke$^-$. Right: V$_{97\%}$ as a function of fluence at 0° tilt for different devices. The small pitch 50×50 μm^2 1E devices (red/orange) are compared to the IBL 50×250 μm^2 2E generation (blue/magenta). Full markers refer to a threshold of 1.0 ke$^-$, open ones to 1.5 ke$^-$. The uncertainties shown are statistical and systematic combined. The fluence uncertainty from figure 6.19 is not displayed for visibility.

The efficiency over one device as a function of fluence for different voltages at 0° and 1.0 ke$^-$ is shown in figure 6.24. At low voltages the expected decrease of efficiency with fluence is observed. This confirms that the position of the peaks determined in section 6.7.2 are fairly well determined. At high voltages no fluence dependence is observed since the plateau maximum efficiency is uniformly reached in all the pixels (see figure 6.21 bottom right). The efficiency values at the same voltage and fluence agree reasonably well for the different devices and periods, except for W4-C1 in period PS3 in the low fluence region, which is observed to be systematically lower than the others. However, this can be understood when taking the systematic fluence uncertainties into account, which increase significantly with decreasing fluence as observed in section 6.7.2.

In the figure 6.25 (left) a compilation of the voltage dependence of the efficiency for non irradiated, uniformly irradiated and non uniformly irradiated devices is shown. The results of the latter are evaluated at (or close to) the highest fluence of each device, where systematic fluence uncertainties are lowest. At 1.0×10^{16} n$_{eq}$/cm^2, the curves for KIT and PS irradiation agree reasonably well. The expected fluence degradation at fixed voltage is observed. However, even at the highest fluence studied, a plateau efficiency of 98% is obtained. The voltage V$_{97\%}$ is evaluated from linear interpolation and compared to measurements of the IBL 50×250 μm^2 2E generation [66] as a function of fluence (see figure 6.25 (right)). As expected, a rising trend is visible, but even at the highest measured fluence of 2.8×10^{16} n$_{eq}$/cm^2, V$_{97\%}$ does not exceed 150 V for the new small pitch

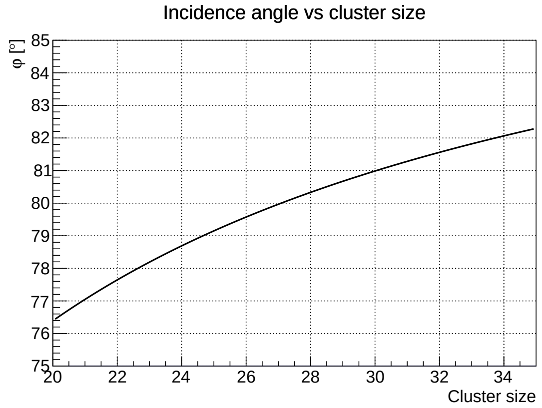

Figure 6.26: Cluster size versus incident angle using equation 6.3.

generation. At the ITk baseline fluence of 1.4×10^{16} n_{eq}/cm^2 (assuming one replacement), $V_{97\%}$ is only about 100 V. The significant improvement of the new generation of 3D sensor with reduced pixel size is visible (this was also discussed for 5×10^{15} n_{eq}/cm^2 in section 6.7.3).

6.7.5 High angle analysis

In high energy experiments, like in the inner detector of ATLAS, particles can cross the layers with different angles. The particular case of perpendicular incidence as well as low angle (15 °) has been explained in the previous sections. To study the extreme case of a particle going throw the sensors at high angles, measurements at 80° incidence have been carried out. In particular, these measurements were done with one sensor before irradiation (W3-E), one sensor after 5×10^{15} n_{eq}/cm^2 (W3-C1) and one after 1.0×10^{16} n_{eq}/cm^2 (W4-E), all uniformly irradiated at KIT. The tuning used was 1.0 ke^- and 6ToT@3ke^- since the charge deposited in each pixel due to the high angle is expected to be low. At 80°, the expected cluster size is ∼28 but it changes drastically with the angle. The equation

$$\varphi = \frac{\pi}{2} - arctan\left(\frac{w}{p(N_{cl}-1)}\right) \tag{6.3}$$

shows the dependence of the cluster size with the incidence angle (w = sensor width (230 μm), p = pixel length (50 μm) and N_{cl} = cluster length).

In figure 6.26 the cluster sizes with its respective incidence angle are shown. The cluster size for one 50×50 μm^2 1E small pitch sensor non irradiated is shown in figure 6.27. The cluster size at an intermediate voltage is 24, which corresponds to an incidence angle of 78.69° but varies between 22-24 at the different voltages. This value agrees with the values of the IBL device, since they were rotated in the Y direction where the pixel size is 50 μm for both devices. For the devices irradiated at 5×10^{15} n_{eq}/cm^2 and

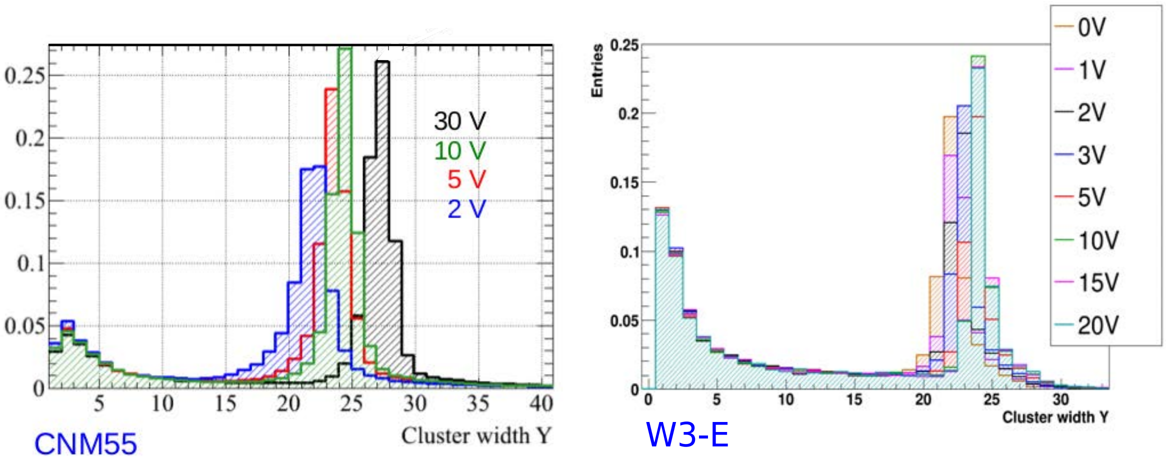

Figure 6.27: Cluster size at high angle for non irradiated 50×50 μm^2 1E small pitch (W3-E, right) and 50×250 μm^2 2E IBL (CNM55, left) devices at different voltages.

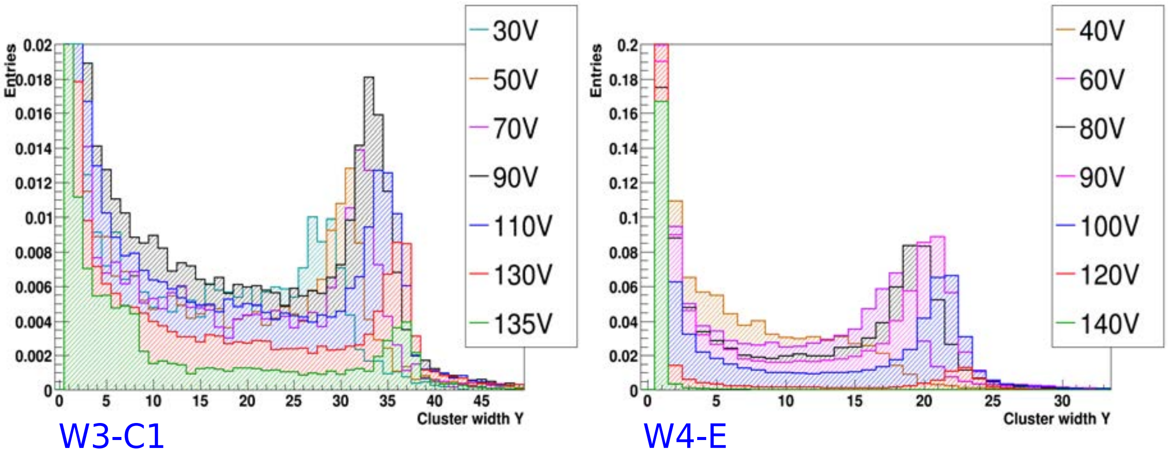

Figure 6.28: Cluster size at high angle for uniformly irradiated 50×50 μm^2 1E small pitch devices at 5×10^{15} n$_{eq}$/cm^2 (W3-C1, left) and 1×10^{16} n$_{eq}$/cm^2 (W4-E, right) at different voltages.

1×10^{16} n$_{eq}$/cm^2 the cluster size values are shown in figure 6.28. It ranges between 35-37 (82.51°) at 5×10^{15} n$_{eq}$/cm^2 and between 17-23 (76.39°) for 1×10^{16} n$_{eq}$/cm^2. The difference of cluster sizes may be due to the uncertainty of the incidence angle measurement in the different beam tests, causing small misalignment (figure 6.26 shows that cluster size changes fast with the incidence angle). The cluster size varies also at different voltages because the particles can pass throw a region that is not fully depleted since the columns are not fully passing through. This dependence is more visible for the irradiated devices.

To study the efficiency, the EUTelescope framework was not fully used due to its impossibility to successfully create tracks at these high angles. Instead, the raw data taken on the beam test is passed only through the converter and the clustering of EUTelescope,

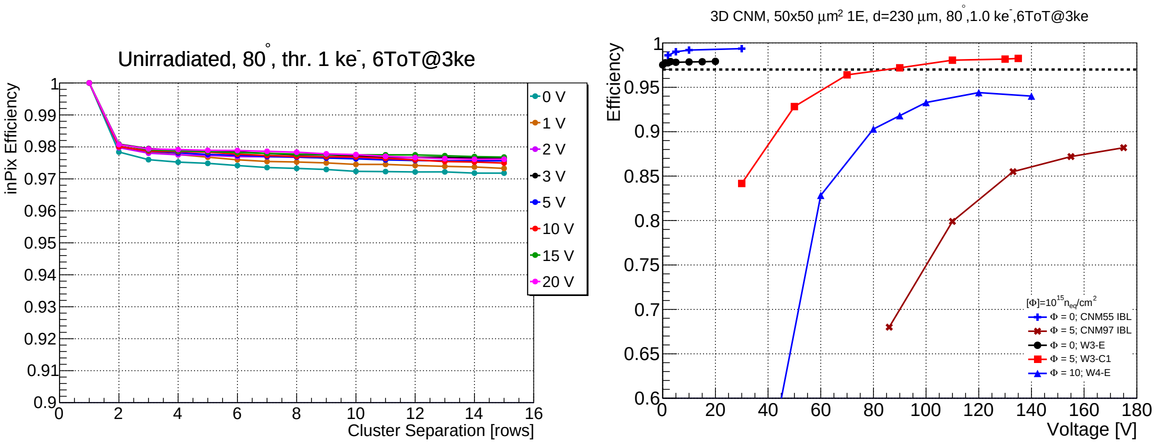

Figure 6.29: (Left) Hit efficiency of the pixels inside a cluster as a function of the allowed holes in the cluster at different voltages for the non irradiated device (W3-E). (Right) In pixel efficiency for the small pitch and IBL-like devices at high angle (taken from the left graph with a cluster separation of 10 for the device W3-E and similarly for the other devices).

obtaining only the clustered hits on the sensor (see section 5.4.3). The events with a cluster size lower than 15 are excluded since they come from broken clusters by interspersed noisy pixels. The detection efficiency on the remaining long clusters would be close to 100%, thanks to the fact that each particle is going throw several pixels. Instead, to analyze the performance of the independent pixels it is possible to define a "per pixel efficiency" using the long clusters in the direction of the rotation as pseudo-tracks and count the pixels that detect a hit between them. The pseudo-tracks are defined with the first and the last pixels of the long cluster while setting all the intermediate pixels to 1. The events selected are restricted to one column, hence, in the other direction the cluster size is fixed to one to avoid inefficiencies due to charge sharing. With this definition of the pseudo-tracks the per pixel efficiency can be defined as the standard efficiency (ratio of hits divided by the associated tracks). Then, the efficiency of the first and the last pixels is always 100% by definition and it is possible to study the hit efficiency of the other pixels inside this cluster. It is also necessary to take into account the noisy and unresponsive pixels inside the cluster. If no hole is allowed inside the cluster, the efficiency will be defined with its first and last working pixel, resulting in a 100% hit efficiency for all the pixels inside the cluster. This efficiency goes lower when increasing the number of allowed holes until a plateau is reached. This is shown for the device W3-E (non irradiated) in figure 6.29 (left). The plateau determines the number of holes taken to do the rest of the analysis, in this case the number was 10. The in pixel efficiency of the cluster is defined then as the efficiency with 10 allowed holes, and is shown in figure 6.29 (right) for all the devices and irradiations (using the same method than for the non irradiated device).

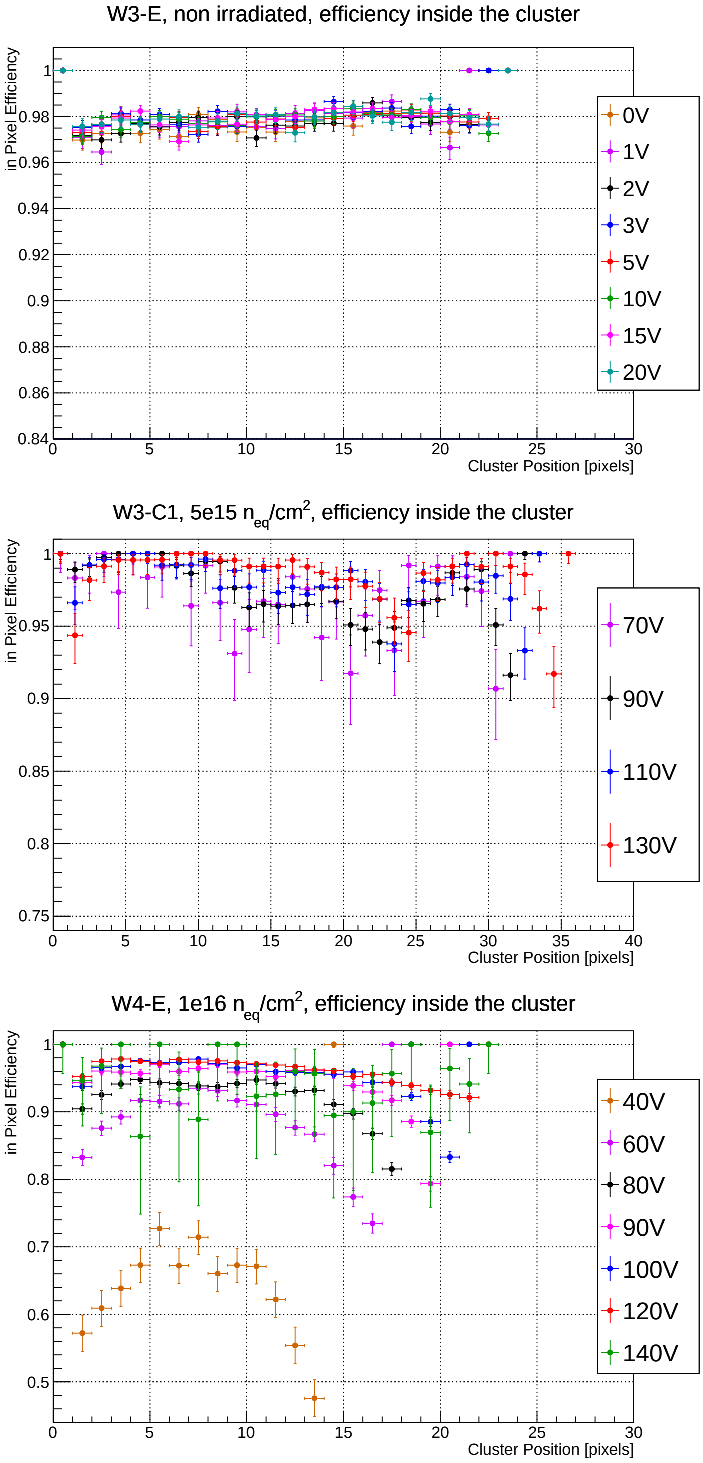

Figure 6.30: Efficiency for each pixel inside the cluster for non irradiated device (top), uniform irradiation to $5{\times}10^{15}$ n_{eq}/cm^2 (middle) and uniform irradiation to $1{\times}10^{16}$ n_{eq}/cm^2 (bottom). Note that the first and the last pixels of the cluster have always 100% efficiency by definition.

The in pixel efficiency before irradiation is over 97% even at 0 V, as observed for perpendicular incidence. It is comparable to the efficiency observed for IBL-like devices (which reaches up to 99% but the small pitch technology may improve with better processing). However after irradiation of $5{\times}10^{15}$ n_{eq}/cm^2 the small pitch show a much better performance than the IBL-like devices, reaching a 97% efficiency at ∼85 V and reaching up to 98% vs the IBL-like which does not reach 90% at the maximum voltage applied to this sensor [68]. The small pitch devices irradiated at $1{\times}10^{16}$ n_{eq}/cm^2 outperform even the IBL-like devices at lower fluences, reaching almost a 95% efficiency at 120 V which again demonstrates the big improvement that the smaller inter-electrode distance gives to the 3D sensors.

The efficiency of every single pixel inside the cluster is also possible to calculate and thus determine if the efficiency has any dependence with the internal structure of the sensor. The results are shown in figure 6.30. Due to the high performance of the small pitch sensors, the efficiency of all the pixels is very high for non irradiated and uniform irradiation at $5{\times}10^{15}$ n_{eq}/cm^2 for all the voltages measured. However for the highest irradiation of $1{\times}10^{16}$ n_{eq}/cm^2 and the lower voltages (40-60 V), a dependence of the efficiency on the pixel position inside the cluster is observed. At the edges of the cluster, the efficiency is noticeable lower on the regions of low field due to the non-fully passing through columns. This dependence is smaller, but still observable for all the other voltages at the highest irradiation level measured.

6.7.6 Thickness dependence

The Fondazione Bruno Kessler (FBK) is another center involved in the production of 3D sensors for ITk. They produced one run of small pitch sensors compatible with the FE-I4 chip and 130 μm active thickness. A single side process was used to etch the 3D columns which have a column diameter of 6 μm. The devices compatible with the FE-I4 produced had the configurations of $50{\times}50$ μm^2 1E and $25{\times}100$ μm^2 1E and 2E, and also a standard FE-I4 configuration with $50{\times}250$ μm^2 2E was produced. The devices studied here were the $50{\times}50$ μm^2 1E and the $50{\times}250$ μm^2 2E, to directly compare with the CNM devices studied before. Since it is expected that the final thickness of the sensors for the ITk innermost layer will be 150 μm the objective of this study is to verify that the power dissipation at the operation voltage of the thinner sensors is smaller than the CNM sensors with 230 μm thick.

One device with $50{\times}50$ μm^2 1E configuration was measured before irradiation, and one device with $50{\times}250$ μm^2 2E configuration was measured before irradiation and after an uniform irradiation at KIT of $3.8{\times}10^{15}$ n_{eq}/cm^2, both at the laboratory (leakage current) and at a beam test (hit reconstruction efficiency). The measurements on the beam were done only at perpendicular incidence and the tuning of the non irradiated devices was

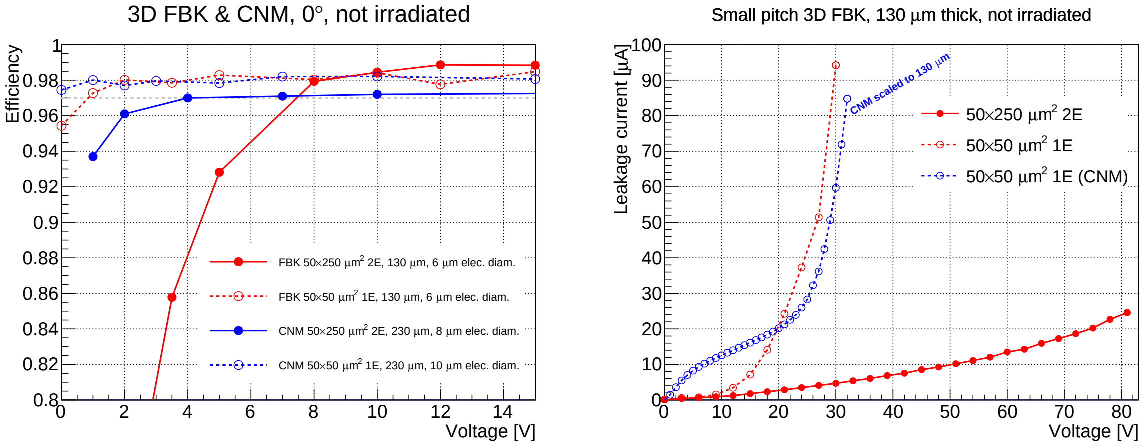

Figure 6.31: (Left) Efficiency of the FBK devices of 130 μm thickness with electrode diameter of 6 μm compared to CNM devices with 230 μm thickness with electrode diameter of 8 μm with pixel sizes of 50×50 μm^2 1E and 50×250 μm^2 2E at perpendicular incidence. (Right) Leakage current of the FBK devices measured in the beam test compared to one CNM small pitch sensor from the section 6.5.

1.5 ke$^-$ and for the irradiated was 1.0 ke$^-$, both with a 10 ToT response for a charge of 10 ke$^-$.

The beam test results before irradiation can be seen in figure 6.31 left. The efficiency for the thinner devices is lower for the same pixel size. The FBK device with pixel size of 50×50 μm^2 1E needs at least 1 V to reach the 97% benchmark efficiency while for the CNM device with the same pixel size no voltage is needed. For the other FBK device of 50×250 μm^2 2E, the voltage needed to reach the 97% benchmark is about 7.5 V, almost double than the 4 V of the CNM of 230 μm thickness. Also, a maximum efficiency of ∼99% is achieved in FBK sensors compared to CNM sensors (∼98% for small pitch and ∼97% for IBL) due to the effect of the column thickness (6 μm for FBK, 8 μm for CNM small pitch and 10 μm for CNM IBL). This is in agreement with the fact that in thinner devices the total collected charge is lower, hence a higher voltage is needed to achieve the same efficiency. Comparing the efficiency of different pixel sizes of the FBK devices, the trend observed in section 6.7.1 (between IBL geometry and small pitch) is confirmed. The voltage needed to reach the required efficiency decreases (from 7.5 to 1 V) when reducing the electrode distance (from 67 to 35 μm). The leakage current of these FBK devices is compared to one CNM small pitch on figure 6.31 right, with the leakage current of the CNM device scaled linearly to the 130 μm thickness of the FBK device. The current of the devices with 50×50 μm^2 1E pixel size is comparable.

Only the device with pixel size of 50×250 μm^2 2E was irradiated at KIT. It was irradiated to 3.8×10^{15} n$_{eq}$/cm^2 due to time constrains (the irradiation had to be stopped to measure the device in the closest beam test). The results of the efficiency are shown

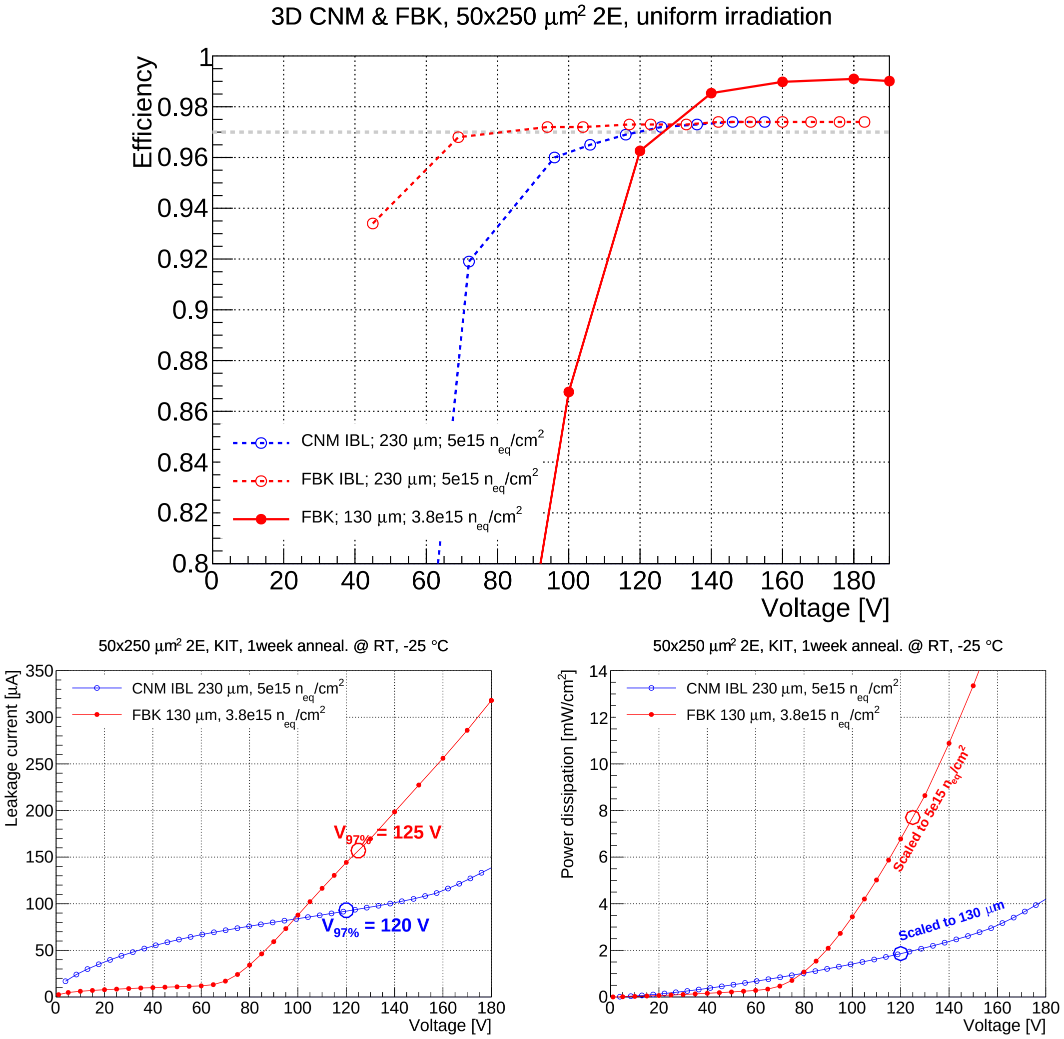

Figure 6.32: (Top) Efficiency of the FBK device with 50×250 μm^2 2E pixels, 130 μm thickness and electrode diameter of 6 μm compared to FBK and CNM devices similar to the IBL production with pixel size of 50×250 μm^2 2E and 230 μm thickness with electrode diameter of 8 μm at perpendicular incidence. (Bottom) Leakage current (left) and power dissipation (right) of the 50×250 μm^2 2E thin FBK device compared to a standard CNM IBL-like one. The power dissipation was scaled linearly to the same thickness and fluence.

in figure 6.32 top. It can be seen that the voltage necessary to achieve the 97% benchmark is higher for the lower thickness, following the trend observed in the devices before irradiation. A voltage of 125 V is needed for the 130 μm thick FBK sensor, higher than for the IBL-like devices from CNM (120 V) and from FBK (80 V). However, a maximum efficiency of 99% is reached on the first device while only a 97.5% is reached for the other devices, since, like for the non irradiated case, thanks to the thinner 3D columns the inefficiency due to undetected particles passing through the columns at perpendicular incidence is reduced. The power dissipation is extracted from figure 6.32 bottom with the

$V_{97\%}$ calculated with the efficiency, resulting in 7.5 mW/cm^2 for the FBK device compared to the 1.8 mW/cm^2 for the CNM one (scaled to 130 μm). In principle, one expect that lower thickness give lower power dissipation despite the need of higher operation voltage but in this particular sensor, a soft breakdown voltage appears at ∼70 V, resulting on a high leakage current at the operation voltage which leads to the higher power dissipation.

Chapter 7

Conclusions and outlook

This thesis describes the fabrication and characterization of the first 3D devices with pixel size of 50×50 μm^2 1E and 25×100 μm^2 2E before and after irradiation coupled to the FE-I4 readout chip. The aim was to demonstrate that they are a good candidate for the use in the innermost layer of the Inner Tracker (ITk) of the ATLAS detector after its 2026 upgrade for the High Luminosity Phase of the Large Hadron Collider (HL-LHC).

The 3D silicon sensors were already used for the 2015 upgrade of the ATLAS detector which inserted a layer of pixel detectors (IBL) closer to the beam pipe to improve the performance and the redundancy of the inner tracker system. However, for the ITk Pixel detector a smaller pixel size is needed on ITk to cope with the higher pile-up that the HL-LHC provides. Given the importance, for the physics reach of the experiment, of the innermost pixel layer (specially b-tagging), it becomes critical to understand which, if any, silicon technology could face the challenges of ITk. One obstacle to study devices with small pitch for the ITk Pixel detector, was that its first readout prototype chip, the RD53A, was not available until 2018. In order to overcome this issue, small pitch 3D sensors compatible with the IBL FE-I4 ASIC were fabricated in CNM-Barcelona in 2015. The hybridization and assembly of these devices were done in IFAE and their performance studied before and after irradiation in the framework of this thesis. The active thickness of these first small pitch 3D sensors was 230 μm, higher than the proposed one for ITk (of 150 μm) but this decision came at a later stage and, in any case, the results presented here are still very relevant.

Due to production problems with the first prototypes, only nine 3D small pixel devices were produced, eight with 50×50 μm^2 pixel size and one with 25×100 μm^2. Their hit efficiency was measured in beam test before irradiation, showing a ~97% efficiency at perpendicular incidence even without the application of any bias voltage. This improved already the performance of the IBL generation 3D pixel sensors, which needed at least 4 V to reach the required efficiency. It was shown that the efficiency increases up to ~97-98% for a small incident angle (15° with respect to the perpendicular case) since the influence of the low efficiency regions due to 3D columns is minimized.

To test the performance of these devices after high doses of irradiation[1], two types of irradiation were performed: uniform and non uniform. The uniform irradiation delivers the same fluence over the full 3D pixel sensor, allowing to parametrize the effect of the radiation (fluence) on the leakage current and the power dissipation. This also allows to directly compare the power dissipation performance of small pitch 3D sensors with the IBL generation. On the other hand, the non uniform irradiation delivers a range of fluences over the 3D pixel sensor, allowing to study the performance at different fluences on the same device at the expense of not being able to study the power dissipation. Only the devices with pixel size of 50×50 μm^2 could be measured after irradiation. For uniform irradiation, the fluences selected were of 5×10^{15} n$_{eq}$/cm^2 and 1×10^{16} n$_{eq}$/cm^2 while for non uniform irradiation, the fluences studied ranged from 8×10^{15} n$_{eq}$/cm^2 to 2.8×10^{16} n$_{eq}$/cm^2. At 5×10^{15} n$_{eq}$/cm^2, the benchmark efficiency of 97% is reached at 40 V for the small pitch 3D devices, while for 3D IBL-like sensor with their larger pixel size (of 50×250 μm^2 2E) a voltage of 120 V is needed. The efficiency of the small pitch 3D devices increases up to 99% at 15° incidence. The value of power dissipation also improves compared to the IBL-like sensors: from 3.5 mW/cm^2 to 1.5 mW/cm^2. For a fluence of 1×10^{16} n$_{eq}$/cm^2, the voltage needed for a 97% efficiency is 100 V, giving a power dissipation of 8 mW/cm^2. This can be compared to the most radiation hard planar technology evaluated at the same fluence, which gives a power dissipation of 25 mW/cm^2 at 500 V (3 times bigger). This demonstrates that the 3D technology with small inter-electrode distance has superior radiation hardness while consuming less power.

Thanks to the performance of the new generation of 3D small pitch shown in this thesis, they were selected as the technology to be used in the innermost layer of ITk. A new production of 3D sensors with pixel size of 50×50 μm^2 and 25×100 μm^2 was fabricated in 2018 to be coupled to the RD53A prototype, and the results obtained from these devices confirm the ones presented in this thesis [69]. Up to the highest fluence measured in this thesis, the radiation damage does not seem to be a limiting parameter in terms of 3D sensors performance, which can reach the required efficiency by increasing the bias voltage. In the future, more beam test can be carried out with the RD53 chip at higher irradiation levels to study the limits of the 3D technology.

---

[1] The expected fluence on the innermost layer of ITk is 1.4×10^{16} n$_{eq}$/cm^2.

List of Figures

List of Tables

Bibliography

[1] L. Evans and P. Bryant, *LHC Machine*, JINST 3 (2008) S08001.

[2] C. Lefèvre, *The CERN accelerator complex*, CERN-DI-0812015.

[3] ATLAS Collaboration, *ATLAS Luminosity Public Results*, https://twiki.cern.ch/twiki/bin/view/AtlasPublic/LuminosityPublicResults.

[4] ATLAS Collaboration, *ATLAS Luminosity Public Results Run 2*, https://twiki.cern.ch/twiki/bin/view/AtlasPublic/LuminosityPublicResultsRun2.

[5] G. Apollinary et al., *High-Luminosity Large Hadron Collider (HL-LHC) : Technical Design Report V. 0.1*, CERN-2017-007-M.

[6] *The LHC project schedule*, https://project-hl-lhc-industry.web.cern.ch/content/project-schedule.

[7] ALICE Collaboration, *The ALICE experiment at the CERN LHC*, JINST 3 (2008) S08002.

[8] LHCb Collaboration, *The LHCb detector at the LHC*, JINST 3 (2008) S08005.

[9] ATLAS Collaboration, *The ATLAS experiment at the CERN Large Hadron Collider*, JINST 3 (2008) S08003.

[10] CMS Collaboration, *The CMS experiment at the CERN LHC*, JINST 3 (2008) S08004.

[11] ATLAS Collaboration, *ATLAS magnet system: Technical Design Report, 1*, CERN-LHCC-97-018.

[12] Joao Pequenao, *Computer generated image of the whole ATLAS detector*, CERN-GE-0803012.

[13] ATLAS Collaboration, *ATLAS inner detector: Technical Design Report, 1*, CERN-LHCC-97-016.

[14] ATLAS Collaboration, *ATLAS inner detector: Technical Design Report, 2*, CERN-LHCC-97-017.

[15] Y. Unno et al., *ATLAS silicon microstrip Semiconductor Tracker (SCT)*, Nucl. Instr. Meth. A 453 (2000) 109.

[16] A. Ahmad et al., *The silicon microstrip sensors of the ATLAS semiconductor tracker*, Nucl. Instr. Meth. A 578 (2007) 98.

[17] ATLAS TRT Collaboration, *The ATLAS Transition Radiation Tracker (TRT) proportional drift tube: Design and performance*, JINST 3 (2008) P02013.

[18] A. Vogel et al., *ATLAS Transition Radiation Tracker (TRT): Straw tube gaseous detectors at high rates*, Nucl. Instr. Meth. A 732 (2013) 277.

[19] Joao Pequenao, *Computer generated image of the ATLAS inner detector*, CERN-GE-0803014.

[20] ATLAS Collaboration, *ATLAS liquid-argon calorimeter: Technical Design Report*, CERN-LHCC-96-041.

[21] ATLAS Collaboration, *ATLAS tile calorimeter: Technical Design Report*, CERN-LHCC-96-042.

[22] Joao Pequenao, *Computer Generated image of the ATLAS calorimeter*, CERN-GE-0803015.

[23] ATLAS Collaboration, *ATLAS muon spectrometer: Technical Design Report*, CERN-LHCC-97-022.

[24] Joao Pequenao, *Computer generated image of the ATLAS Muons subsystem*, CERN-GE-0803017.

[25] Joao Pequenao, *Computer generated images of the Pixel, part of the ATLAS inner detector*, CERN-GE-0803013.

[26] ATLAS Collaboration, *Pixel Detector Technical Design Report*, CERN-LHCC-98-013.

[27] G. Aad et al., *ATLAS pixel detector electronics and sensors*, JINST 3 (2008) P07007.

[28] M. Capeans et al., *ATLAS Insertable B-Layer Technical Design Report*, CERN-LHCC-2010-013.

[29] ATLAS Collaboration, *Technical Design Report for the ATLAS Inner Tracker Pixel Detector*, CERN-LHCC-2017-021.

[30] M. Elsing et al., *Final Report of the second ITk Pixel Layout Task Force*, ATL-COM-ITK-2018-053.

[31] M. Tanabashi et al. (Particle Data Group), *Particle Physics Booklet*, Phys. Rev. D 98, 030001.

[32] R. Sternheimer, M. Berger, and S. Seltzer, *Density effect for the ionization loss of charged particles in various substances*, Atomic Data and Nucl. Data Tab. 30 (1984) 261.

[33] H. Bichsel, *Straggling in Thin Silicon Detectors*, Rev. Mod. Phys 60 (1988), pp. 663-699.

[34] L. Rossi et al., *Pixel Detectors*, Particle Acceleration and Detection. Berlin: Springer-Verlag, 2006. isbn: 9783540283324, 9783540283331.

[35] W. Shockley, *Currents to Conductors Induced by a Moving Point Charge*, Journal of Applied Physics 9.10 (Oct. 1938), pp. 635–636.

[36] Simon Ramo, *Currents induced by electron motion*, Proc. Ire. 27 (1939), pp. 584–585.

[37] J.R. Srour et al., *Review of displacement damage effects in silicon devices*, IEEE Trans. Nucl. Sci. 50 (2003) 653.

[38] A. Vasilescu (INPE Bucharest) and G. Lindstroem (University of Hamburg), *Displacement Damage in Silicon: Online compilation*, https://rd50.web.cern.ch/rd50/NIEL/.

[39] M. Moll, *Radiation damage in silicon particle detectors: Microscopic defects and macroscopic properties*, Ph.D. Thesis, University of Hamburg, Hamburg Germany (1999) DESY-THESIS-1999-040 and online pdf version at http://mmoll.web.cern.ch/mmoll/thesis/pdf/moll-thesis.pdf.

[40] Sherwood I. Parker, Christopher J. Kenney, and Julie Segal. *3-D: A New architecture for solid state radiation detectors*, Nucl. Instr. Meth. A 395 (1997), pp. 328–343.

[41] C. Kenney et al., *Silicon detectors with 3-D electrode arrays: fabrication and initial test results*, IEEE Transactions on Nuclear Science 46.4 (1999), pp. 1224–1236.

[42] ATLAS IBL Collaboration, *Prototype ATLAS IBL Modules using the FE-I4A Front-End Readout Chip*, JINST 7 (2012) P11010.

[43] M. Garcia-Sciveres, *The RD53A Integrated Circuit*, CERN-RD53-PUB-17-001.

[44] M. Garcia-Sciveres, *RD53A Integrated Circuit Specifications*, CERN-RD53-PUB-15-001.

[45] D. Nelson, *HSIO II Development Platform Users Guide*, HSIO-II 2015 guide.

[46] J. Große-Knetter et al., *USB based readout system for ATLAS FE-I3 and FE-I4*, http://icwiki.physik.uni-bonn.de/twiki/bin/view/Systems/UsbPix.

[47] I. Peric et al., *The FEI3 readout chip for the ATLAS pixel detector*, Nucl. Instr. Meth. A 565 (2006) 178.

[48] M. Garcia-Sciveres et al., *The FE-I4 pixel readout integrated circuit*, Nucl. Instr. Meth. A 636 (2011) S155.

[49] A. Belloti, *Charge Collection Studies of 3D Pixel Detectors*, Bachelor of Physics thesis, University Autónoma de Barcelona (UAB) 2015.

[50] J. Baudot et al., *First Test Results Of MIMOSA-26, A Fast CMOS Sensor With Integrated Zero Suppression And Digitized Output*, 2009 IEEE Nuclear Science Symposium Conference Record (NSSMIC.2009.540239).

[51] EUTelescope Software Developers, *EUTelescope: A Generic Pixel Telescope Data Analysis Framework*, https://eutelescope.github.io, https://github.com/eutelescope.

[52] V. Blobel, *Software alignment for tracking detectors*, Nucl. Instr. Meth. A566 (2006) 5.

[53] R. E. Kalman, *A New Approach to Linear Filtering and Prediction Problems*, Journal of Basic Engineering 82 (1960) 35.

[54] V. Blobel, *A new fast track-fit algorithm based on broken lines*, Nucl. Instr. Meth. A566 (2006) 14.

[55] TBMon2 Software, *TBMon2*, https://gitlab.cern.ch/tbmon2/tbmon2.

[56] J. Weingarten et al., *Planar Pixel Sensors for the ATLAS Upgrade: Beam Tests results*, JINST 7 (2012) P10028.

[57] M. Paterno, *Calculating efficiencies and their uncertainties*, Fermilab, (2004), FERMILAB-TM-2286-CD.

[58] Kasugai Y. et al., *Measurement of Activation Cross Sections on Tantalum and Tungsten with 14 MeV Neutrons*, Journal of Nuclear Science and Technology 31, (1994) 12.

[59] L. Simon, *TCT Measurements on 3D small pitch strip detectors*, Master thesis, University Autónoma de Barcelona (UAB) 2016.

[60] J. Lange et al., *Radiation hardness of small-pitch 3D pixel sensors up to a fluence of* $3{\times}10^{16}\ n_{eq}/cm^2$, JINST 13 (2018) P09009.

[61] S. Grinstein et al., *Module production of the one-arm AFP 3D pixel tracker*, JINST 12 (2017) C01086.

[62] M. Bigas, E. Cabruja and M. Lozano, *Bonding techniques for hybrid active pixel sensors (HAPS)*, Nucl. Instrum. Meth. A 574 (2007) 392.

[63] P. S. Miyagawa and I. Dawson, *Radiation background studies for the Phase II inner tracker upgrade*, Tech. Rep. ATL-UPGRADE-PUB-2013-012, CERN, February, 2013.

[64] G.-F. Dalla Betta et al., *Investigation of leakage current and breakdown voltage in irradiated double-sided 3D silicon sensors*, JINST 11 (2016) P09006.

[65] J. Lange et al., *Radiation hardness of 3D pixel detectors up to* $2{\times}10^{16}\ n_{eq}/cm^2$, 27th RD50 Workshop (CERN).

[66] J. Lange et al., *3D silicon pixel detectors for the High-Luminosity LHC*, JINST 11 (2016) C11024 [arXiv:1610.07480].

[67] N. Savic et al., *Investigation of thin n-in-p planar pixel modules for the ATLAS upgrade*, JINST 11 (2016) C12008.

[68] I. Lopez, *Recent testbeam results of 50 m pitch 3D sensors at high incidence angle for HL-LHC*, Talk at the 26^{th} RD50 Workshop.

[69] S. Terzo et al., *Performance of Irradiated RD53A 3D Pixel Sensors*, JINST 14 (2019) P06005.

Acknowledgements

I would like to dedicate some lines to thank everyone that made this thesis possible. First of all I want to express my gratitude to Sebastian Grinstein for giving me the opportunity to join his group. His supervision, continuous support and advice was specially important. Special thanks also to Jörn and Stefano who taught me a lot and have been very patient. I want also to thank my colleagues for their help and the good times we shared together: Iván, Emanuele, Fabian, Giulia, Chiara, Tianya, Vagelis and Lucia. Also thanks to all the IFAE members which created an enriching environment during my PhD years. Thanks to the people of CNM and of the workshop, my thesis would not be possible without their hard work.

I want also to mention the people from the irradiation facilities: F. Ravotti and G. Pezullo (CERN IRRAD), V. Cindro and I. Mandic (JSI Ljubljana) and A. Dierlamm and F. Bögelspacher (KIT) for their excellent support. Thanks to the ITk community specially to Jens Weingarten, André Rummler and Marco Bomben for the hard work organizing test beams and the great help they provided. Also thanks to Claudia Gemme, Hide Oide and the rest of the INFN Genova group. They provided great help and support in the 5 months I worked with them.

Last but not least, quero agradecer á miña familia e amigos. Sei que vos teño lonxe, pero sempre vos teño no meu corazón. Especialmente ós meus pais, que sempre me apoiaron nas miñas decisións e me deixaron liberdade para perseguir os meus soños. Grazas Andrea, es a persoa máis importante na miña vida, sempre me alentas a que traballe duro e me apoias moito. Tamén agradezo á túa familia, que tamén me apoia como se fose a miña propia.

This work was partially funded by the MINECO, Spanish Government, under the grant FPA2013-48308-C2-1-P.